Tidal distortion in the Arcachon basin

PAULO SALLES[1], ALDO SOTTOLICHIO[2], PATRICE BRETEL[2],
STÉPHANE BUJAN[2], RODRIGO PEDREROS[3]

1. Universidad Nacional Autónoma de México, Instituto de Ingeniería, 5-306,
Ciudad Universitaria, 04510 México D.F., Mexico
email: psallesa@ii.unam.mx

2. Université Bordeaux 1, Laboratoire EPOC, avenue des Facultés,
33405 Talence Cedex, France
email: a.sottolichio@epoc.u-bordeaux1.fr, p.bretel@epoc.u-bordeaux1.fr,
s.bujan@epoc.u-bordeaux1.fr

3. BRGM, Aménagement et Risques Naturels (ARN/ESL)
3, avenue C. Guillemin - BP6009, 45060 Orléans Cedex 2, France
email: r.pedreros@brgm.fr

Keywords: nonlinear tidal distortion, coastal lagoon hydrodynamics, long term morphodynamics

ABSTRACT

In order to address the inlet morphodynamics, the water quality and in particular the problem of episodic invasions of toxic algae (dynophisis) in the Arcachon Coastal Lagoon in the French Atlantic, the understanding of the lagoon hydrodynamics was improved, through the analysis of field data. Two ADCP and an ADV were installed during one lunar cycle in the two channels of the inlet and in the upper reaches of the lagoon. Wind and a fourth tide gage data were also available.

Based on the concepts of flood and ebb dominance, the relative phase of the M_2 and M_4 tidal constituents, and the residual non-astronomic tide, the general circulation patterns were investigated.

Introduction

The tidal distortion in coastal semi-enclosed water bodies is an important parameter from a range of points of view: water quality, larval dispersal paths, inlet morphodynamics, navigation… In fact, at least for single-inlet systems, the tidal distortion, commonly represented by the evolution and transformation of the M_2 and M_4 tidal constituents, determines the Flood or Ebb dominance of the system, i.e. its infilling tendency or flushing capacity (e.g., Friedrichs et al., 1988; Salles et al., 2005).

Tidal distortion and generation of compound tides

As the tide propagates to the coasts and enters semi-enclosed coastal water bodies it experiences significant transformations, ranging from dissipation, distortion and the generation of compound tides. For instance, by looking at the x-momentum equation

$$h\left(\frac{\partial U}{\partial t}+U\frac{\partial U}{\partial x}\right)+gh\left(\frac{\partial a}{\partial x}+\frac{\partial h}{\partial x}\right)-\frac{h}{\rho}\left(E_{xx}\frac{\partial^2 U}{\partial x^2}\right)-\frac{\tau_{zx}}{\rho}=0\,, \tag{1}$$

and defining the velocity in terms of the M_2 and M_4 tidal components as

$$U=u_2\cos\left(kx-\varphi_2\right)+u_4\cos\left(2kx-\varphi_4\right), \tag{2}$$

the resulting convective acceleration reads

$$U\frac{\partial U}{\partial x} = \overbrace{-\frac{1}{2}ku_2u_4\cos\left(kx+\varphi_2-\varphi_4-\frac{\pi}{2}\right)}^{M_2} \overbrace{-k\frac{u_2^2}{2}\cos\left(2kx-2\varphi_2-\frac{\pi}{2}\right)}^{M_4} \underbrace{-\frac{3}{2}ku_2u_4\cos\left(3kx-\varphi_2-\varphi_4-\frac{\pi}{2}\right)}_{M_6} \underbrace{-ku_4^2\cos\left(4kx-2\varphi_4-\frac{\pi}{2}\right)}_{M_8}. \quad (3)$$

Other nonlinear terms, e.g., friction, also distort the tide.

Defining, for a semi-diurnal tide, the relative phase and the degree of nonlinear distortion, respectively, as:

$$Phase_{M_4\,M_2} = 2\varphi_2 - \varphi_4, \quad \text{and} \quad \frac{u_4}{u_2} \quad (4)$$

we can see that the resulting velocity from the M_2 and M_4 tidal components, as well as the sediment transport capacity ($\sim V^3$), vary dramatically, depending on the relative phase, as shown in Figure 1. The ranges for ebb/flood dominance, both for currents and WSE, are shown in Figure 2.

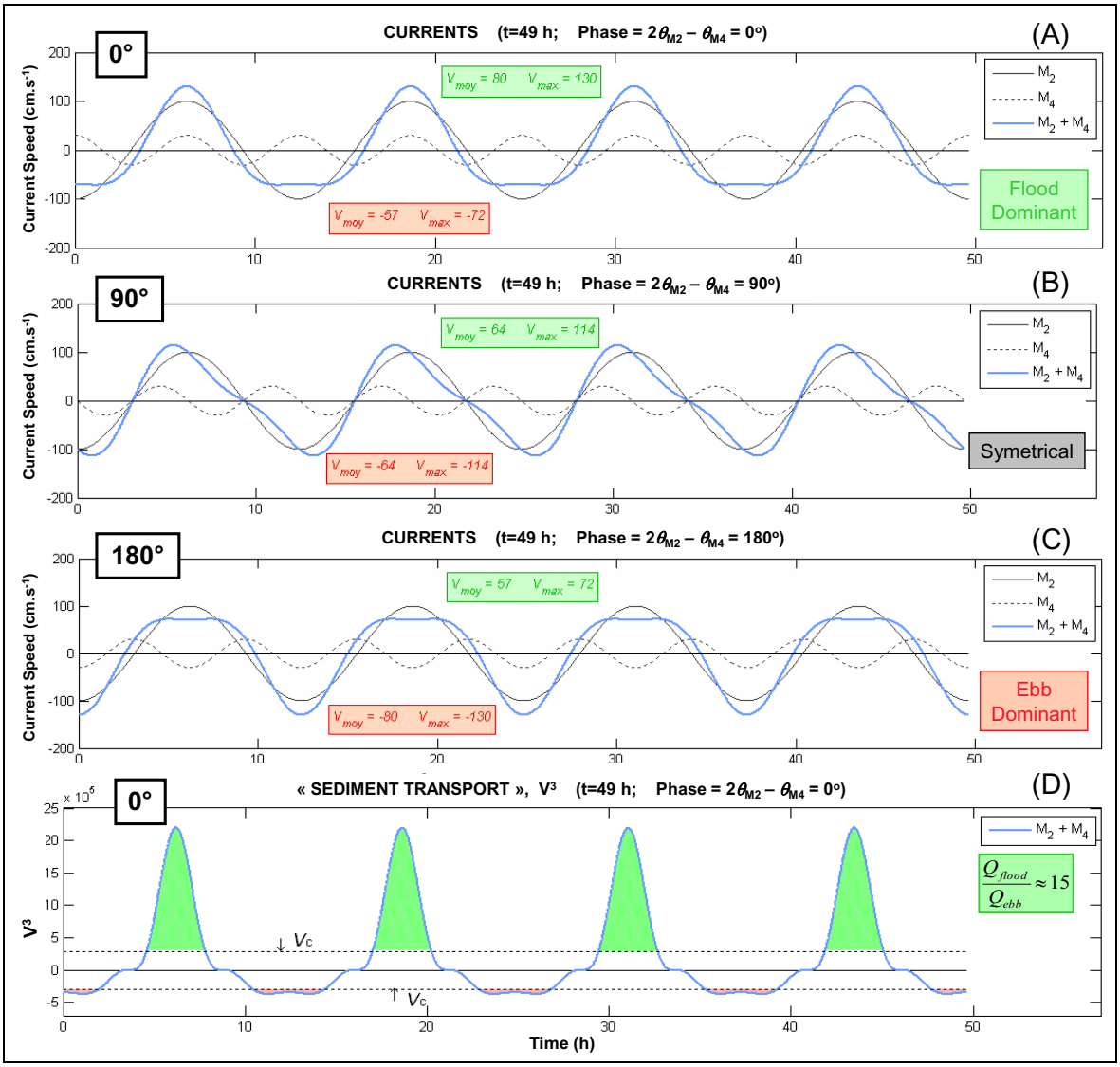

Figure 1. Theoretical resulting velocity (panels A, B and C) and sediment transport capacity (proportional to V^3; panel D) for different relative phases between the M_2 and M_4 tidal components (0°, 90°, and 180°).

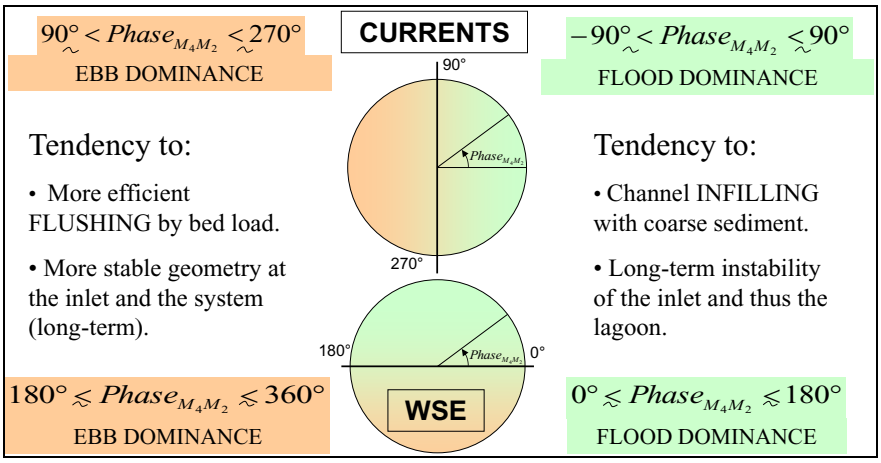

Figure 2. Ranges for ebb and flood dominance.

Study site

This phenomenon was studied during winter 2007 in the Arcachon basin (see Figure 3).

Figure 3. Study site, Arcachon basin, French Atlantic.

- 160 km^2
- Large intertidal flats (52%)
- Channel network (48%)
- Semi-diurnal tide (2–4 m amplitude)
- Inlet with Mixed Energy regime
- Small Flood Delta
- Large Ebb Delta
- Two Passes: 'Nord' and 'Sud'
- Only one Channel

Instrumentation

- Two ADCPs for waves and currents at the inlet (Passe Nord & Passe Sud).
- Current meter at 'Cassy'.
- Pressure Sensor at 'Eyrac' (SHOM).
- Wind (speed and direction) at 'Cap Ferret' (courtesy of Météo France).

Results

The tidal data (WSE and current profile) was studied in terms of (i) current profiles and residuals, (ii) harmonic analysis, (iii) flood and ebb durations, (iv) tidal constituent evolution inside the system (see Figure 4), and (v) nonlinear distortion and dominance phase (see Figure 5).
It can be seen from Figure 5 that:

- during neap tide (and neap-spring transition), when the intertidal zones are mostly emerged, the tidal trough propagation is slower, meaning that the ebb is weaker and longer, and the flood is stronger and shorter, which translates in flood dominance.
- during spring tide (and spring-neap transition), when the intertidal zones are mostly submerged, the friction is larger during flood, meaning that the flood is weaker and longer, and the ebb is stronger and shorter, which translates in ebb dominance.

Conclusions

The data analysis suggests that the tide outside and inside Arcachon, as well as the geometry and the bathymetry, are such that:

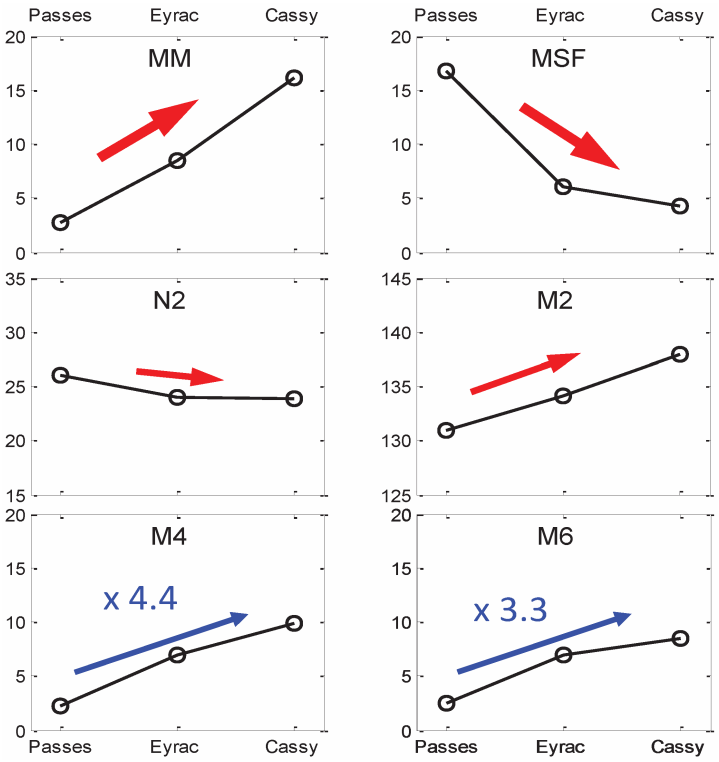

Figure 4. Tidal component evolution upstream.

- Except for southeasterly winds, both Passes are ebb dominant.
- However, Passe Nord is a net exporter of water and sediment and Passe Sud is a net importer,
- Passe Nord is the able to stay open, even with the strong N-S littoral drift.
- Inside the system ('Cassy' station), flood dominates during Neap tide (accumulation of water and material up in the lagoon) and ebb is more important during Spring tide.
- The tidal distortion analysis is useful to estimate the 'health' of a system in the long term.

Acknowledgements

This study was part funded by the Universidad Nacional Autonoma de México, the French PNEC Littoral Atlantique, Université Bordeaux 1, and BRGM.

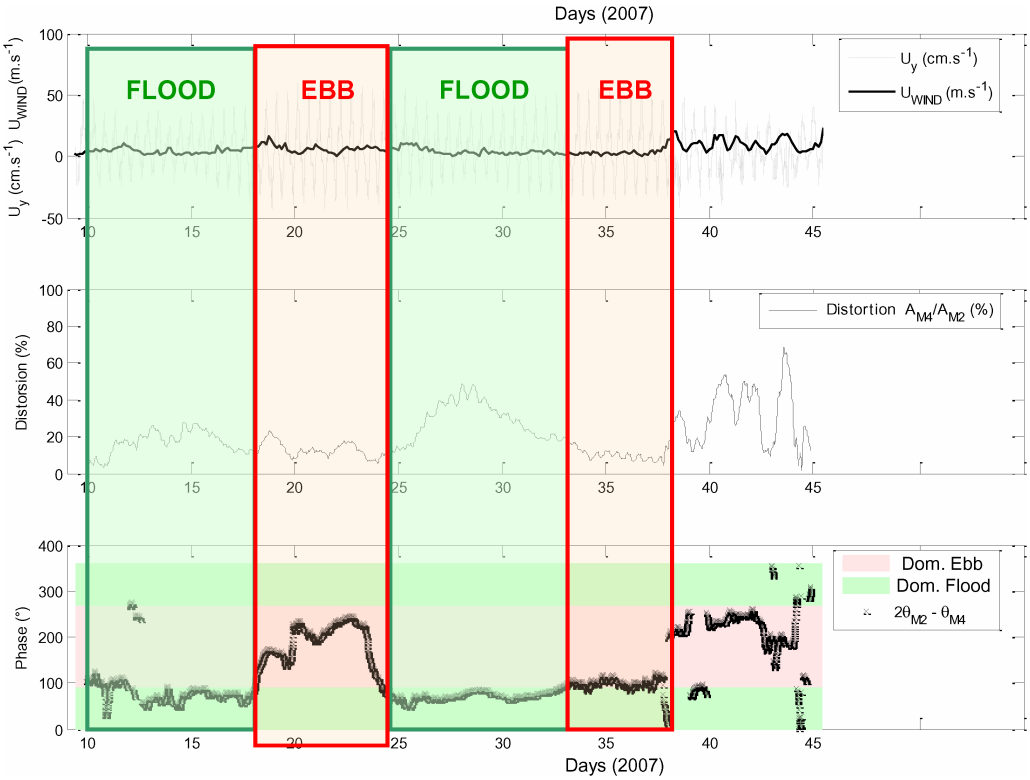

Figure 5. Nonlinear distortion and dominance phase at Cassy.

References

Friedrichs C.T., Aubrey D.G. (1988), Nonlinear tidal distortion in shallow well-mixed estuaries: A synthesis, *Estuarine, Coastal and Shelf Science*, 27, 521–545.

Salles P., Voulgaris, G., Aubrey, D.G. (2005), Contribution of non-linear mechanisms in the persistence of multiple tidal inlet systems, *Estuarine, Coastal and Shelf Science*, 65, 475–491.

Computational modeling and field measurements of stratification in Sydney Harbour estuary

SERENA B. LEE, GAVIN BIRCH

School of Geosciences, University of Sydney, Madsen Building, Sydney 2006, New South Wales, Australia
email: serena.lee@usyd.edu.au, gavin@usyd.edu.au

Keywords: stratification, freshwater plume, turbidity, contaminant transport

ABSTRACT

Sydney Harbour is a well-mixed tidally, dominated micro-tidal estuary on the east coast of Australia. The estuary is surrounded by Sydney metropolis, the most populated city in Australia. Approximately 90% of the 500 km^2 Sydney Harbour catchment is urbanized and impervious surfaces cover the majority of catchment area generating large volumes of runoff during high precipitation storm events. Under quiescent conditions the estuary is well mixed due to low fluvial inputs from the main rivers (Parramatta, Duck and Lane Cove), as well from numerous creeks and canalized stormwater drains discharging to the estuary. During high-precipitation conditions freshwater plumes develop and stratification is observed. It was thought that these high-precipitation events (rainfall >50 mm day^{-1}) produced a distinct upper-layer freshwater plume which transverses the harbor into the open ocean, essentially bypassing the estuary altogether. Current monitoring of such events revealed a more complex plume behavior and a multi-cyclic transport mechanism for particulate-bound contaminants associated with stormwater runoff in this estuary.

The primary aim of this study was to investigate the configuration of freshwater plumes generated under high precipitation conditions in the Sydney Harbour estuary. This new hydrological information will form the foundation for the identification of transport pathways for contaminants associated with freshwater plumes. Further studies will determine likely locations for deposition of contaminants associated with runoff from extreme storm events and will facilitate implementation of appropriate management strategies to reduce negative impacts from storm water runoff on the estuarine environment.

Methods

Five storm events were monitored between January 2005 and September 2007 to better comprehend plume generation, transport and collapse. Salinity and turbidity measurements were taken at between 40 and 50 sites throughout the estuary during these field investigations. Plume structure was determined from CTD measurements taken through the water column and rain gauge measurements throughout the catchment

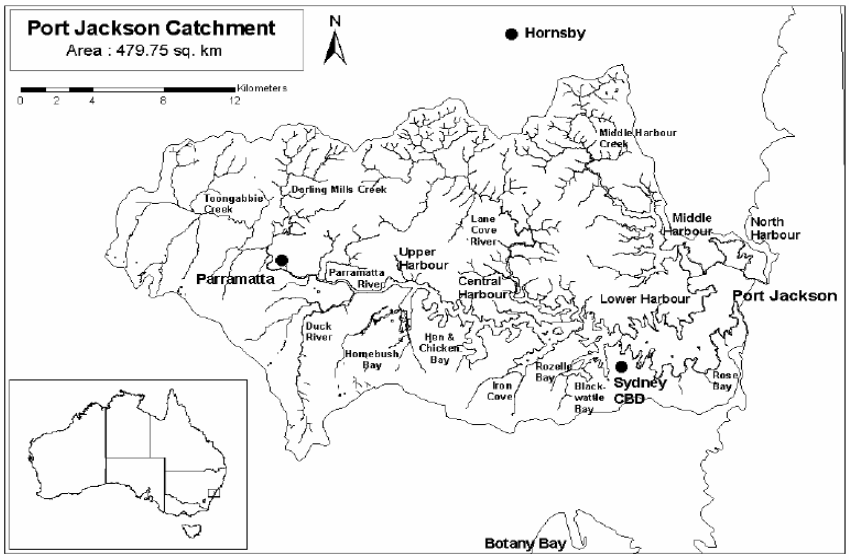

Figure 1. Sydney Harbour (Port Jackson) estuary (Cruickshank, 2006).

provided by the Bureau of Meteorology were used to estimate runoff volumes generated during storm events for each subcatchment.

Estimated runoff volumes for the top 16 subcatchments responsible for the majority of fluvial discharge to the estuary were applied to a verified and calibrated hydrodynamic model of Sydney Harbour. The Environmental Fluid Dynamics Code (EFDC) was the modeling suit utilized for the study. Salinity profiles through the water column predicted by the model were compared with corresponding field measured profiles. The hydrodynamic models were run for an additional 2–4 weeks following the end of a storm event to determine the models ability to predict collapse and dispersal of freshwater plumes generated by these events.

Results

Table 1 summarizes monitored and modeled salinity results from representative sites throughout the estuary after the commencement of a high-precipitation event in June 2007 when a freshwater plume was observed throughout most of Sydney Harbour.

In the upper reaches of the estuary at the confluence of the Duck and Parramatta Rivers, salinity measurements during high-precipitation events were generally <5 ppt from the top to the bottom of the water column. Surface water salinity was lower than salinity at the bottom of the water column at all locations for all monitored storm events. Stratification was strongest in the upper estuary (upstream Parramatta and Duck Rivers) and the upper Lane Cove River which joins the main channel in the central estuary (Figure 1). The freshwater plume was well defined in the main channel of the upper estuary. In this section of the waterway the salinity interface between fresh and marine water was very sharp. Whilst stratification was evident in the central estuary, surface water salinity was approximately 10 ppt and the salinity gradient at the interface between fresh and marine water layers was more gradual.

The structure of the freshwater plume varied between rainfall events as is illustrated in Figure 3. Modeling of the June 2007 storm event qualitatively replicated freshwater plume generation for this event. Salinity profiles resulting from high-precipitation events, as predicted by the hydrodynamic model of Sydney Harbour, compared favorably with monitored salinity profiles in most sections of the estuary. However, accurate quantitative predictions in some sections were limited (Table 1). Figure 4 displays the comparison of modeled and monitored salinity results on the 10th of June 2007 for one monitored site.

Table 1. Salinity measurements Sydney Harbour, 10 June 2007 (three days after rain commenced and the day following highest measured 24-hr rainfall for this event).

Site location (beginning upstream)	Monitored surface water salinity (ppt)	Monitored bottom water salinity (ppt)	Monitored plume structure	Modeled salinity of surface water (ppt)	Modeled bottom water salinity (ppt)
Duck River	0.72	1.88	0–2.33 m : <0.2 ppt (whole water column)	0	0
Parramatta River	0.85	15.78	0–2.09 m : <2.5 ppt 3.12 m : 15 ppt	0	0
Upper estuary main channel	1.85	23.1	0–1.80 m : <2.5 ppt 2.0 m : 10.68 ppt 3.04 m : 23.1 ppt	0	0
Central estuary main channel	8.13	31.04	0–1.33 m : 8–9.17 ppt 2.47 m : 20.07 ppt 11.96 m : 31.04 ppt	15	31.5
Lane Cove River mouth	3.97	28.67	0–1.75 m : 3.5–16 ppt 2.6 m : 23 ppt 3.5m : 28.5 ppt	8	30.5
Upper Lane Cove River	2.95	19.24	0–1.60 m : 3–5 ppt 1.9 m : 11 ppt 2.85 m : 18.4 ppt	0	1.5
Central estuary, off-channel embayment	10.45	30.41	0–1.20 m : 10–12 ppt 2.5 m : 17.8 ppt 5 m : 30.4 ppt	12	24.5
Lower estuary main channel	15	34.72	0–1.45 m : 15–23 ppt 2.0 m : 29 ppt 6.10 m : 36.5 ppt	22	36.5

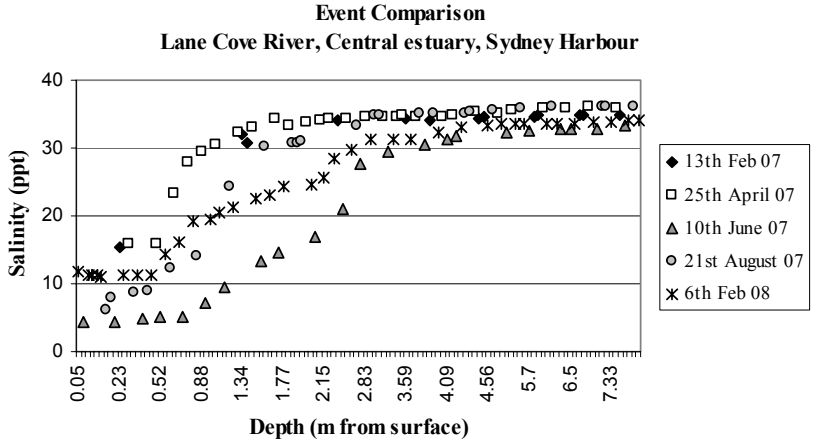

Figure 3. Salinity profiles, Lane Cove River, Sydney Harbour, for five monitored storm events.

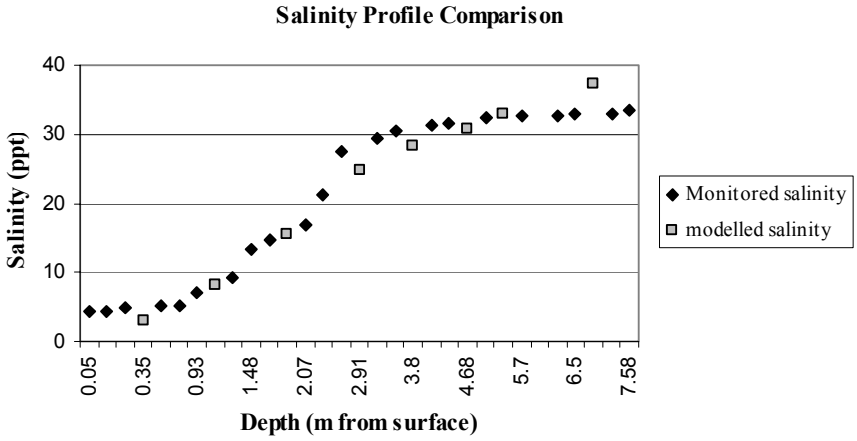

Figure 4. Monitored and modeled salinity profiles for 10th June 2007, Lane Cove River, Sydney Harbour.

Both monitoring and modelling of salinity variations throughout the estuary during storm events showed the freshwater plumes formed at the upstream ends of the three main rivers joining the main channel of the estuary. These freshwater plumes collapsed in or near the central estuary excepting during the June 2007 event. During the four day storm event daily rainfall throughout the catchment ranged between 25 mm to 150 mm. The resulting freshwater plume migrated into the lower estuary and approached the estuary mouth. Modelling of the storm event showed freshwater entering the lower estuary. Predicted salinity of surface water in the region from the model was ~7 ppt higher than the field data (Table 1), however modeled salinity was averaged over the depth of the cell (~1.2 m) and so is expected to be somewhat higher than measured surface water salinity.

Discussion

Factors controlling plume development and collapse and the relationship between monitored and modeled results are discussed.

Areas of the estuary where freshwater plumes originated in the current study have a high ratio of subcatchment surface area to receiving water surface area. The two primary regions where freshwater plumes developed during this study are the Upper Parramatta River and Lane Cove River receiving basins. The Upper Parramatta River and Lane Cove River subcatchments cover approximately 25% and 20% of the total Sydney Harbour catchment, respectively. Both estuarine sections to these rivers are narrow (less than 70 m wide) and shallow (<5 m) resulting in small volumes of saline water. Monitoring of salinity through the water column in the entire estuary revealed that the plume occupying the Parramatta and Duck Rivers experienced a higher degree of mixing between the fresh and marine water layers upon reaching the central estuary. Complex current patterns and higher current velocities are present in this area (unpublished Acoustic Doppler Current Profiles: February 2007, May 2007). The increased hydrodynamic activity would likely contribute to increased friction at the fresh/saline water interface and result in increased mixing. The freshwater plume from Lane Cover River converged with the freshwater plume from the Parramatta and Duck Rivers in the central estuary.

Comparison of salinity profiles between events demonstrated a strong relationship between salinity of the freshwater plume and storm intensity and duration. The site depicted in Figure 3 is located in the lower Lane Cove River, approximately 800 m upstream of the river mouth. Surface water salinity was lowest during the June 2007 storm and this storm event was the most intense monitored. Additionally, the event continued for four consecutive days as opposed to other events which took place over one to two consecutive days.

Modeling of rain events gave good indications of the time taken for a plume to develop once a high precipitation storm had commenced. Modeled plume locations closely mirrored field monitoring, however the ability of the model to accurately predict salinity changes through the water column throughout the entire estuary is limited by the large grid sizes utilized and the inaccuracies inherent when estimating runoff volumes generated from storm events.

Accuracy will improve when the model grid size and layer thickness are reduced. Additionally, field measurement of fluvial discharge to the estuary during storm events may contribute to more accurate model inputs leading to better agreement between modeled and monitored results.

Conclusions

Monitoring and modeling of storm events show plume thickness varies both temporally and spatially dependent on storm intensity, duration, and precipitation distribution over the catchment. The freshwater layer was consistently well-defined in the narrow sections of the upper estuary (18–27 km from the estuary mouth), and along the Lane Cove River (13 km from the estuary mouth), however, plumes collapsed, mixing with marine water in the wider, central section of the estuary.

The hydrodynamic model developed for Sydney Harbour adequately demonstrates plume generation and migration. At present, the model may be used to predict plume development and migration, however further adjustment of the model grid and input parameters is required to accurately depict salinity variations and plume thickness, especially in the wider, down-stream section of the estuary. Once these issues are resolved, the model will more reliably predict plume collapse and dispersal of fresh water plumes.

Acknowledgements

We acknowledge the financial support supplied by the Australian Research Council Discovery Grant No. DP0560023 ‘Modelling contaminant dynamics in a well-mixed/stratified estuary’. Additionally we thank Doug Treloar and associates at Cardno Lawson and Treloar for providing expertise regarding hydrodynamic modelling, Paul Craig of Dynamic Solutions for providing expertise and technical support for EFDC and EFDC Explorer, Craig Jones of Sea Engineering for advice regarding modeling estuarine systems and all students and technical staff at the University of Sydney who assisted with field data collection.

References

Cruickshank, B. (2006), *Modelling nutrient load to the Port Jackson estuary, Australia*. Honours Thesis, University of Sydney.

Hamrick, J.M. (1992), *A three-dimensional environmental fluid dynamics computer code: Theoretical and computational aspects*. Virginia Institute of Marine Science, School of Marine Science, The college of William and Mary, Gloucester Point, VA 23062.

Hatje, V., Rae, K., Birch, G.F. (2001), Trace metal and total suspended solids concentrations in freshwater: The importance of small-scale temporal variation, *Journal of Environmental Monitoring*, 3, 251–256.

Institution of Engineers, Australia (1977). *Australian Rainfall and Runoff: Flood Analysis and Design*. In: Pattison, A., Ward, J.K.G., McMahon, T.A., Watson, B. (Eds.), Institution of Engineers, Australia.

O’Donnell, J. (1993), Surface Fronts in Estuaries: A review, *Estuaries*, 16(1), 12–39.

Taylor, S.E. (2000), *The source and remobilisation of contaminated sediment in Port Jackson, Australia*. PhD Thesis, The University of Sydney.

Wolanski, E. (1977), The fate of storm water and stormwater pollution in the Parramatta estuary, Sydney, *Australian Journal of Marine and Freshwater Research*, 28, 67–75.

Modeling tidal flow in large-scale basins

PIETER C. ROOS[1], HENK M. SCHUTTELAARS[2]

1. Water Engineering and Management, University of Twente,
P.O. Box 217, 7500 AE Enschede, Netherlands
email: p.c.roos@utwente.nl

2. Delft Institute of Applied Mathematics, Delft University of Technology, Mekelweg 4,
2624 CD Delft, Netherlands
email: h.m.schuttelaars@ewi.tudelft.nl

Keywords: tidal flow, viscous effects, Taylor problem, collocation method

ABSTRACT

We solve the extended Taylor problem that accounts for viscous effects. The solution, written as a superposition of wave solutions, involves viscous counterparts of the well-known Kelvin and Poincaré modes, as well as a new type of mode. This work is a first step towards an idealized, analytical model for tidal and residual flow in basins with a complex geometry.

Introduction

Tidal basins with arbitrary shapes usually display intricate patterns of tidal and residual flow that are difficult to interpret. To get a better understanding of the water motion, we propose to develop and analyze an analytical model for the flow in large-scale basins with complex geometry on an f-plane. A further advantage of such an analytical method is that it allows us to quickly assess the impact of basin geometry on the flow patterns, including its sensitivity to the associated geometrical parameters. Examples are the natural flow patterns observed in large scale basins (North Sea, Wadden Sea) and those due to human interferences (artificial islands, large-scale land reclamation).

To mimic complex basin geometries, the model domain is constructed as an arbitrary combination of rectangular boxes with uniform depth. The solution is constructed by expanding the surface elevation and the depth-averaged flow field in the Froude number, which is a small parameter, equal to the ratio of the tidal wave amplitude and the water depth. At leading order, the main tidal constituent (e.g., M_2) is modeled. In each box, the spatial structure of the solution is constructed using a superposition of so-called open channel modes, both generalized to account for friction and viscous effects. A collocation method is employed to match the solutions across the interface of adjacent boxes. As it turns out, horizontal viscosity and a no-slip boundary condition are required to obtain a smooth solution. At the next order, the internally generated residual current and the higher harmonics (M_4), forced by nonlinear interactions of the M_2-component, can be calculated using a similar approach.

As a first step in the modeling approach above, we solve the classical Taylor problem (Taylor, 1921), extended to account for viscous effects. We thus focus on the geometry of a semi-enclosed rectangular basin depicted in Figure 1b. After briefly formulating the problem, we investigate the so-called open channel modes (e.g., Ripa and Zavala-Garay, 1999), in terms of which the solution to the viscous Taylor problem is expressed. Finally, we present the conclusions.

Model formulation

Consider a tidal wave of angular frequency ω^* and typical vertical amplitude A^* in a rotating channel/semi-enclosed basin of uniform depth H^* of the order of tens of meters and width B^* of the orders of tens to hundreds of km (See Figure 1. An asterisk denotes a dimensional quantity.) The free surface displacement is denoted by $z^* = \zeta^*$, and we introduce depth-averaged flow velocities $\mathbf{u}^* = (u^*, v^*)$ with components in the along-channel x^*-direction and the cross-channel y^*-direction, respectively. Conservation of mass and

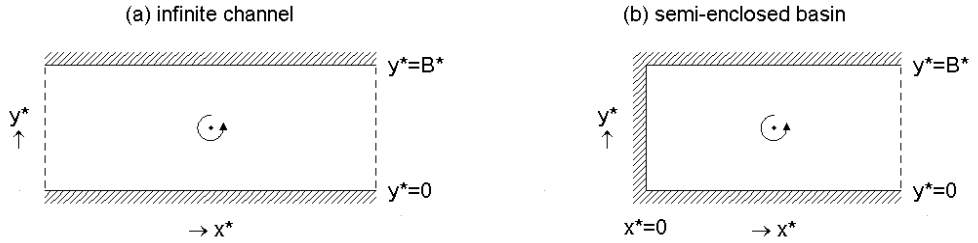

Figure 1. Definition sketch of the geometry: (a) infinite channel with longitudinal boundaries at $y^* = 0$, B^*, (b) semi-enclosed basin with an additional lateral boundary at $x^* = 0$.

momentum is then expressed by the nonlinear shallow water equations. No slip conditions are imposed at the closed boundaries, instead of the no-normal flow condition of the inviscid case.

Next, we introduce dimensionless quantities by scaling against the typical scales of an inviscid Kelvin wave (Pedlosky, 1982): time $1/\omega^*$, horizontal length $1/k^*$ with $k^* = \omega^*/(g^*H^*)^{1/2}$ the Kelvin wave number and g^* the gravitational acceleration), surface elevation A^* and velocity $U^* = A^*(g^*/H^*)^{1/2}$. At lowest order in the Froude number, i.e., at $O(Fr^0)$ with $Fr = A^*/H^* = U^*/(g^*H^*)^{1/2}$, the following set of linear model equations is then obtained (subscripts denoting derivatives, dimensionless quantities without an asterisk):

$$\zeta_x + u_t - fv + \mu u = \nu [u_{xx} + u_{yy}] \quad , \tag{1a}$$

$$\zeta_y + v_t + fu + \mu v = \nu [v_{xx} + v_{yy}] \quad , \tag{1b}$$

$$\zeta_t + u_x + v_y = 0 \quad . \tag{1c}$$

Here, f is a dimensionless Coriolis parameter, μ a dimensionless friction coefficient and ν a dimensionless eddy viscosity. The no-slip condition at the closed boundaries simply reads $u = v = 0$, to be satisfied at $y = 0$, B (with $B = k^*B^*$) and, for the geometry in Figure 1b also at $x = 0$.

The model Equations (1) can be rewritten into three fundamental relationships: the viscous counterparts of the polarization equations (expressing u and v in terms of ζ only), and the so-called viscous Klein-Gordon equation (a single PDE for ζ only). They are given by

$$(L^2 + f^2)u = -[L\zeta_x + f\zeta_y] \quad , \quad (L^2 + f^2)v = -[L\zeta_y - f\zeta_x] \quad , \quad (L^2 + f^2)\zeta_t - L[\zeta_{xx} + \zeta_{yy}] = 0 \quad , \tag{2a, b, c}$$

respectively. Here we have introduced the differential operator $L = \partial/\partial t + \mu - \nu[\partial^2/\partial x^2 + \partial^2/\partial y^2]$. Note that, owing to viscous effects, the viscous Klein-Gordon Equation (2c) is of fourth order.

Open channel modes

For the infinite channel geometry of Figure 1a, we now proceed by seeking wave solutions of the form

$$\zeta(x, y, t) = Z(y) \exp(\mathrm{i}[t - kx]) \quad , \qquad \mathbf{u}(x, y, t) = \mathbf{U}(y) \exp(\mathrm{i}[t - kx]) \quad , \tag{3a, b}$$

with cross-channel structures Z(y) and $\mathbf{U}$(y), respectively. The complex wave number k is to be obtained from the subsequent analysis. Without going into the mathematical details, we find the following cross-shore structure for the surface elevation (similar for the flow field):

$$Z(y) = A_1 \exp(-\alpha y) + A_2 \exp(\alpha[y - B]) + A_3 \exp(-\beta y) + A_4 \exp(\beta[y - B]) \quad . \tag{4}$$

The quantities $\pm\alpha$ and $\pm\beta$, obtained as the roots of a fourth order characteristic polynomial equation, have a direct physical meaning. In Equation (4), the first two terms with coefficient α represent the wave structure in the interior of the channel domain, already present in an inviscid analysis. The third and fourth term represent the two boundary layers on either side of the channel, the width of which scales with $\nu^{1/2}$.

Next, imposing no-slip at both channel boundaries gives a homogeneous linear system for the coefficients A_1, A_2, A_3 and A_4. To obtain nontrivial solutions, a solvability condition must be satisfied, from which the wave number(s) k can be determined. To this end, we combine an analytical method, i.e., expanding k, α and β in powers of $\nu^{1/2}$, with a numerical search routine. We thus identify the following wave solutions, termed open channel modes (see Figures 2 and 3):

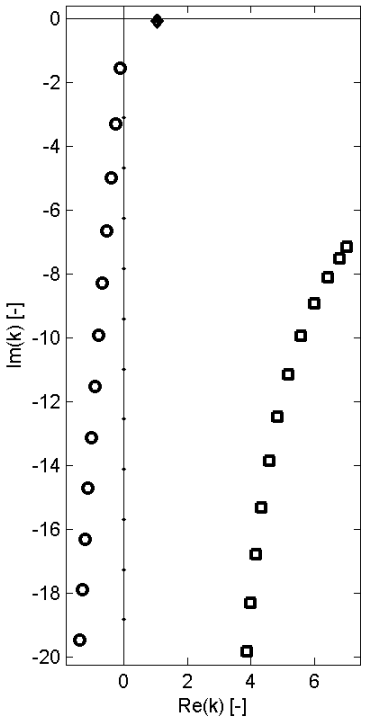

Figure 2 (left). Open channel modes, plotted as points in the complex wave number plane: the viscous Kelvin mode (diamond), viscous Poincaré modes (circles, truncation number $M = 12$) and the new type of modes (squares, $M = 12$). The inviscid counterparts are indicated by black dots. Parameter values: $f = 0.8$, $\nu = 0.01$, $\mu = 0$, $B = 2$. Note: due to the point symmetry in $k = 0$, it is sufficient to plot the modes with $\mathrm{Im}(k) \leq 0$.

Figure 3 (below). Cross-shore structure of the open channel modes. Top: viscous Kelvin mode (solid, $m = 0$). Rows below: Poincaré modes (solid, $m = 1, 2, 3$) and the new type of modes (dashed, $m = -1, -2, -3$). Note the differences in vertical axis scales. Moreover, only the absolute values have been plotted; arguments/phases have been omitted. For parameter values, see the caption of Figure 2.

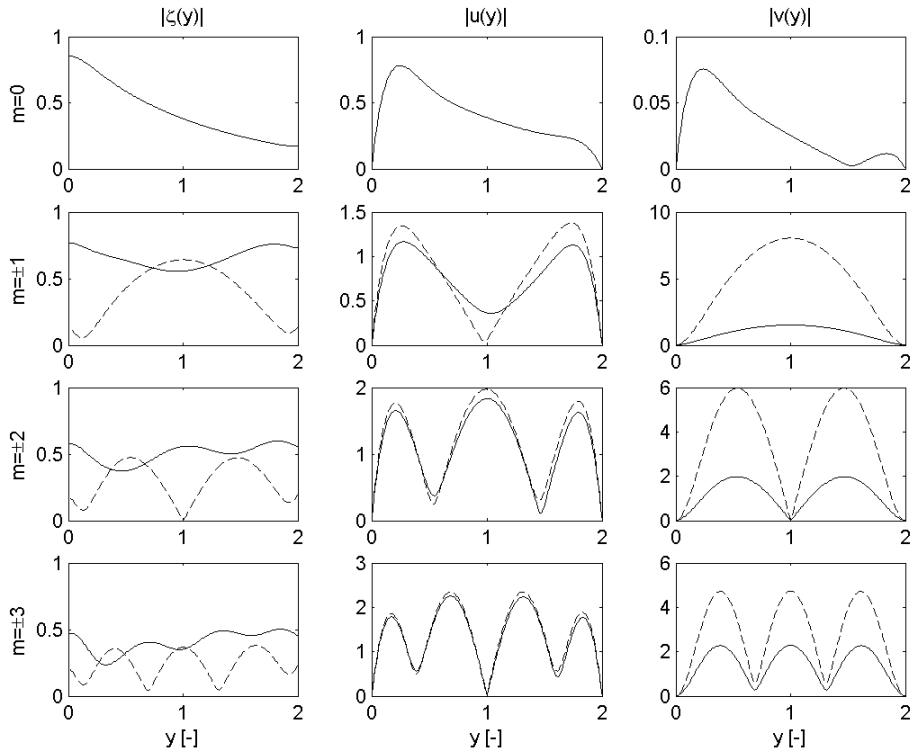

- The *viscous Kelvin mode* (denoted by a diamond in Figure 2) is the viscous counterpart of the classical Kelvin wave, showing exponential decay in the cross-shore direction. Apart from the two boundary layers mentioned above, the viscous Kelvin wave displays amplitude decay in the direction of propagation and the wavelength is slightly smaller than in the inviscid case. These effects resemble those of bottom friction (Rienecker and Teubner, 1982).
- *Viscous Poincaré modes* (circles in Figure 2) are the viscous counterparts of the classical Poincaré modes, which have a harmonic lateral structure and – depending on the channel width – are free or evanescent. The longitudinal length scales are slightly smaller than in the inviscid case.
- Finally, a *new type of mode* (squares in Figure 2) emerges, the presence of which is entirely due to viscous effects. These are purely evanescent waves with a longitudinal decay distance bounded by $\nu^{1/2}$. For every Poincaré mode, there is a new mode with a rather similar cross-shore structure.

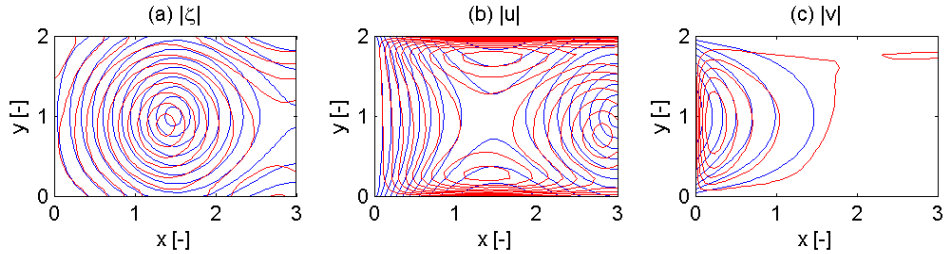

Figure 4. Contour plot of the Taylor solution ($M = 12$), both inviscid (blue) and viscous (red): (a) free surface amplitude $|\zeta(x, y)|$, (b) along-channel amplitude $|u(x, y)|$, (c) cross-channel amplitude $|v(x, y)|$. For parameter values, see the caption of Figure 2.

Viscous Taylor problem

Now let us turn to the viscous Taylor problem, with the semi-enclosed basin geometry as depicted in Figure 1b and an incoming Kelvin wave from $+\infty$. Key step is to write the solution as a superposition of the viscous open channel modes, obtained in the previous section. We thus consider a truncated sum of an incoming Kelvin wave, a reflected Kelvin wave, M Poincaré modes and M new modes:

$$\zeta(x, y, t) = Z_0(B - y)\exp(\mathrm{i}[t + k_0 x]) + \Sigma_{m=-M..M}\, C_m\, Z_m(y)\exp(\mathrm{i}[t - k_m x]) \quad . \tag{5}$$

The Kelvin mode is indicated by the subscript $m = 0$, whereas the Poincaré modes are indicated by positive subscripts and the new modes by negative subscripts. The first term in Equation (5) corresponds to the incoming Kelvin wave: traveling in the negative x-direction, with amplitude fixed to unity at $x = 0$. For the flow field an expression similar to Equation (5) holds.

The above solution involves $2M + 1$ complex coefficients C_m, to be determined from the no-slip boundary condition along the lateral basin boundary $x = 0$. To this end, we adopt a collocation method. Defining $y_n/B = n/(2M + 2)$ for $n = 1, 2, \ldots, 2M + 1$, we require the *longitudinal* velocity to vanish at the $M + 1$ collocation points $(0, y_{2n+1})$ with an odd index; and we require the *lateral* velocity to vanish at the M intermediate collocation points $(0, y_{2n})$ with an even index. This leads to a linear system of $2M + 1$ equations and $2M + 1$ unknown coefficients C_m.

For the parameter values listed in the caption of Figure 2 and a truncation number $M = 12$, the viscous and inviscid solution are depicted in Figure 4. The viscous solution clearly shows boundary layers along the closed boundaries, the lateral boundary layer being formed by the new type of modes. Compared to the inviscid solution, the amphidromic points have shifted slightly. This is mainly due to viscous dissipation, which triggers amplitude decay in the direction of Kelvin wave propagation.

Conclusions

We have solved the extended Taylor problem that accounts for viscous effects. As part of our analysis, a new type of open channel mode has been identified, the existence of which is entirely due to viscous effects. These modes turn out to create the transverse boundary layer at the closed end of the semi-enclosed basin.

The next steps are the following. The first step is to investigate the flow pattern (residual and M_4) obtained at first order in the Froude number, i.e., at $O(Fr^1)$, and triggered by nonlinear interactions of the M_2-tide. The second step, as pointed out in the Introduction, is to create more complex geometries as an arbitrary combination of rectangular boxes. These two steps will allow us to compare with flow patterns observed in e.g., the North Sea and Wadden Sea and to assess the impact of human interferences on tidal flow patterns.

References

Pedlosky, J. (1982), *Geophysical Fluid Dynamics*. Springer-Verlag, New York. 624pp.

Rienecker, M.M., Teubner, M.D. (1980), A note on frictional effects in Taylor's problem, *Journal of Marine Research*, 38, 183–191.

Ripa, P., Zavala-Garay, J. (1999), Ocean channel modes, *Journal of Geophysical Research*, 104(C7), 15479–15494.

Taylor, G.I. (1921), Tidal oscillations in gulfs and rectangular basins, *Proceedings of the London Mathematical Society*, 20(2), 148–181.

Extracting 'free-stream' tidal current energy in estuaries

DAVID PRANDLE

Department of Earth and Ocean Sciences, University of Liverpool,
4 Brownlow Street, Liverpool L69 3GP UK
email: davidprandle@hotmail.com

Keywords: tidal-stream energy, renewable energy

ABSTRACT

This paper examines the power potential and feasibility of extracting tidal-stream energy in estuaries. The net power available at any cross section is derived and compared with equivalent values associated with impounded-barrier schemes. To provide a perspective on the impact of energy extraction on overall estuarine dynamics, this net power is also compared with the (upstream) energy dissipation from bed friction. The practicalities of extraction are examined for deployments which span various fractions of a cross-section. It is shown that 'fences' spanning large fractions are required for effective energy extraction. Similarly it is shown that to avoid excessive increases in current speed outside of the 'fence', some channeling of flows upstream and downstream of devices may be necessary.

Introduction

Recent pressures to exploit 'renewable' energy sources have led to renewed interest in the extraction of tidal energy within estuaries. Unlike wind or wave energy, tides are entirely predictable for decades ahead. Small scale tidal mills have operated in estuaries for centuries. However, despite long-standing interest in large-scale 'impounded-barrier' schemes in many countries, La Rance in France is the only full-scale scheme, (250 MW), remaining in successful operation since 1978. A similar sized Korean scheme, SIHWA, (256 MW) is under construction and is scheduled for completion in 2009 (www.tidaltoday.com).

This lack of development can be related to several complicating factors which hinder energy extraction from impounded barrier schemes. These include:

1) Net energy yield only ~27% of available value for one-way ebb generation or ~37% for two-way (at the cost of more expensive turbines). Energy production limited to 55% of time for both one-way and two-way operations (Prandle, 1984).
2) The ubiquitous 15-day spring-neap tidal cycle introduces a typical 2:1 variation in range translating into a 4:1 (or more) variation in available tidal energy.
3) Operational characteristics result in approximate halving of tidal range and flow rate upstream of the barrier. Such changes are likely to have significant and uncertain impacts on: land drainage, saline intrusion, flushing rates, sedimentation patterns and longer-term morphological evolution.
4) The economic viability depends on the ratio of alternative (oil/gas) energy costs to capital repayment charges. However, construction costs for 'one-off' marine projects are notoriously unpredictable. Similarly, projections of both factors over design lives in excess of 50 years are difficult and may change appreciably over the decade or so between the start and completion of construction.

Table 1. Characteristics of tidal energy schemes

Parameter	***Theory*** (Prandle, 1984)	**La Rance**	**Korea**	**Fundy**	**Bristol Channel**	**Units**
Surface area		22	56	86	420	km^2
Tidal amplitude, A		4.25	4.0	5.0	4.0	m
$E_{max} = 4\rho g A^2 S/P$		350	360	1900	5900	MW
Actual output	*27*	16	17	20	19	%
Rated head, h	*1.2*	1.3	1.4	1.3	2.2	h/A
Rated flow, q	*0.4*	0.5	0.2	0.4	1.9	q/Q

By contrast, deployment of free-stream tidal-current devices can offer immediate energy production from a single unit with relatively little environmental impact.

Energy availability

Horizontal axis turbines can extract a fraction, α, of the stream energy $\frac{1}{2}\rho U^3$. Over a cross-sectional breadth, B, and depth, D, the mean rate of free-stream energy available, E_U, is

$$E_U = 2\,\alpha\, B\, D\, \rho U^3/(3\pi) \tag{1}$$

for an oscillatory tidal current, $U \sin \omega t$, with $\omega = 2\,\pi/P$, P tidal period.

The corresponding maximum energy extraction from an impounded barrier scheme, E_B, is

$$E_B = 4\,\rho g Z^2 S/P \tag{2}$$

where Z is the tidal elevation amplitude and S the surface area of the impounded basin.

It is convenient to introduce the approximation that the upstream volume is equal to the net flood flow in the form

$$2Z\,S = (2/\pi) B\, D\, U\, P/2. \tag{3}$$

Hence from (1), (2) and (3), the ratio R_E of energy available from tidal streams to that from barriers is

$$R_E S = E_U/E_B \quad = \quad \tfrac{1}{3}\,\alpha\, U^2/\mathrm{g}\,\mathrm{Z}. \tag{4}$$

Prandle (2004), derived the following relationship between tidal current and elevation in 'synchronous' estuaries

$$U = \mathrm{Z}(2g/D)^{0.5}/[1 + (F/\omega)^2]^{0.5} \tag{5}$$

where D is the depth of a triangular shaped cross section and the linearized friction parameter, $F = 1.33 f U/D$, with $f \sim 0.0025$ representing the 'quadratic' bed friction factor.

For typical values of $\alpha = 0.5$, R_E increases from about 0.5% in micro-tidal estuaries ($Z < 1$ m) up to 2% in macro-tidal estuaries ($Z > 3$ m). As noted earlier, extraction from impounded barrier schemes is limited to about 37% for two-way operation or 27% for one-way. Thus generally, free stream energy availability represents only a small fraction of that from barrier schemes. While multiple 'fences' of free-stream turbines can be located at suitable spacings along an estuary, it is unlikely that net energy extraction will rival that from barrier schemes.

To provide a scaling perspective on actual magnitudes of energy production, we assume a triangular cross section with side slope 0.01. Estimates of E_B then range from 100 to 1000 MW, the latter in the deeper, macro-tidal estuaries with production reaching 7000 MW for $D = 40$ m and $Z = 4$ m. By contrast, free-stream extraction ranges from 1 to 25 MW rising to 100 MW in the deepest, macro-tidal estuaries.

A reasonable estimate of the maximum tidal energy available is provided by the 'upstream' energy dissipation, E_F, given by

$$E_F = 0.25\,\rho g\, BDZU \cos\theta \tag{6}$$

where θ is the phase difference between U and Z given by

$$\tan\theta = F/\omega. \tag{7}$$

Calculations of the ratio of E_U:E_F range from 1% in shallow estuaries to 2.5% in deeper waters. This illustrates that installation of multiple 'fences' of free-stream turbines should generally be possible. In deeper water, inertia can predominate over friction and substantially increase the amount of tidal energy available above that indicated by E_F.

A further part of this study illustrates that for effective capture of the available free-stream energy, 'fences' must extend over more than half of the cross-sectional area . Moreover, spacing between successive fences must be at least ten times the mean water depth.

References

Prandle, D. (1984), Simple theory for designing tidal power schemes, *Advances in Water Resources*, 7, 21–27.

Long-term development of the tsunami-affected coast

ELLA MEILIANDA[1], SUZANNE J.M.H. HULSCHER[1], C. MARJOLEIN DOHMEN-JANSSEN[1], BEN H.P. MAATHUIS[2], KATHELIJNE M. WIJNBERG[1]

1. Water Engineering and Management, University of Twente, P.O. Box 217, 7500 AE Enschede, Netherlands
email: e.meilianda@utwente.nl, s.j.m.h.hulscher@utwente.nl, c.m.dohmen-janssen@utwente.nl, k.m.wijnberg@utwente.nl

2. Water Resources, International Institute for Geo-information Science and Earth Observation (ITC), P.O. Box 6, 7500 AA Enschede, Netherlands
email: maathuis@itc.nl

Keywords, coastal morphology, geomorphological interpretation, post-tsunami evolution, conceptual model; Banda Aceh coastal plain

ABSTRACT

Banda Aceh city is located in the triangular shape of coastal plain between the two headlands (Figure 1) on the northwest tip of Sumatra Island, Indonesia. Two inland tectonic fault systems are situated on the island; i.e. the Sumatran Fault System at the western side and the Seulimum Fault System at the eastern side of the coastal plain. Apart from these, a major continental crust subduction zone is located 300 km offshore along the western coast of Sumatra. Displacement of this rupture zone has triggered an earthquake of 9.0 on Richter scale which subsequently triggered the tsunami on 26 December 2004. The coastal plain of Banda Aceh has a complicated morphology. The destructive earthquakes and tsunami waves caused a sudden and massive change in the morphology of the low-lying coast of Banda Aceh.

The main objective of this study is to build a conceptual model of the future morphological development of the coast after being destroyed by the earthquakes and tsunami. The principle underlying this study is to understand the morphological development in the past that led to the pre-tsunami's coastal morphology, and use this information to construct a conceptual model for the morphological development in the future.

Data and geomorphological interpretation

Very limited information is available about the morphological processes leading to the formation of the Banda Aceh coastal plain at present. Long-term morphological processes leading to the present day coastal plain has never been thoroughly investigated. This study tries to interpret the processes that influence the coastal morphology on a time scale of hundred years from a geomorphological perspective. This has two main objectives: The first is to determine the spatial extent of the earthquake and tsunami impact and investigate the existence and development of the pre-tsunami's morphology of this specific area in the past. The second is to determine the magnitude of some specific coastal morphological parameters and the controlling factors that determine these magnitudes (e.g., tectonic activity, wind direction, rainfall, etc.). In this case, the net sediment transport rate and direction are the parameters under consideration. Using this information, some scenarios are set up of what might happen in future under different forcings, e.g., severe erosion due to tsunami, land subsidence and the re-distribution of tsunami-related sediments.

Eight sets of historical topographic maps and nautical charts of Banda Aceh plain from 1898 to 1978 and six sets of satellite images from 1989 to 2005 are utilized to map the coastline change and to interpret the morphological processes leading to the recent coastal morphology. Historical rainfall and wind direction of 20th and 21st centuries are collected to obtain historical climate records. Study of Holocene sea level fluctuations at Malaysian Peninsula by Tjia (1992) is referred to interpret the formation time of some prominent coastal features such as old beach ridges and perched beach barriers.

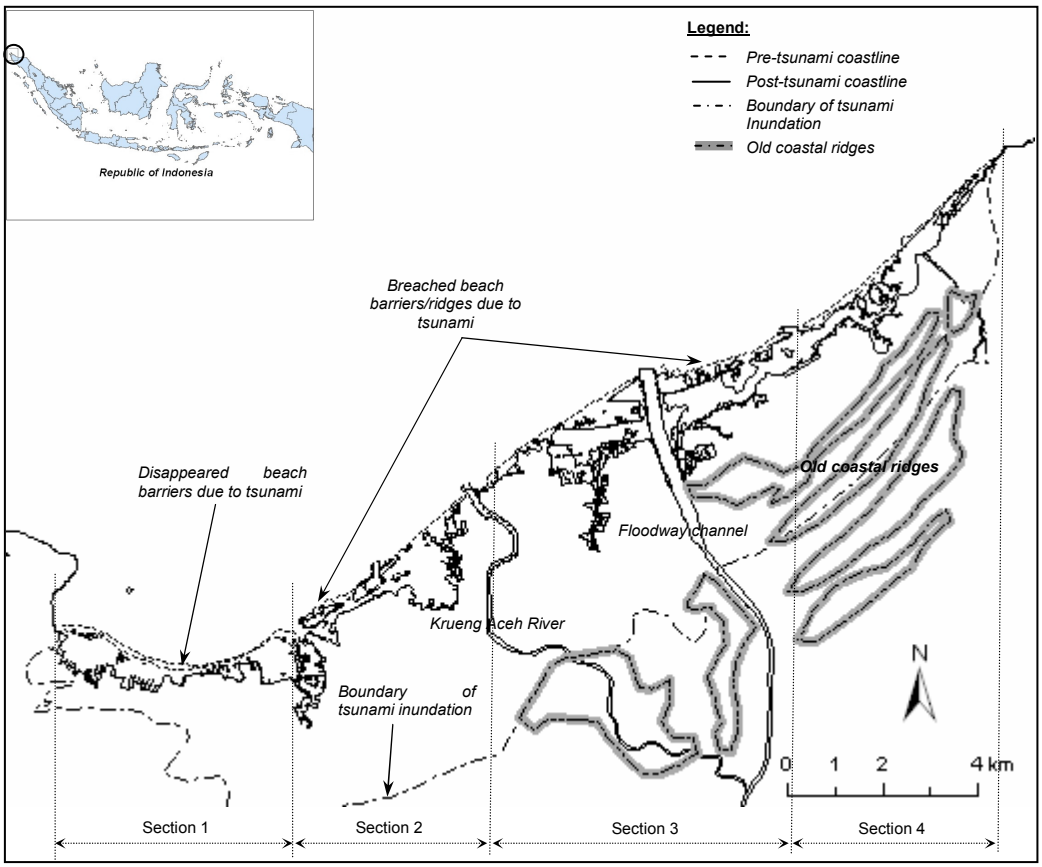

Figure 1 Morphology of Banda Aceh coastal plain and the effect due to the earthquake and tsunami.

Morphological interpretation of coastal development in the past

Within the extent of the affected region, the pre-existing coastal plain consists of some prominent morphology. Multiple coastline-oriented coastal ridges and swales can be found on the northeastern section of the (sub aerial) coastal plain, situated from an elevation of 6.5 m above mean low water level (MLWL) towards the coastline where the front-row beach barrier (1.0 to 1.5 m above MLWL) is perched in front of the coast-parallel lagoon system.

The perched beach barriers which are connected with narrow sandy beach strips have been formed since 700 BP, interpreted from the study of Holocene sea level fluctuation in the region by Tjia (1992) and Verstappen (2000). The bathymetric profiles (available at several locations alongshore) together with this observation indicate that the coastal plain tilted down southwestward due to tectonic activities during this period. The abnormal coastline which is connected to the inner curve of the headland (instead of to the tip of the headland) on the southwest is also a good indication of this situation. As a result, towards the southwestern section of the coast beach ridges no longer exist. In stead, a lower elevation sandy beach barrier is present here (Figure 1).

More recent developments (i.e., over the past 100 years) indicate that the coastal processes were influenced by the fluctuations in sediment supply, either from marine sources or from the river. Historical data of rainfall and wind directions coincide with this fluctuation. The monsoonal climate not only determines the annual net sediment transport (i.e., resulting from seasonal changes in the direction of littoral transport), but also by accumulation, the decadal net sediment transport rate and direction. The latter is quantified by the growth of sand spits and the advancing or retreating coastline positions.

Littoral transport rates were amplified by predominant winds (and thus waves) and sea current of Malacca Strait from the northeast in the period of 1967–1978, causing a reverse in the direction of net sediment transport (i.e., usually towards the northeast) and a corresponding northeastern sand spit migration. On the other hand, since 1978–1989 human intervention has started to change the sediment transport from the river and from the coastal area due to river normalization and sand mining. Predominant wind direction from the

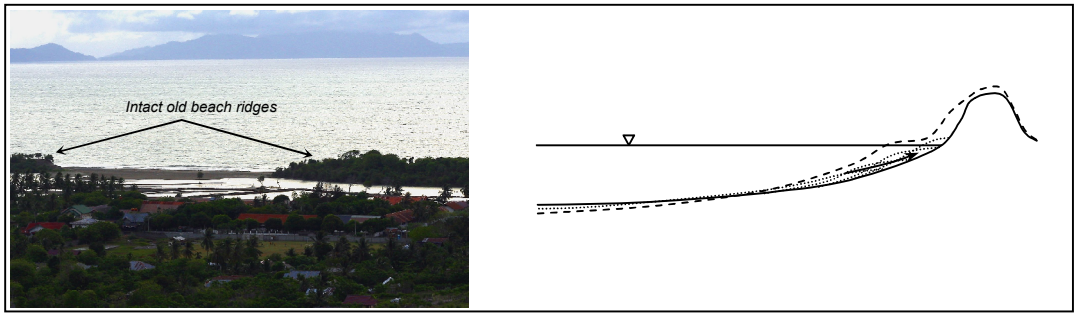

(a)

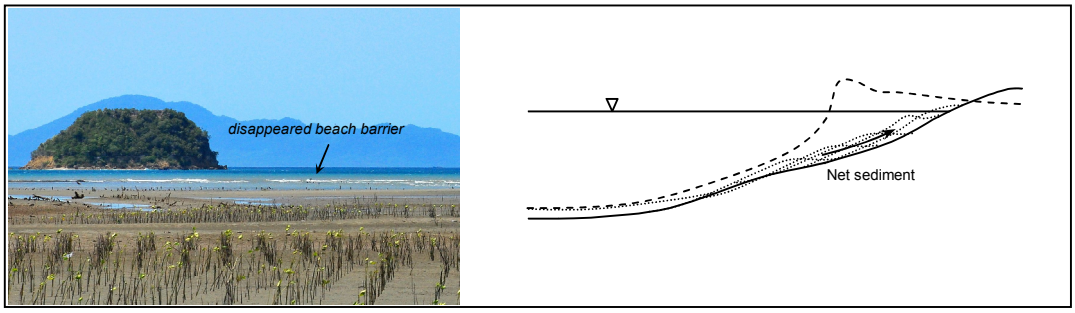

(b)

Figure 2. Conceptual model schematization of morphological development of a tsunami-affected coast. (a) Sandy beach strip connects the remnant of beach ridges on section 4; (b) Initial beach barrier was destroyed on section 1, replaced by development of instable sand bars. Note: Pictures were taken in May 2008; dashed line denotes the initial profile; black line denotes profile due to earthquake and tsunami.

west and northwest (i.e., almost perpendicular to the coastline) led to a built up trend of the coast towards 2000s. In the 1990s, Krueng Aceh River was bifurcated by an artificial floodway channel and coastal protections were started to be built. These two aspects have to some extent caused a disruption of sediment transport. Combination of these factors may cause reduction of sediment supply in the littoral zone which led to reduction of sand spit growth. Beach erosion due to cross shore transport was prominent at some sections. This 'negative' trend of net sediment transport is expressed as an average rate of coastline change on a hundred-year time scale of -0.52 m yr^{-1}, 0.01 m yr^{-1}, -1.88 m yr^{-1} and -0.27 m yr^{-1} (negative numbers denote coastline retreat) for sections 1, 2, 3 and 4, respectively.

Conceptual model for the future scenario

For the next hundred years it is assumed that the pre-dominant monsoonal wind direction (53% of occurrence) follows the trend of the past ten years (i.e., west direction). Consequently, section 1 and section 2 will not receive sediment supply from the Krueng Aceh River. Erosion of the headland's cliff on the west may be the main source of sediment to these sections. Sediment supply from Krueng Aceh River is responsible for the development of the coastline at section 3, which in the recent decades has shown some sediment deficit. The second dominant monsoonal wind from the northeast (40% of occurrence) combined with cliff erosion from the Ujong Batee headland results in accumulation of sediment as far as section 4.

Along the entire coastal stretch sediment will also come from a re-distribution of tsunami-deposited sediment from the shoreface. This process is thought to be one of the important factors to consider in addition to the more rapid process of littoral transport over a hundred-year time scale of coastal morphological development. In addition, there is evidence of tectonic subsidence which occurred as a consequence of the earthquakes of 26 December 2004, and 8 March 2005 with a magnitude of 8.0 on Richter scale. Some observed points along the affected coastal plain indicate a subsidence magnitude of 0.5 m on average.

With the condition of the shoreface being out of equilibrium due to deposition, there is an opportunity that the rate of sediment transport will be 'positive' (i.e., coastline advancing). Nevertheless, due to the dramatic

change of the upper shoreface profile and the land subsidence leading to coastal retreat, the advancement would start from the new coastline after the tsunami. For instance, at the coastal sections where remnants of the breached old beach barriers are present, such as in section 2, section 3 and section 4, the new beach will re-connect the old beach barriers (Figure 2a). However, at section 1, where the beach barrier completely disappeared due to the tsunami, the new beach may develop as unstable sand bars which eventually may be connected to the new beach of the new coastline (Figure 2b).

Conclusions

Tectonic activities played a leading role in morphological development of Banda Aceh plain in the geological time scale. Beach ridges, perched beach barriers and lagoon systems are prominent coastal features that formed as the boundary of the more recent morphological development.

Monsoonal climate leading to trends in wind directions is the main factor which influences the development of the morphology of Banda Aceh coastal plain on a hundred-year time scale. Influenced by the climate and human intervention, sediment supply from the river to the littoral zone may change the regime of the littoral transport.

The earthquake and tsunami have changed the coastal morphology dramatically. It is not likely that the new beach strips will have the same geometry and position as the old one within 100 years. This is due to the fact that some coastal features (e.g., beach barriers) developed on a time scale much longer than 100 years (geological time scale) and requires different morphological processes. Rates of net sediment transport at Banda Aceh coast were quite small due to the alternating trend of the monsoonal wind. This is also because the coast is a semi-protected coast with a narrow continental shelf. In the next hundred years after the tsunami event, new narrow sandy beaches may still develop dynamically towards a new equilibrium.

References

Tjia, H.D. (1992), Holocene sea-level changes in the Malay-Thai Peninsula, a tectonically stable environment, *Geological Society of Malaysian Bulletin*, 31, 157–176.

Verstappen, H.Th. (2000), *Outline of the geomorphology of Indonesia*. ITC publication No. 79, International Institute for Aerospace Survey and Earth Sciences, Enschede, Netherlands, 212pp.

Changing coastlines: data assimilation for morphodynamic prediction and predictability

SARAH L. DANCE[1], TANIA R. SCOTT[2], MICHAEL J. BAINES[1], AMOS S. LAWLESS[1], DAVID C. MASON[2], NANCY K. NICHOLS[1], ROGER PROCTOR[3], POLLY J. SMITH[1], PETER K. SWEBY[1]

1. Department of Mathematics, University of Reading, Reading RG6 6AX UK
email: s.l.dance@reading.ac.uk, m.j.baines@reading.ac.uk, a.s.lawless@reading.ac.uk
n.k.nichols@reading.ac.uk, p.j.smith@reading.ac.uk, p.k.sweby@reading.ac.uk

2. Environmental Systems Science Centre, University of Reading,
Reading RG6 6AL UK
email: trs@mail.nerc-essc.ac.uk, dcm@mail.nerc-essc.ac.uk

3. Proudman Oceanographic Laboratory, 6 Brownlow Street, Liverpool L3 5DA UK
email: rp@pol.ac.uk

Keywords: coastal morphodynamic modeling, data assimilation;
Dee estuary, Morecambe Bay

ABSTRACT

Operational coastal flood forecasting is limited near-shore by lack of knowledge of evolving bathymetry. Obtaining a full bathymetric survey can be time-consuming and expensive, and is not generally possible just prior to a storm event. A more attractive option may be to use a coastal area morphodynamic model with data assimilation to maintain up-to-date model bathymetry in anticipation of such an event. Data assimilation provides a means to combine model predictions with observations to give more accurate forecasts. It also enables uncertainties in the forecasts to be calculated. Predictions of future bathymetry with specified uncertainty would be useful for coastal flood risk management purposes. In this paper we describe the application of data assimilation techniques to coastal area morphodynamic modeling. Two study sites are considered: the Dee estuary and Morecambe Bay.

Introduction

Knowledge of near-shore bathymetry, as estimated by a morphodynamic model, can be useful for navigation purposes, or to act as input to coastal flood inundation models during a storm event. Predictions of future bathymetry are also useful. For example, environmentalists want to know about potential habitat loss, port authorities want to know if the channels into their docks will remain open, and engineers want to know if their flood defense works will provide the desired protection.

Unfortunately coastal morphodynamic modeling is challenging. This is due to difficulties in modeling the underlying physical processes, in setting the initial state of the model, and in setting the model parameters. Data assimilation is a technique that can help with these problems, by making optimal use of model and observation resources. It also allows information to be gained about the uncertainty of the model state.

While data assimilation has been used in atmospheric and oceanic prediction for some years, it has rarely been used for coastal morphodynamic modeling, despite the availability of suitable observations from a variety of sources. However a recent feasibility study showed that data assimilation does have the capability to improve morphodynamic modeling, as illustrated in Figure 1. This study was a precursor to the current Changing Coastlines project, in which we aim to make much greater use of the information available as part of the data assimilation process. The aims of the current project are to

1. Develop morphodynamic models and assimilation systems for at least two study sites
2. Evaluate model predictability and uncertainty, both with and without data assimilation
3. Investigate data assimilation for morphodynamic model parameter estimation
4. Investigate optimal observation strategies for coastal monitoring.

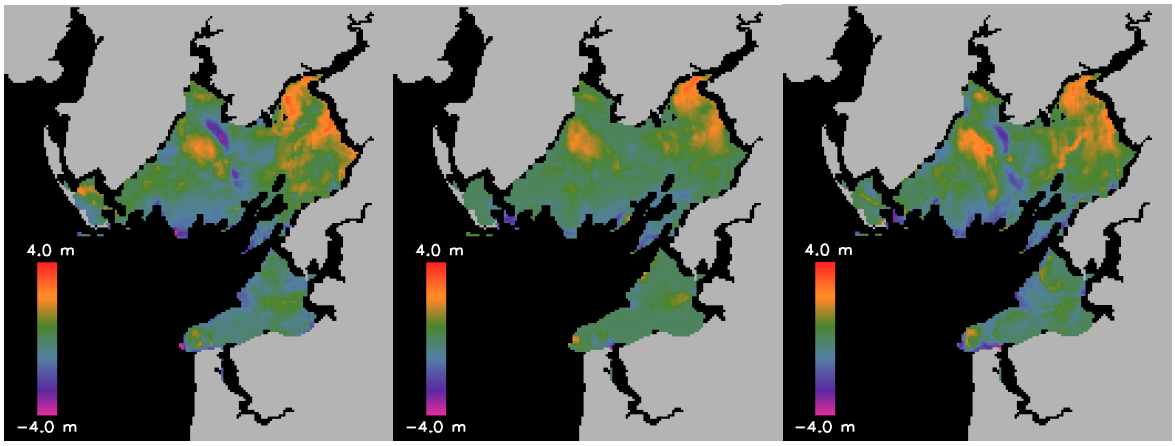

Figure 1. Change in Morecambe Bay bathymetry over a 3-year period (Scott and Mason, 2007). Left: observed change. Middle: modeled change without data assimilation. Right: modeled change with data assimilation.

The remainder of this paper will focus on the first two of these aims. The third aim is considered by Smith et al. (2008).

Study sites

Our project has two identified study sites, the Dee estuary and Morecambe Bay. These are both macrotidal environments in the UK with extremely mobile channels, as can be seen in Figure 2 for Morecambe Bay. The Dee estuary was selected because of the extensive availability of data and will be used for the development of techniques. Morecambe Bay was selected because of our familiarity with this site and will be used for the validation of techniques. We also hope to look at a third, as yet unspecified, site, with a different tide/wave regime, in which to examine the more general applicability of our work.

Morphodynamic model

A coastal morphodynamic model aims to predict changes in bathymetry caused by water based transport of sediment. There are various types of morphodynamic model, but we will use a process-based model which represents the underlying physical processes that lead to morphological change. At the most basic level, water action transports sediment, which alters the bathymetry, which alters the water action, and so on. Although these processes occur simultaneously, it is possible to de-couple the physical equations into those describing the hydrodynamics, and those describing the sediment transport and the resulting change in bathymetry. This makes the model easier to implement, and is possible because the bathymetry changes relatively slowly relative to the tidal flow conditions. Our model will thus have two main components: a hydrodynamic model to predict tidal water flow for given bathymetry, and a bathymetric model to predict change in bathymetry for given tidal water flow.

The hydrodynamic model is a 2DH tide model developed by the Proudman Oceanographic Laboratory (Mason et al., 1999). The bathymetric model is our own. It calculates sediment transport rates and solves a sediment conservation equation. Essentially, if the rate of sediment entering a model grid cell is greater than that leaving the cell than accretion occurs, and vice versa.

We will calculate the sediment transport rates using a standard formula $q = A\,u^n$, where q is the sediment transport rate in the direction of the depth-averaged current u, and A and n are parameters (Soulsby, 1997). We may also include some extensions to this formula, for example to include wave effects, and a critical current below which sediment transport will not occur. Parameters A and n are usually set by calibrating against observations, but we ultimately hope to use data assimilation to achieve this (Smith et al., 2008). The sediment conservation equation is historically solved numerically using a Lax-Wendroff type scheme. However these schemes are notorious at causing dispersion and introducing high frequency oscillations into the solution. Recently some alternative schemes have been proposed, and we intend to try that of Long et al. (2008).

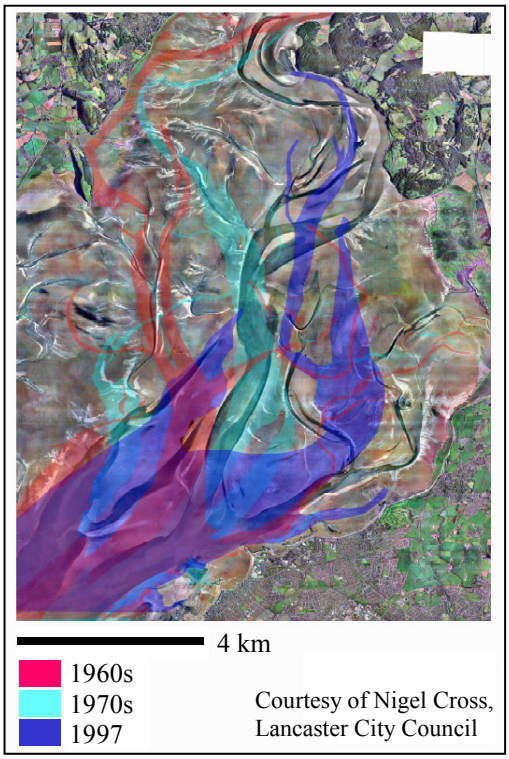

Figure 2. Channels in Morecambe Bay can move by several kilometers in just a few years.

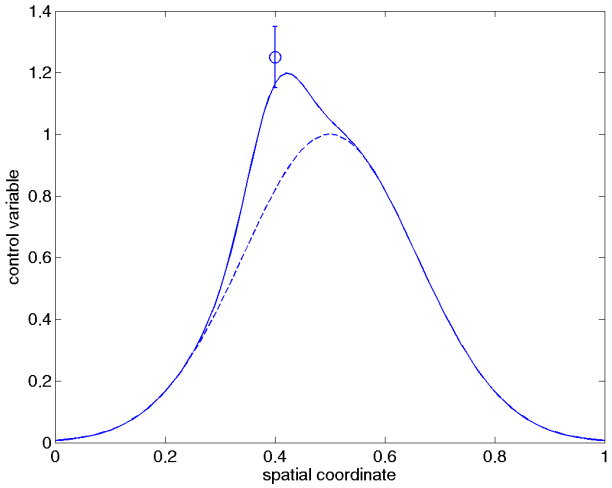

Figure 3. An illustration of data assimilation. The dotted line is a forecast of the model state at the time of an observation. It is prescribed to have errors with Gaussian correlations and a variance of 0.2. The single observation, represented by the circle, has an error bar indicative of the standard deviation of the observation error. The solid line is the new model state that would be obtained by applying 3D-Var in this situation.

Data assimilation

Data assimilation is a sophisticated mathematical procedure by which model predictions can be combined with observations to improve the current state of the model, taking into account the uncertainties in the model predictions and observations. For this work we have chosen to use the data assimilation scheme known as three-dimensional variational assimilation (3D-Var) (Nichols, 2003; Smith et al. 2008).

In this scheme we use our morphodynamic model to forecast to the time of an observation, or set of observations. This forecast model state provides us with a background estimate of the true state. The 3D-Var algorithm then finds a new model state that minimizes a cost function measuring the misfit between the new state, the background state, and the observations. A simple demonstration of assimilation is given in Figure 3.

Once the new model state has been found, this can be used as a new estimate of bathymetry for the morphodynamic model. The model can then be used to forecast to the time of the next observations, and the assimilation process carried out again. This cyclical approach using the dynamical forecast model allows information from past observations to be propagated forward in time and advected across the domain, allowing for much greater observational impact.

Several other dynamic data assimilation schemes are currently popular, such as the ensemble Kalman filter and 4D-Var. However, since the aim of this project is to demonstrate the utility of data assimilation for morphodynamic prediction rather than to develop an operational system, we chose a scheme that we believe offers greater numerical robustness than the Kalman filter variants, and which is easier to implement than schemes such as 4D-Var, that require model adjoints to solve the minimization problem.

Data

Data are integral to the project. Observations are needed to create an initial model bathymetry for each site, to use for data assimilation, and to verify model results. We have assembled an extensive collection of data for each of our study sites, as detailed in Tables 1 and 2. Most of these observations are direct measurements of the bathymetry, and are thus easy to use for all of the above purposes. However the SAR satellite images are radar images which simply show which parts of the coastal zone are under water. These images must be processed to give what is essentially a contour of the bathymetry, which follows the instantaneous shoreline visible in the SAR image (Mason et al., 1999).

1. Dee estuary		
Date	Data type	Source
Apr 2003	LiDAR (full survey)	EA[a]
Jul 2003	Swath bathymetry (main channel)	EA
Feb 2004	LiDAR (full survey)	EA
May 2004	LiDAR (full survey)	EA
Oct 2006	LiDAR (full survey)	EA
Apr 2003 – Aug 2006	29 SAR images	ESA[b]

2. Morecambe Bay		
Date	Data type	Source
Dec 2003	LiDAR (partial survey)	EA
Nov 2004	LiDAR (partial survey)	EA
Feb 2005	Swath bathymetry (low-water channels)	HR Wallingford & Bridge Across the Bay
Mar 2005	LiDAR (partial survey)	EA
Nov 2005	LiDAR (partial survey)	EA
Nov 2005	LiDAR (full survey)	Lancaster City Council
2005?	GPS ground surveys	Lancaster City Council
Feb 2006 – May 2006	LiDAR (partial surveys)	EA
May 2003 – Feb 2007	36 SAR images	ESA

Tables 1 and 2. Data for the Dee estuary and Morecambe Bay.
[a]Environment Agency of England & Wales
[b]European Space Agency

Given our data availability, we will run the Dee estuary model from April 2003 to October 2006. The April 2003 lidar survey will be used as an initial bathymetry, while the October 2006 lidar survey will be used for model validation. We will run the Morecambe Bay model from late 2003 to late 2006, with initial and validation bathymetries created by merging information from different subsets of the SAR images (Mason et al., 1999). In both cases, all remaining data will be used for both data assimilation and model validation.

Conclusions

The paper has given an outline of our project, which is examining how data assimilation can be used to improve coastal area morphodynamic modeling. Although we have yet to produce any results, we are well on the way to developing our model systems, and have acquired a substantial amount of data. These data will allow us to make a comprehensive assessment of the benefits of data assimilation for coastal area morphodynamic modeling. We see a prime application of this work as a means to maintain up-to-date model bathymetry of a coastal area in anticipation of a storm event, for input to coastal flood inundation models. It will also allow improved predictions of future bathymetry for coastal management purposes, including flood risk management, due to improved model state and better model parameters.

Acknowledgements

This work is being funded under the NERC (UK Natural Environment Research Council) program FREE (Flood Risk from Extreme Events). PJS receives additional funding from the EA (Environment Agency of England and Wales) under the CASE (Co-operative Awards in Science and Engineering) scheme. We would like to thank Alan Cooper at HR Wallingford and Nigel Cross at Lancaster City Council for visits, discussions, and access to additional data.

References

Long, W., Kirby, J.T., Shao, Z. (2008), A numerical scheme for morphological bed level calculations, *Coastal Engineering*, 55(2), 167, doi:10.1016/j.coastaleng.2007.09.009.

Mason, D.C., Amin, M., Davenport, I.J., Flather, R.A., Robinson, G.J., Smith, J.A. (1999). Measurement of recent intertidal sediment transport in Morecambe Bay using the waterline method, *Estuarine, Coastal and Shelf Science*, 49(3), 427–456.

Nichols, N.K. (2003), *Data assimilation: aims and basic concepts*, In: Proceedings of the NATO Advanced Study Institute on Data Assimilation for the Earth System, Maratea, Italy, June 2002.

Scott, T.R., Mason, D.M. (2007), Data assimilation for a coastal area morphodynamic model: Morecambe Bay, *Coastal Engineering*, 54(2), 91–109, doi:10.1016/j.coastaleng.2006.08.008.

Smith, P.J., Dance, S.L., Baines, M.J., Nichols, N.K., Scott, T.R. (2008), Morphodynamic modeling and data assimilation. (This volume.)

Soulsby, R. (1997), *Dynamics of Marine Sands*, Thomas Telford, London, 249pp.

Seasonal and spatial variation in cohesive sediment erodibility in the York River estuary: physical deposition versus biological reworking

PATRICK J. DICKHUDT[1], CARL T. FRIEDRICHS[1], LINDA C. SCHAFFNER[1],
LAWRENCE P. SANFORD[2], ROBERT J. DIAZ[1]

1. Virginia Institute of Marine Science, College of William and Mary,
Gloucester Point VA 23062-1346, USA
email: dickhudt@vims.edu, cfried@vims.edu, linda@vims.edu, diaz@vims.edu

2. University of Maryland Center for Environmental Science, Horn Point Laboratory,
P.O. Box 775, Cambridge MD 21613-0775, USA
email: lsanford@hpl.umces.edu

Keywords: erosion, mud, sediment transport, benthic biology

ABSTRACT

Cohesive sediments in marine and coastal environments are responsible for degrading water quality, influencing the cycling and availability of particle bound contaminants, and infilling navigable waterways. In spite of their significance to coastal environments, there are still major gaps in our understanding of many of the fundamental processes governing cohesive sediment transport and deposition. In particular, seabed erodibility, which facilitates sediment exchange between the bed and water column, is under-resolved in field studies and is often treated as a tuning parameter in numerical models. The goal of this work is to evaluate variation in seabed erodibility over several seasons in a cohesive estuarine environment and gain insight into the dominant physical and biological processes influencing these variations.

Introduction and methods

This study was conducted on the York River estuary, a sub-estuary of the Chesapeake Bay, USA (Figure 1). The York River is tidally energetic with tidal currents reaching magnitudes of ~1 m s^{-1} at the surface during spring tide. A persistent estuarine turbidity maximum (ETM) has been reported just upstream of West Point in the Pamunkey and Mattaponi Rivers, the York's main tributaries. Additionally, an ephemeral secondary turbidity maximum (STM) has been reported in the middle estuary near Clay Bank, ~25 km from the York River mouth (Lin and Kuo, 2001). Schaffner et al. (2001) reported a strong estuarine gradient in ecological diversity from the ETM region of the York into the main stem of the Chesapeake Bay. Both the ETM and STM regions were characterized by high suspended sediment concentrations resulting in unfavorable conditions for benthic biota. In contrast, the main stem of the Chesapeake Bay had lower suspended sediment concentrations and a more diverse benthic community.

Sediment erodibility was measured at three sites on the York River estuary, monthly to bimonthly over a 19-month period. Two sites were established in the more physically dominated middle estuary near Clay Bank, and one site was established in the more biologically influenced lower estuary near Gloucester Point. Each time a site was visited, cores were collected for erodibility measurement, X-radiography, and analysis of grain size, water content, and organic components. Within a few hours of core collection, seabed erodibility over the range of 0.01 to 0.6 Pa was measured with a dual core Gust erosion microcosm.

Results and discussion

The two sites located in the Clay Bank region of the estuary (CS and CC) exhibited a pronounced seasonal cycle in seabed erodibility (Figure 2). Both CS and CC had consistent and relatively low erodibility in the summer and fall of 2006 and 2007 and elevated erodibility in the late winter and spring of 2007. CS and CC also exhibited what appeared to be transitional periods of moderate erodibility prior to and after periods of highest erodibility. In contrast, erodibility at the Gloucester Point (GP) site (Figure 2) was generally low and did not exhibit the pronounced seasonal pattern found at the two Clay Bank sites. Interestingly, the range in eroded mass and mean eroded mass found at GP year-round (except for May 2007) was quite similar to that

measured at the Clay Bank sites in the summer and fall of 2006 and 2007. Weak to nonexistent correlations between bed erodibility, solids volume fraction, and components of organic matter were not sufficient to explain the observed seasonal pattern in erodibility at Clay Bank.

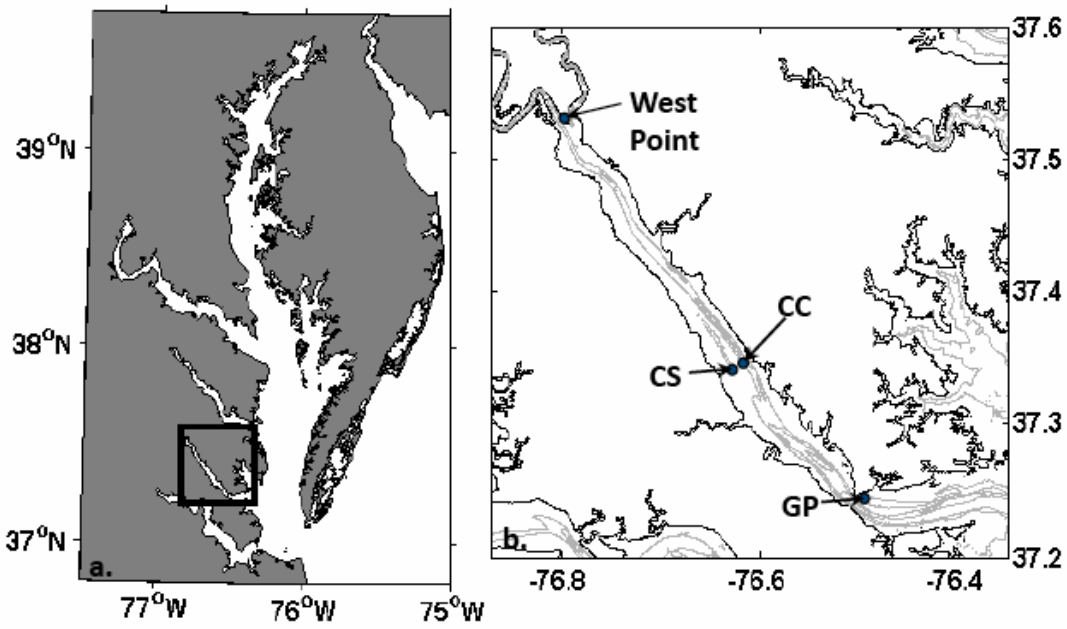

Figure 1. (a) Map of Chesapeake Bay, USA. Black box indicates region included in Figure 1b. (b) Map of York River estuary including sampling station locations. GP = Gloucester Point station, CC = Clay Bank channel station, CS = Clay Bank shoal station.

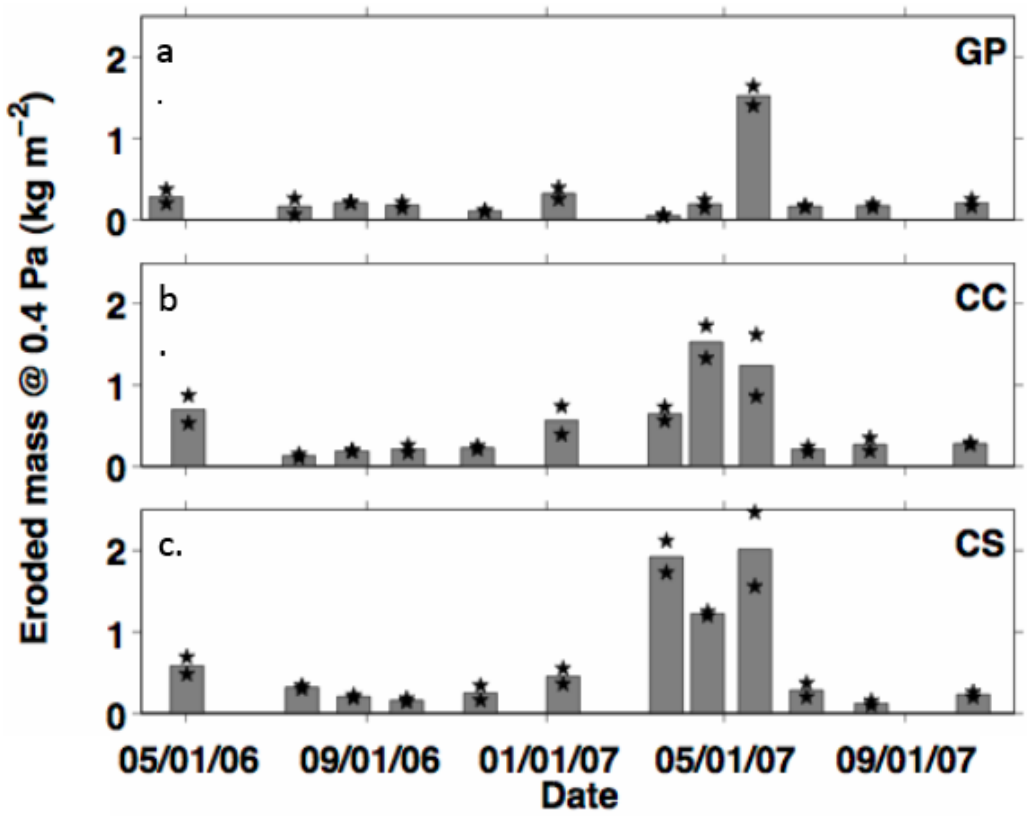

Figure 2. Time series of eroded mass at 0.4 Pa at (a) Gloucester Point (GP) site, (b) Clay Bank channel (CC) site, (c) Clay Bank shoal (CS) site. Stars are values for each of the two individual cores eroded; bars indicate the mean value.

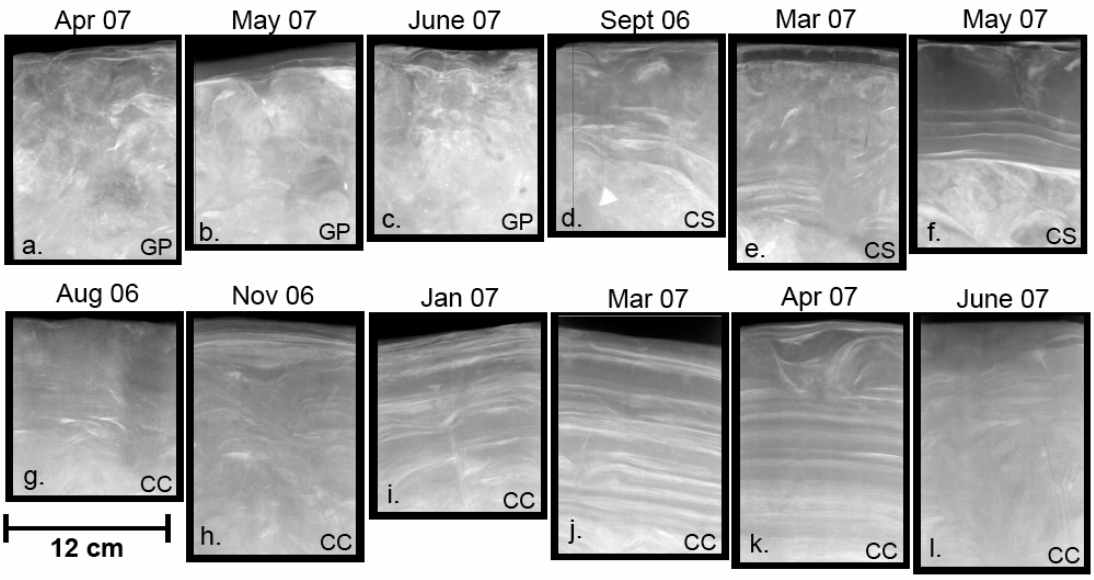

Figure 3. X-radiographs images from the York River. Month and year of sample collection is indicated above each X-radiograph. GP = Gloucester Point, CC = Clay Bank channel, CS = Clay Bank shoal.

X-radiographs from the GP site (Figure 3a–c) revealed little temporal variability in the structure of the seabed. Similar to the GP site, X-radiographs from the CS site often appear mixed with few laminations (Figure 3d). However, a more uniform surface layer, occasionally containing thin laminations and ranging in thickness from 1 to 15 cm, was occasionally observed (Figure 3e–f). This layer was most distinct in March to May of 2007. Digital X-radiographs from the CC site revealed the most dramatic seasonal variability in bed structure. From May to September of 2006 the bed appeared mottled (Figure 3g). In November, a surface layer, 2 cm thick and containing many fine laminations appeared (Figure 3h). Similar laminations were then observed down to 10 cm in January of 2007 (Figure 3i) and down to 20+ cm in March and April. In May 2007 only traces of laminations remained, and by June cores from the CC site appeared mottled once again (Figure 3l).

The presence at Clay Bank of (i) thick sequences of laminated sediments coincident with the period of highest erodibility and (ii) more biologically reworked sediment during the rest of the year suggests that periodic rapid deposition introduced new sediment that was seasonally easy to erode. The presence of laminated bedding in the X-radiographs likely highlighted times when physical processes dominated bioturbation due to rapid deposition overwhelming the ability of benthic biota to mix the seabed. In contrast, sediments appearing mottled were indicative of the times with more active bioturbation and lower rates of deposition. The finding that seasonal deposition influenced erodibility in the Clay Bank region is consistent with previous results indicating the occasional presence of a secondary turbidity maximum.

Comparison of the biologically reworked, but still ‘low’ erodibility condition found at all three York River sites to other published Chesapeake Bay erodibility data revealed a remarkably consistent eroded mass versus critical shear stress profile. In the absence of rapid recent deposition (i.e., outside of turbidity maxima zones), it appears that muddy areas of moderate depth exhibit a notably consistent level of bed erodibility in both space and time. These common erodibilities suggest an equilibrium critical stress profile may exist which may be broadly representative of other similar estuarine environments. At relatively low stresses and in the absence of rapid deposition, we further speculate that burrowing and/or sediment pelletization may play a role in maintaining high equilibrium bulk water content without reducing the strength of the surface of the seabed. Thus the presence of biologically-induced heterogeneity may confound the otherwise expected relationship between muddy seabed water content and erodibility.

Figure 4 presents a conceptual model of processes in the York River estuary influencing bed erodibility. Following periods of high river discharge, a secondary turbidity maximum (STM) forms near Clay Bank, resulting in high suspended sediment concentrations dominated by fines and flocs, rapid deposition of an ephemeral layer tens of centimeters thick, a physically dominated seabed, and high bed erodibility. The lower estuary, including the GP site, lies outside of the region typically occupied by the STM. The result at Gloucester Point is lower suspended sediment concentrations, highly pelletized surficial sediment, a more actively burrowed seabed, and low erodibility. After an extended period of low river flow, stratification

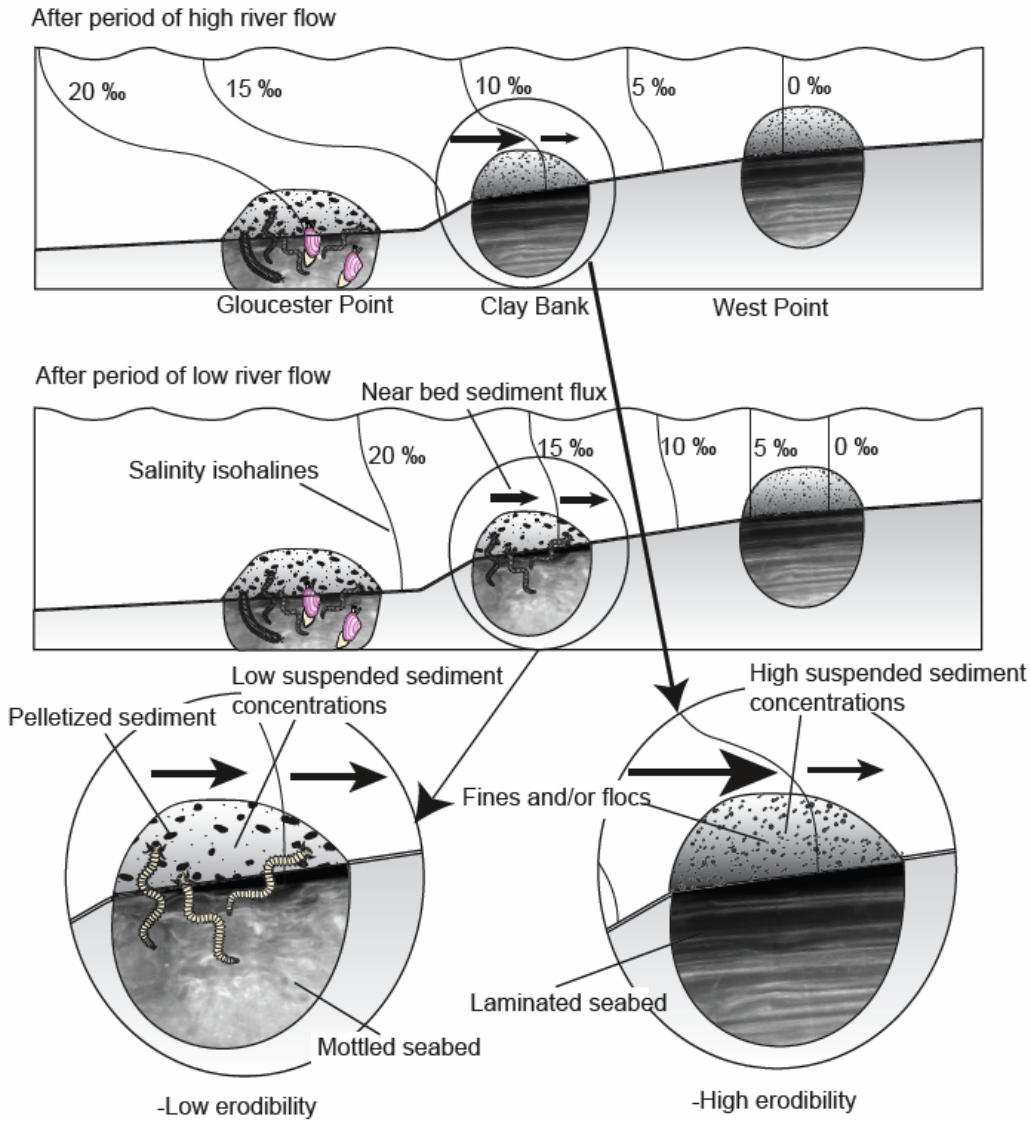

Figure 4. Conceptual diagram for sediment transport and resulting seabed structure in the York River estuary.

throughout the estuary breaks down, and the STM either moves up-estuary or dissipates, resulting in a period of divergent sediment transport and/or sediment bypassing. During this period, the conditions near Clay Bank more closely resemble Gloucester Point, with lower suspended sediment concentrations, increasingly pelletized sediment, more intense bioturbation, and lower erodibility.

Acknowledgements

This work was part of the Multidisciplinary Benthic Exchange Dynamics (MUDBED) project supported by funding from the National Science Foundation (Grant #OCE-0536572). Field and laboratory assistance was provided by Grace Cartwright, Alice Brylawski, Payal Dharia, and Laura Palomo.

References

Lin, J., Kuo, A.Y. (2001), Secondary turbidity maximum in a partially mixed microtidal estuary. *Estuaries*, 24, 707–720.

Schaffner, L.C., Hinchey, E.K., Dellapenna, T.M., Friedrichs, C.T., Thompson Neubauer, M., Smith, M.E., Kuehl, S.A. (2001), *Physical energy regimes, sea-bed dynamics and organism-sediment interactions along an estuarine gradient*. In: Aller, J.Y., Woodin, S.A., Aller, R.C. (Eds.) Organism-Sediment Interactions, University of South Carolina Press, pp159–179.

Organisms influence fine sediment dynamics on basin scale

MINDERT DE VRIES[1, 2], BAS W. BORSJE[2, 1]

1. Deltares, Rotterdamseweg 185, P.O. Box 177, 2600 MH Delft, Netherlands
email: mindert.devries@deltares.nl

2. Water Engineering and Management, University of Twente,
P.O. Box 217, 7500 AE Enschede, Netherlands
email: b.w.borsje@utwente.nl

Keywords: ecosystem engineering, sediment budget, turbidity; Wadden Sea

ABSTRACT

The amount of fine sediment in the water phase and in the bed is an important factor influencing the functioning of the ecosystem. Therefore, man-made and natural changes in the amount and distribution of fine sediment will affect the functioning of the ecosystem. Many bottom dwelling organisms engineer the temporal and spatial distribution of fine sediment in the bed by actively changing settling and erosion processes. In this way organisms influence local habitat quality to their own advantage. Impact on settling and erosion processes will through changes in the bed force changes in the fine sediment availability in the water column. This study elaborates the effect of such local ecosystem-engineers on sediment budget and suspended sediment concentrations at the scale of whole tidal basins. In the Wadden Sea yearly average settling and erosion fluxes are roughly known on the basis of long term monitoring of suspended sediment concentrations. It is shown that the effect of ecosystem engineers, occurring predominantly on shallow areas (less then 3 m water depth), causes erosion fluxes and suspended sediment concentrations to change significantly due to the seasonality of biomass variations. The effect could explain the seasonal variation in suspended sediment concentrations measured in the Wadden Sea. Absolute biomediated fluxes are comparable to exchange of fine sediment between North Sea and Wadden Sea. Biomediated fluxes are an order of magnitude larger than the multi-year averaged net import flux of fine sediment into the Wadden Sea. The study results are in agreement with field data and it is shown that the effect of ecosystem engineers on erosion fluxes and on suspended sediment concentrations is quite large and will result in lower turbidity in the summer and higher turbidity in the winter on basin scale.

Introduction

Research on estuary scale is relevant for society because emergent ecological processes -such as ecosystem self design and human induced ecosystem engineering- act on this scale (Odum, 1996), and therefore, by definition, both must be interacting dynamically. Also, de Jonge (2000) argued that, for the Wadden Sea ecosystem, relevant temporal and spatial scales for management are both annual and basin wide, emphasizing the need for research on that scale.

In tidal basins, fine sediment availability (defined as mixture of cohesive and non-cohesive minerals, smaller then 64 μm diameter) is associated with the occurrence and the distribution of many species living on and in the bed. The distribution of fine sediment suspended in the water phase and deposited on the estuary bed is therefore an important factor governing the functioning of the estuarine ecosystem. It is clear from many studies that bottom dwelling ecosystem-engineering species can change sediment properties in their habitats, on the sub-mudflat scale. The objective of this study is to clarify the influences of bottom dwelling species on the basin scale fine sediment budget.

Study area

This study is focused on the Western part of the Dutch Wadden Sea, located in the northwest of the Netherlands (Figure 1). The study area, the Dutch Western Wadden Sea (WWS) is bounded by the Afsluitdijk, sandy barrier islands and the watershed between Schiermonnikoog island and the mainland (Figure 1). The area of the WWS covers about 2178 km^2 which is made up of 1050 km^2 intertidal, 502 km^2

subtidal (defined here to lie between 1.5 m and 3 m average water depth) and 626 km^2 gullies (more than 3 m water depth). The area is characterized by a diurnal tide, ranging from 1 to 2 m in amplitude.

The bed sediment consists of sands with a median diameter between 170–190 microns, with an average concentration of 1% of mud in the top 10 cm of the drying areas. About 270 km^2 of intertidal area is considered muddy with a mud content averaging 5.8%. Due to the lack of a large local river, mud in the Wadden Sea originates mainly from sources in the North Sea. The physical processes governing the import of mud into the Wadden Sea have been studied extensively. The work of Postma (1961, 1981) and later Dronkers (1984) established a firm base to understand the driving forces behind the transport of fine sediment. Borsje et al. (2008) elaborated the spatial distribution of (de)stabilizing ecosystem engineers in the Wadden Sea, based on biomass and bathymetry, resulting in a spatial zoning presented in Figure 1.

Quantification of basin scale fine sediment budget

Postma (1981) quantified fine sediment transport from North Sea to the Wadden Sea. If we apply his approach to the study area, it can be estimated that the quantity of North Sea water entering the WWS with each flood tide through the various inlets is about 2.2 km^3. With a yearly average concentration of about 10 mg l^{-1} of fine-grained suspended matter, this gives an input of about 21,000 tonnes per tide or 16,106 tonnes each year. The permanent deposition is estimated at 3–5% of the input by various authors (Postma, 1961; Eisma, 1979). This means that each ebb tide must on average leave about 1000 tonnes behind. In addition to loading from the North Sea, some mud arrives in the WWS from rivers through the Afsluitdijk and the Lauwersmeer. The total riverine input is less than 4% of the total input. Gross fluxes within the Wadden Sea basins, especially the exchange between the bed and the water phase, are almost two orders of magnitude higher, due to shallow depths and sensitivity to wave impact. Almost all of this material has to settle each tide within the basin to maintain the observed net balance. If we assume with Postma (1981) that 85% (the remainder has too low settling speeds) of the material can settle in one slack tide, this gives 182,000 tonnes of settled sediment per tide on the intertidal and subtidal areas of the WWS combined. This calculation is based on an average depth of three meters and the multi-year average of suspended sediment concentration data from many stations inside the Wadden Sea, including Zoutkamperlaag and Dantziggat (stations are indicated in Figure 1; see Figure 2 (left panel) for field data of these two stations from the long term monitoring program of Rijkswaterstaat, Waterbase (2008)). Both Postma (1981) and Dronkers (1984) considered biological influences on settling and erosion to be possible important factors for the residual sediment transport between the North Sea and the Wadden Sea. Black et al. (2002) stated that there is no sediment without organisms and cites Paterson (1997), that the biomass and activity of sediment-inhabiting organisms, ranging from bacteria to worms and shrimps, act as important regulatory controls on natural sediment stability, according to many earlier authors. Therefore field data presented in Figure 2 (left panel) must include the effects of ecosystem engineers.

Quantification of ecosystem engineered effects on fine sediment budget

Main **stabilizing** species are benthic primary producers such as diatoms and cyano-bacteria (MPB) that rapidly colonize freshly deposited layers and stick them together, sometimes resulting in layered tidal deposits (Grant and Gust, 1987; Austen, 1999; de Brouwer, 2000; Paterson et al., 2000; de Deckere et al., 2001). Bed destabilization – and therefore increased capacity for erosion – is mainly caused by key surface deposit feeding species such as the surface grazing mud snail *Hydrobia ulvae*, the mudshrimp *Corophium volutator* and Baltic tellin *Macoma balthica*. Although many other species are present in the Wadden Sea, quantitative and seasonal effects of MPB and surface deposit feeding (SDF) macrobenthic ecosystem engineers *Macoma balthica* and *Hydrobia ulvae* are well documented (Widdows et al. 2000a, 2000b; Andersen et al., 2004). Borsje et al. (2008) have analyzed the effect of seasonal biomass variation of (de)stabilizing ecosystem engineers on bed strength and erosion rate. On the basis of the quantifications presented by Borsje et al. (2008) in combination with known gross sediment fluxes presented above, an attempt was made to quantify the effect of ecosystem engineers on whole basin fluxes of fine sediment. Table 1 shows the data used for the analysis.

Results: Ecosystem engineered influence on sediment budget

The influence of ecosystem engineers on erosion in the Wadden Sea is quantified on the basis of the known average erosion flux. An estimate of (de)stabilizing coefficients (Table 1) was derived from Borsje et al.

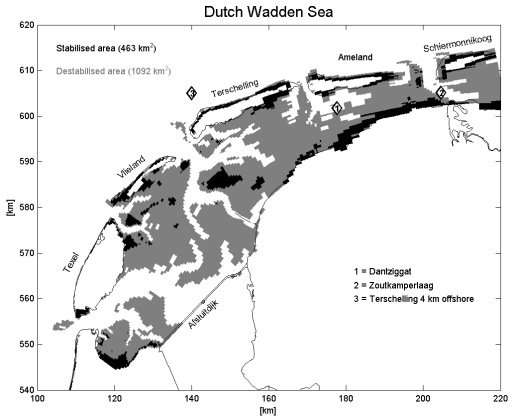

Table 1 Overview of input parameters for quantitative analysis of sediment budget

Parameter	Value
Area of WS (km²)	2178
Average depth of WS (m)	3
Volume of WS (km³)	6.5
Sandy area of WS < -3m (km²)	1550
Mud content of sandy area <-3m (fraction) [2]	0.01
Stabilized area in WS with mud (km²) [1]	463
Mud content of MPB patches in stabilized area (fraction) [2]	0.1
Patchiness factor MPB [1]	0.25
Average depth stabilized area (m)	1
Biomass dependent erosion coefficient MPB (min<>max) [1]	0.37<>0.99
Biomass dependent erosion coefficient SDF (min<>max) [1]	2.8<>3.2
Average settling flux WS (ton/tide) [3]	183 000
Average erosion flux WS (ton/tide) [3]	182 000
Average burial flux (ton/tide) [3]	1000

[1] Values derived from Borsje et al. (2008)
[2] Sedimentatlas (1998)
[3] Postma (1981)

Figure 1. Study area Western Wadden Sea with zones of stabilized and destabilized bed.

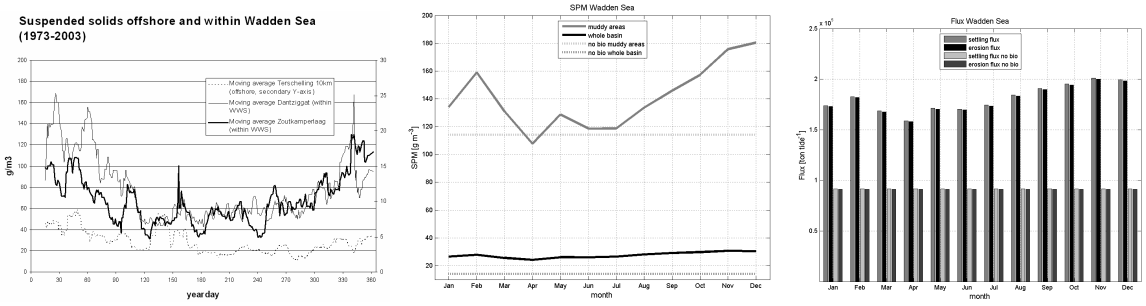

Figure 2. Suspended sediment concentrations measured in Western Wadden Sea (left panel), SPM calculated from biologically influenced erosion flux (middle). Settling and erosion fluxes influenced by biological activity (right panel).

(2008) and is used to influence the average erosion flux. Destabilizing SDF have a significant impact on increase of the erosion flux in the sandy areas. The stabilizing effect of MPB is reducing the erosion flux on the MPB patches in the muddy intertidal areas. Figure 2 gives an overview of the resulting suspended matter concentration (SPM) and settling and erosion fluxes, exclusively based on biomass trends of MPB and SDF throughout the year, assuming complete and instantaneous mixing in the water column. When compared to SPM measured in stations within the Wadden Sea (left panel of Figure 2) the seasonal patterns are strikingly similar. It becomes clear that ecosystem engineers (stabilizers and destabilizers combined) cause a significant 'bio-mediation' of erosion flux and therefore of SPM. The fluxes must be doubled when compared to a situation without biological activity, in order to maintain the observed average erosion flux. The variation of SPM is comparable to what is measured in the field. Driven by biomass cycles throughout the year, maximum influence of stabilizing MPB is seen in spring and summer, leading to lower SPM, while maximum influence of destabilizing SDF is seen in autumn and winter, gradually compensating stabilizing activity, resulting in increasing SPM. MPB reduces erosion flux with a magnitude comparable to the average import of fine sediment of North Sea to Wadden Sea. SDF increases erosion flux at least five times over the level of average import from North Sea.

Conclusions

This study demonstrates the influence of biota on the fine sediment transport on estuary scale. From this study a picture of ecosystem-engineers has arisen, that indicates that on basin scale, dynamic bio-physical interactions indeed emerge, influencing sediment transport. Sediment transport fluxes inside the Wadden Sea are affected following seasonal trends in biomass. The quantity of these effects is larger than the fine sediment exchange between Wadden Sea and North Sea and at least an order of magnitude larger than estimated net import flux. The sediment destabilizing processes are stronger than the stabilizing processes and are occurring on larger areas, caused by the influence of basin shape on zoning of habitats. Strong effect on turbidity is observed, indicating a link between basin shape, activity of ecosystem engineers and water quality. Ecosystem engineering species might influence the balance between import and export of fine

material between Wadden Sea and North Sea. The results emphasize the need of incorporating biological activity in the physical models to help formulate recommendations for the management and conservation of high biomass mesotidal tidal basins.

Acknowledgements

This research is supported by the Dutch Technology Foundation STW, applied science division of NOW and the Technology Program of the Dutch Ministry of Economic Affairs.

References

Andersen, T.J., Lund-Hansen, L.C., Pejrup, M., Jensen, K.T., Mouritsen, K.N. (2004), Biologically induced differences in erodibility and aggregation of subtidal and intertidal sediments: a possible cause for seasonal changes in sediment deposition, *Journal of Marine Systems*, 55, 123–138.

Austen, I., Andersen, T.J., Edelvang, K. (1999), The influence of benthic diatoms and invertebrates on the erodibility of an intertidal mudflat, the Danish Wadden Sea, *Estuarine, Coastal and Shelf Science*, 49, 99–111.

Borsje, B.W., de Vries, M.B., Hulscher, S.M.J.H., de Boer, G.J. (2008), Modelling large scale cohesive sediment transport by including small scale biological influences, *Estuarine, Coastal and Shelf Science*, 78, 468–480.

de Brouwer, J.F.C., Bjelic, S., de Deckere, E.M.G.T., Stal, L.J. (2000), Interplay between biology and sedimentology in a mudflat (Biezelingse Ham, Westerschelde, The Netherlands), *Continental Shelf Research*, 20, 1159–1177.

de Deckere, E.M.G.T., Tolhurst, T.J., de Brouwer, J.M.C. (2001), Destabilization of cohesive intertidal sediments by infauna, *Estuarine, Coastal and Shelf Science*, 53, 665–669.

Dronkers, J. (1984), Import of fine marine sediment in tidal basins, *Netherlands Journal of Sea Research*, 10, 83–105.

Eisma, D. (1981), *Supply and deposition of suspended matter in the North Sea*. In: International Association of Sedimentologists, International Meeting: Holocene Sedimentation in the North Sea Basin. Special publication 5, 415–428.

Grant J., Gust, G. (1987), Prediction of coastal sediment stability from photopigment purple sulphur bacteria, *Nature*, 330, 244–246.

de Jonge, V.N. (2000), Importance of temporal and spatial scales in applying biological and physical process knowledge in coastal management, an example for the Ems estuary, *Continental Shelf Research*, 20, 1655–1686.

Odum, H.T. (1996), Scales of ecological engineering, *Ecological Engineering*, 6, 7–19.

Paterson, D.M. (1997), *Biological mediation of sediment erodibility: ecology and physical dynamics*. In: Cohesive sediments, Burt, N., Parker, R., Watts, J. (Eds.), Wiley and Sons Ltd, pp215–229.

Paterson, D.M., Black, K.S. (1999), *Water flow, sediment dynamics and benthic biology*. In: Advances in Ecological Research 29. Academic Press. ISBN 0120139294. pp155–193.

Paterson, D.M., Tolhurst, T.J., Kelly, J.A., Honeywill, C., de Deckere, E.M.G.T., Huet, V., Shayler, S.A., Black, K.S., de Brouwer , J., Davidson, I. (2000), Variations in sediment properties, Skeffling mudflat, Humber Estuary, UK, *Continental Shelf Research*, 20, 1373–1396.

Postma, H. (1961), Transport and accumulation of suspended matter in the Dutch Wadden Sea, *Netherlands Journal of Sea Research*, 1, 148–190.

Postma, H. (1981), Exchange of materials between the North Sea and the Wadden, *Marine Geology*, 40, 199–213.

Sedimentatlas 1998, CDROM Rijkswaterstaat Waterdienst. Available from www.waddenzee.nl.

Waterbase 2008. Rijkswaterstaat Waterdienst. Available from www.waterbase.nl.

Widdows, J., Brinsley, M.D., Salkeld, P.N., Lucas, C.H. (2000a), Influence of biota on spatial and temporal variation in sediment erodability and material flux on a tidal flat (Westerschelde, The Netherlands), *Marine Ecology Progress Series*, 194, 23–37.

Widdows, J., Brown, S., Brinsley, M.D., Salkeld, P.N., Elliott, M. (2000b), Temporal changes in intertidal sediment erodability: influence of biological and climatic factors, *Continental Shelf Research*, 20, 1275–1289.

Field observation of fine sediment transport processes and oxygen fluxes in estuarine bottom boundary layer

YASUYUKI NAKAGAWA, TOMOHIRO KUWAE

Coastal and Estuarine Environment Research Division,
Port and Airport Research Institute, 3-1-1 Nagase, Yokosuka 247-0006, Japan
email: y_nakagawa@ipc.pari.go.jp, kuwae@ipc.pari.go.jp

Keywords: tidal currents, fine sediment resuspension, bottom boundary layers, oxygen flux, eddy correlation method

ABSTRACT

Field measurements were carried out to elucidate fine sediment transport processes near the bed in Ariake Bay, Japan. Several acoustic velocimeters were deployed for the monitoring, such as an upward-looking acoustic Doppler current profiler (ADCP), a downward-looking pulse coherent acoustic Doppler profiler (PC-ADP) and an acoustic Doppler velocimeter (ADV) for the bottom boundary layer study. Comparing OBS data, converted to suspended sediment concentration near the bed, with current field data, external forcing conditions for the bottom sediment resuspension event were evaluated through estimates of shear stress from measured velocity data. In addition to the measurement of physical parameters, as a preliminary study of how resuspension events affect water quality changes, the eddy correlation method was applied in the field for direct measurement of oxygen fluxes across the bed; estimates demonstrate reasonable values.

Introduction

Measurements of current properties in the bottom boundary layer are crucial for understanding sediment transport processes. Several acoustic velocimeters have been developed and applied in field measurement for bottom boundary studies (e.g., Sherwood et al., 2006). This study focuses on fine sediment transport processes in a coastal and estuarine area, and field monitoring was carried out in Ariake Bay, Japan with high resolution current measurements near the bed using several acoustic velocimeters. In addition to the physical aspects of the bottom boundary layer (including sediment resuspension), we are also interested in how the resuspension event affects water quality changes. Since oxygen depression is prominent, especially during the summer season in the study area, the eddy correlation method was applied in the field for in situ direct measurement of oxygen flux across the sea bed using a microelectrode.

Observation

Field data presented in the study were collected in February 2008 with instruments mounted on bottom pods at a monitoring site in inner Ariake Bay (Figure 1). The bay is a macrotidal estuarine system and the tidal range during spring tide varies from 4 m at the mouth and increases up to more than 6 m towards the inner bay. Sediments near shore in the bay are composed of mud, and resuspension events were observed to be caused not only by wind waves but also by tidal currents (e.g., Nakagawa, 2007). The mean depth of the deployment site is 6 m and the bed is composed of silt (66%) and clay (33%). Instruments were deployed for the current and turbidity measurement from 14 to 28 February 2008.

For the current measurement, the data were obtained with several acoustic velocimeters. A pulse coherent acoustic-Doppler profiler (Sontek, PC-ADP) was mounted at 1.2 m above the bed and measured the bottom boundary current profiles with the space resolution of 10 cm bins. The sample rate was 10 minutes with 1 Hz every hour. ADVs (Nortek, Vector) were mounted for the measurement of turbulence near the bed and sampled three components of velocity at 20 cm above the bottom for 4 minutes with 16 Hz every hour. Five optical backscatter sensors (OBS) were mounted to provide suspended sediment concentration (SSC) profile at several elevations. The collected OBS data were converted to SSC in $mg\,l^{-1}$ by calibrating against sediment samples from the site.

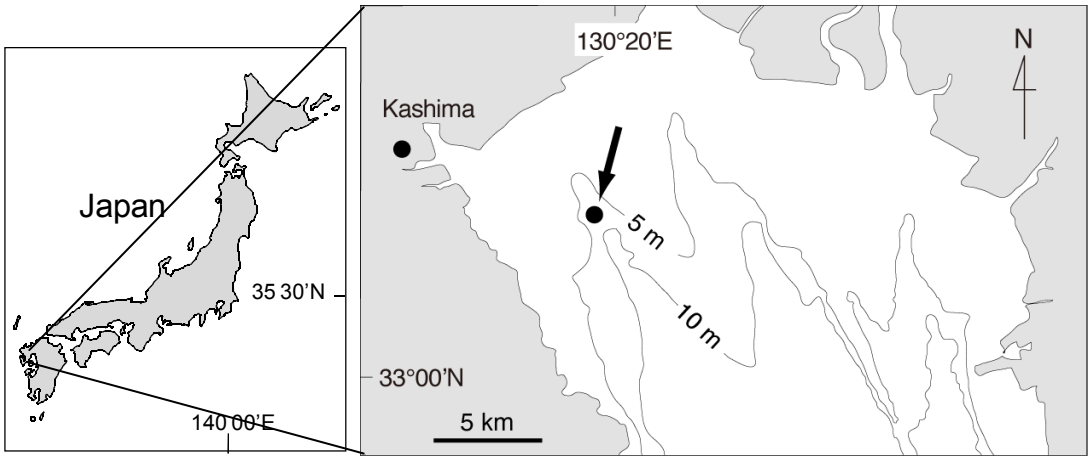

Figure 1. Location of Ariake Bay and study site.

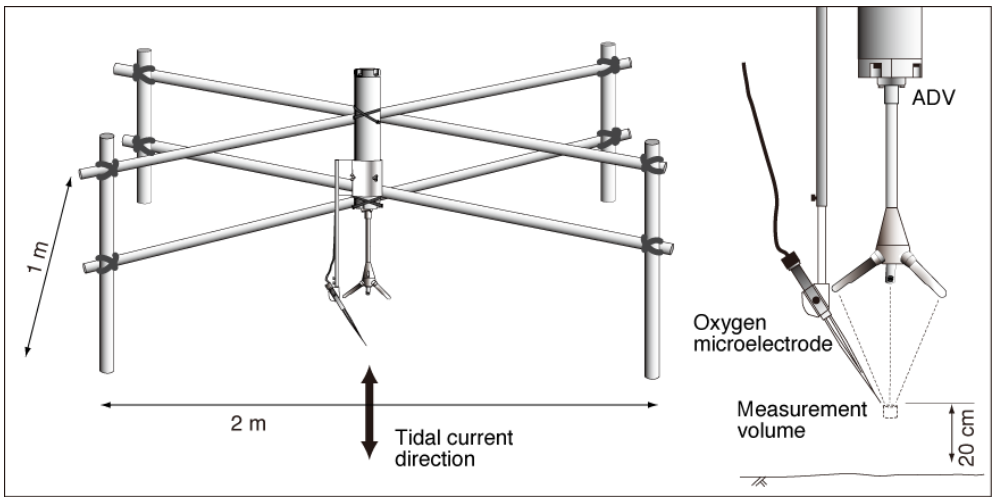

Figure 2. Schematic drawing of oxygen flux measurement system.

In order to estimate oxygen flux at sediment-water interfaces, an oxygen microelectrode sensor (Unisense, OX10) was also applied during the field monitoring campaign. The sampling of oxygen concentration by the sensor was synchronized with measurements of three components of velocity by an ADV and they were mounted on an instrument pod (Figure 2) so that the target point is 20 cm above the bed. Due to the capacity of the data recording system, they were deployed only for 24 hours on 13–14 and 20–21 February sampling continuously at a rate of 16 Hz. For the estimation of oxygen vertical flux, the so called 'eddy correlation' method (e.g., Berg et al., 2007) was applied here.

Results

Measured time series data of tide, current speed and SSC at 20 cm above the bed are shown in Figure 3. During spring tide period, the current speed exceeds around 30 cm s^{-1} and higher SSC events are clearly shown in the data. The higher SSC event at the site is caused mainly by advection of turbid water from the shallower coast and intertidal mud flat area during the low tide of spring tide period with longer tidal excursion. Moreover, local resuspension of the bottom sediment at the site also affect the SSC variation in ebbing and flooding tide phase when currents are strong. Critical force conditions for resuspension of sediments will be analyzed through estimation of bottom shear stress from currents and turbulence measured in the bottom boundary layer.

On the other hand, time series data for the period of oxygen concentration sampling with the microelectrode sensor are demonstrated in Figure 4. Oxygen concentration is highly correlated with SSC variation and they are high during low tide. It is conceivable that these higher concentrations might be caused by the advection of particles originating from algae since the inner area of the site were utilized for cultivation of seaweed by the fishery industry. Estimated oxygen flux with the eddy correlation method is on the bottom of Figure 4

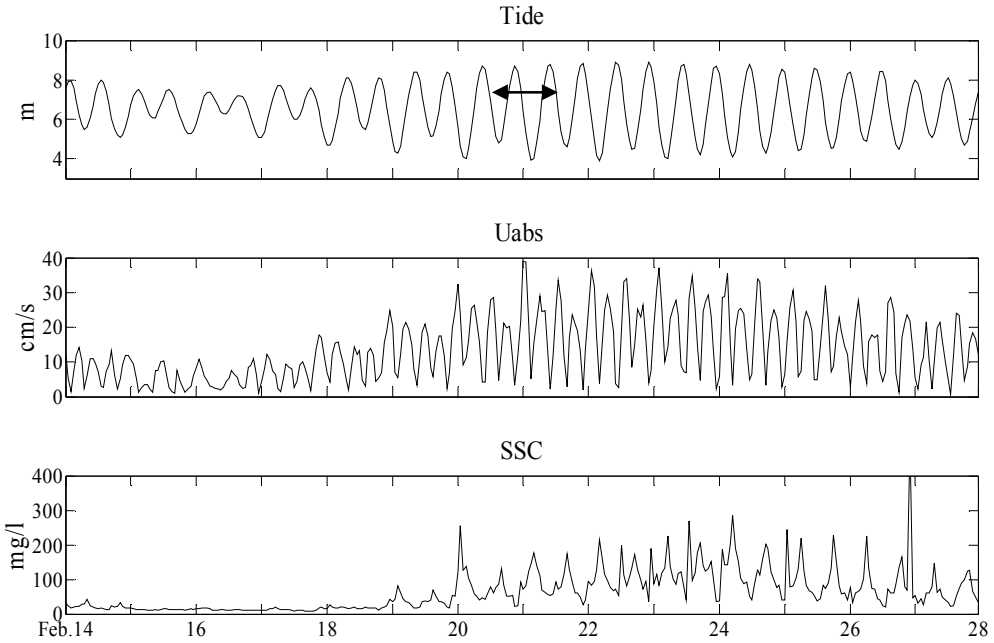

Figure 3. Tide, current speed and SSC at 20 cm above bed. (Deployment period of oxygen flux measurement indicated by arrow.)

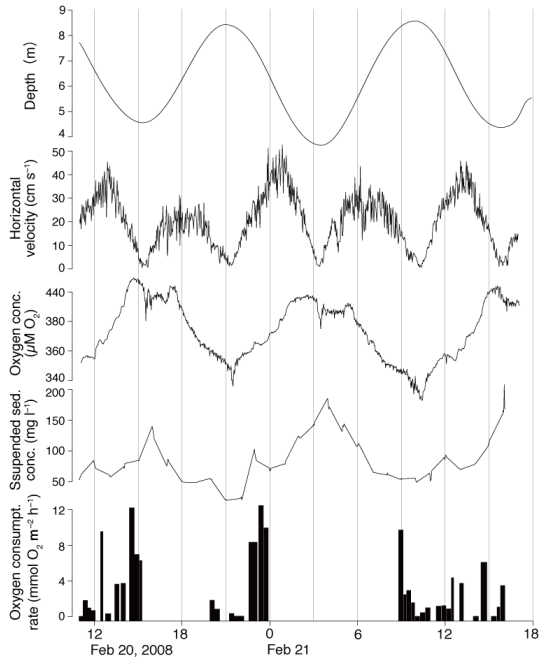

Figure 4. Time series data during deployment of oxygen concentration measurement by electrode.

and the values mean downward flux of oxygen or consumption rate at the bottom surface. Individual estimation of the flux was provided by oxygen concentration and velocity data of 20 minutes length. There is no estimated result in Figure 4 when oxygen data are judged as erroneous with extraordinary high values. The orders of the values are comparative to that of measured on intertidal flat in other Japanese bays (Kuwae et al., 2006). There is a tendency for the consumption rate to become higher under the stronger current condition especially during flooding tide as shown in Figure 5.

Conclusions

Field measurements were carried out for the monitoring of fine sediment transport dynamics with several acoustic velocimeters and optical turbidity sensors in Ariake Bay, Japan. In addition to measurement of

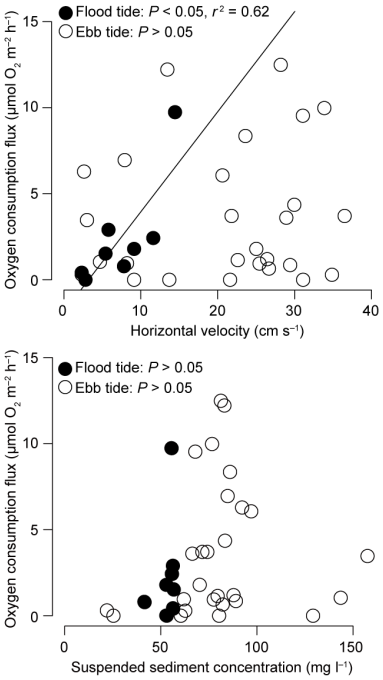

Figure 5. Relationships between estimated oxygen consumption rate (downward flux) and circumstance conditions (upper: current speed, lower: SSC).

physical aspects in the bottom boundary, the scope of this study includes examination of the effect of the resuspension event on water quality changes. As a preliminary study, the eddy correlation method was tested in the field for in situ measurement of oxygen flux across the sea bed and the estimated data shows reasonable values. The method will be applied in the next field monitoring campaign to elucidate prominent oxygen depression in the summer season.

Acknowledgements

The authors thank E. Miyoshi and S. Hosokawa of the Port and Airport Research Institute for their kind help for instrumentation and many field works. This research is supported by the Global Environment Research Fund granted to authors (grant number is RF-074) by the Ministry of the Environment, Japan.

References

Berg, P., Roy, H., Wiberg, P. L. (2007), Eddy correlation flux measurements: The sediment surface area that contributes to the flux, *Limnology and Oceanography*, 52(4), 1672–1684.

Kuwae, T., Kamio, K., Inoue, T., Miyoshi, E., Uchiyama, Y. (2006), Oxygen exchange flux between sediment and water in an intertidal sandflat, measured in situ by the eddy-correlation method, *Marine Ecology Progress Series*, 307, 59–68.

Nakagawa, Y. (2007), *Fine sediment transport in Ariake Bay, Japan*. In: Maa, J.P.-Y., Sanford, L.P., Schoellhamer, D.H. (Eds.), Estuarine and Coastal Sediments Dynamics. Elsevier, pp377–394.

Sherwood, C.R., Lacy, J.R., Voulgaris, G. (2006), Shear velocity estimates on the inner shelf off Grays Harbor, Washington, USA., *Continental Shelf Research*, 26, 1995–2018.

The mass-transfer limited supply of pelagic phytoplankton to the benthos in a shallow estuarine environment

NICOLE L. JONES[1], JANET K. THOMPSON[2], KEVIN R. ARRIGO[3], STEPHEN G. MONISMITH[4]

1. School of Environmental Systems Engineering, University of Western Australia, MO15, 35 Stirling Highway, Crawley 6009, Western Australia, Australia
email: nicole.jones@uwa.edu.au

2. U.S. Geological Survey, 345 Middlefield Road MS-496, Menlo Park CA 94025-3591, USA
email: jthompso@usgs.gov

3. Department of Geophysics, Stanford University, Stanford CA 94305-2215, USA
email: arrigo@stanford.edu

4. Environmental Fluid Mechanics Laboratory, Civil and Environmental Engineering, Stanford University, Stanford CA 94305-4020, USA
email: monismith@stanford.edu

Keywords: phytoplankton, benthic grazing, shallow water, aggregation, fluff layer

ABSTRACT

Benthic grazing can be a primary factor in determining if shallow systems are net phytoplankton exporters or net phytoplankton sinks. Field experiments were undertaken to measure the influence of hydrodynamics on the removal of phytoplankton by benthic grazers in Suisun Slough, North San Francisco Bay. Chlorophyll *a* concentration boundary layers were found to exist at this site. Benthic losses of phytoplankton were estimated via both control volume and vertical flux approaches, in which chlorophyll *a* concentration was measured as a proxy for phytoplankton abundance. The rate of loss of phytoplankton to the bed was observed to be positively correlated to the bed shear stress. Strikingly, rates of loss of phytoplankton to the bed were an order of magnitude larger than estimated by laboratory derived pumping rates for the suspension feeders present. We hypothesize that aggregation of phytoplankton in a near-bed fluff layer may account for the observed large transfer of pelagic carbon to the benthos. There was evidence in our study that the biomass of suspension feeders and surface deposit feeders were supported by this food source.

The work in this extended abstract is contained in a manuscript entitled 'Hydrodynamic control of phytoplankton loss to the benthos in an estuarine environment' submitted for publication in Limnology and Oceanography.

Introduction

Benthic grazing by siphonate bivalves can limit the accumulation of phytoplankton biomass in shallow waters in many systems (e.g., Dame et al., 1980; Newell, 2004; Prins and Escaravage, 2005). Hydrodynamics can directly affect the strength of benthic-pelagic coupling. For example, concentration boundary layers (CBL) form when phytoplankton cells removed by beds of bivalves are not replaced by vertical mixing. When CBLs form, the flux of particles to the incurrent siphons of bivalves is reduced. Therefore, the benthic grazing rate (the rate of removal of particles, such as phytoplankton, from the water [$m^3\ m^{-2}\ s^{-1}$]) is a function of both the pumping rate (the volume of water passing through the siphon per unit time [$m^3\ s^{-1}\ ind^{-1}$]) and the overlying hydrodynamics. Despite great improvements in our knowledge of the effects of benthic grazers on water column seston concentrations, the impact of different hydrodynamic conditions on grazing rates has not been thoroughly quantified. This makes it difficult to assess the system-wide effect of the benthic community on phytoplankton concentrations.

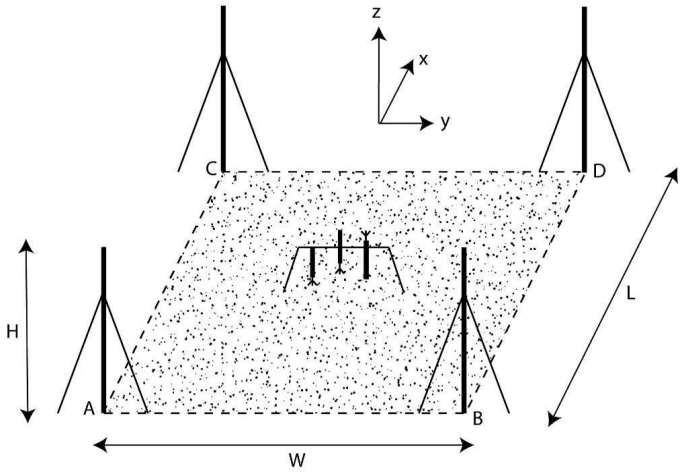

Figure 1. A schematic drawing of the control volume. The four water sampling frames are shown at the corners of the control volume. The instruments shown in the center of the CV are measuring the hydrodynamics. The dominant flow is in the *x*-direction.

The objective of this study was to determine the variability of benthic grazing as a function of the hydrodynamic conditions in shallow water. Specifically, our goals were to: 1) confirm the existence of concentration boundary layers over beds of the clam *Corbicula amurensis* in North San Francisco Bay; 2) determine the relationship between phytoplankton loss due to benthic grazers and the rate of turbulent mixing; and 3) determine the relationship between laboratory-derived pumping rates and in situ grazing rates.

Methods

Chlorophyll a (Chl *a*) concentrations were sampled along each vertical corner of a 10 × 20 m control volume in Suisun Slough, North San Francisco Bay (Figure 1). The water sampling frames collected samples at eight discrete heights (0.1, 0.15, 0.2, 0.25, 0.35, 0.5, 1 and 2.5 m) above the bed. Ten-minute integrated water samples were collected every hour for two 30-hr experiments. The currents were measured at the center of the control volume using an upward looking acoustic Doppler current Profiler (ADCP, RD Instruments) and an array of three acoustic Doppler velocimeters (ADVs, Nortek AS). Vertical density structure at the center of the control volume was measured by an array of thermistors and conductivity sensors (SBE39 and SBE16+, Seabird Electronics). Zooplankton and phytoplankton community composition was sampled periodically. At the conclusion of the experiment, the benthos in the area was systematically sampled.

Benthic losses were estimated via two methods. The control volume method uses an imaginary box (the control volume) that encloses the region of interest (Figure 1). The Flux of Chl *a* was estimated for each face of the control volume and unsteady changes in Chl *a* in the control volume were calculated, these terms were summed and then we assumed losses were due to benthic grazing. The vertical flux method uses the near-bed Chl *a* concentration gradient and the vertical turbulent diffusivity to estimate the benthic grazing rate. Turbulent diffusivity was estimated from the turbulence measurements of the ADVs.

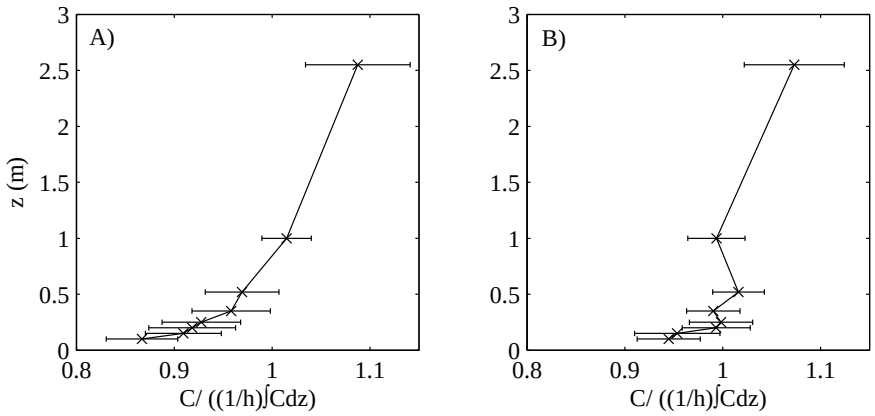

Figure 2. Ensemble-averaged dimensionless profiles for (A) experiment 1 and (B) experiment 2. The non-dimensionalization involves dividing the local value of the concentration by the depth-averaged concentration for that profile.

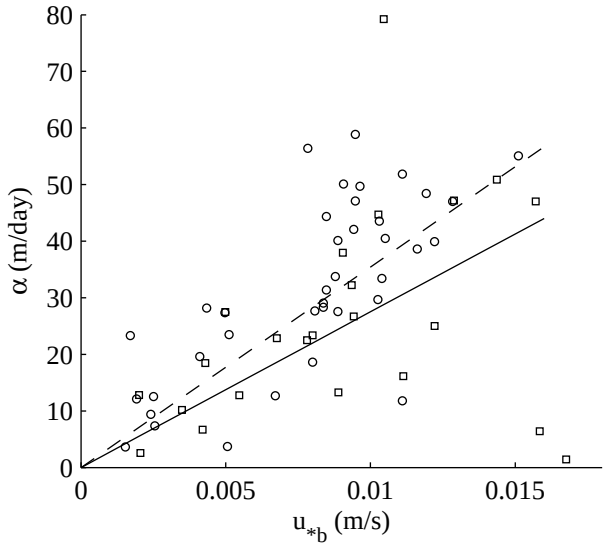

Figure 3. Benthic grazing rate α calculated via the control volume method (squares) and vertical flux method (circles) vs the bed shear velocity u_{*b}. The best fit robust linear regression is shown for each method; control volume method (solid line) and vertical flux method (dashed line).

Results

The phytoplankton biomass was dominated by diatoms during the experiments and the zooplankton community was largely carnivorous. The dominant filter feeders at the Suisun Slough site were the two species of clams (*Corbula amurensis* and *Macoma petalum*), a tube-forming amphipod (*Corophium alienense*), and to a lesser extent, a tube dwelling Sabellid polychaete (*Laonome sp*). The total pumping rate for all active suspension feeders was estimated as 6–7 $m^3\ m^{-2}\ d^{-1}$ using laboratory derived pumping rates.

Vertical profiles of Chl *a* concentration for both experiments exhibited a depletion of Chl *a* adjacent to the bed for a range of different surface Chl *a* concentrations and hydrodynamic conditions. Individual profiles were normalized by the depth-averaged concentration and averaged over the four sampling locations and all sampling times for each experiment to produce non-dimensionalized Chl *a* concentration profiles (Figure 2). The ensemble-averaged normalized profile for experiment 1 indicates that on average there was a considerable depletion of Chl *a* towards the bed. The sample closest to the bed was on average 22% and 12% lower than the near surface concentration for the 1st and 2nd experiments, respectively.

The maximum benthic grazing estimated from the field experiments was approximately 50 $m\ d^{-1}$. The vertical flux analysis indicated that the grazing rate α_{VF} of the benthic organisms was approximately a linear function of the bed shear velocity u_{*b}: $\alpha_{VF} = (3.5 \times 10^{-2} \pm 1.1 \times 10^{-2})\, u_{*b}$. Robust linear least squares regression of the estimated benthic grazing rate via the control volume method α_{CV} versus the bed shear velocity revealed: $\alpha_{CV} = (3.1 \times 10^{-2} \pm 1.2 \times 10^{-2})\, u_{*b}$. Here the uncertainty is at the 95% confidence level and $r^2 = 0.81$ (Figure 3).

Discussion

The benthic grazing rate was positively correlated with the bed shear velocity indicating that the loss of Chl *a* to the bed was mass-transfer limited. However, our third method of estimating benthic grazing rates, using measured abundance and biomass of the benthic community and laboratory derived pumping rates, resulted in estimates an order of magnitude lower (6–7 $m\ d^{-1}$) than the maximum benthic grazing estimates from the field experiments (50 $m\ d^{-1}$). Filtration (and phytoplankton ingestion) rates for benthic organisms are generally smaller than calculated pumping rates due to the formation of CBLs, the refiltration of water (O'Riordan et al., 1995) and the intermittency of pumping (Ortmann and Grieshaber, 2003) so this finding was troubling.

Alternative mechanisms to account for the measured loss of Chl *a* at the bed were considered including: turbulent deposition (e.g., Wood, 1981) and the aggregation of phytoplankton in a near-bed 'fluff' layer (Stolzenbach et al., 1992). We concluded that turbulent deposition of either individual diatoms cells or aggregates containing diatoms contributed minimally to losses of phytoplankton at the bed. Near-bed aggregation of phytoplankton was identified to be a plausible mechanism.

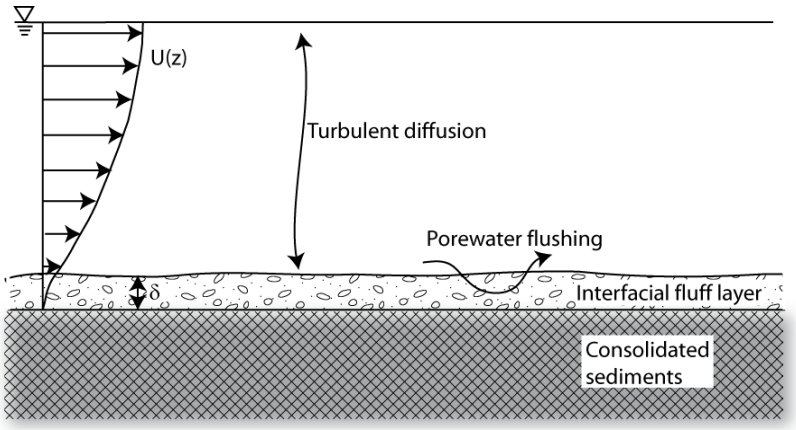

Figure 4. Schematic of aggregation of pelagic phytoplankton in a near-bed fluff layer (adapted from Stolzenbach et al. 1992).

A fluff layer is characterized by loosely aggregated material of high porosity (Figure 4). The fluff layer is hydrodynamically active, and therefore particle transport into this layer is not limited by transport across a laminar sublayer. Particle aggregation would be enhanced in the fluff layer due to both the large number of particles and the large shear stresses, resulting in an increased collision frequency of particles (Jahmlich et al., 2002; Colomer et al., 2005). For this reason, the positive correlation found between the estimated benthic loss rate and the bed shear velocity supports the near-bed aggregation mechanism. Aggregation would further be mediated by the pseudofeces and mucus produced by the benthic community (Meadows et al., 1990). Comparing the carbon produced by the phytoplankton in this system with that consumed by a combination of the surface deposit and suspension feeding members of the benthic community identified the near-bed aggregation mechanism as a plausible explanation for the high flux of phytoplankton to the bed.

Further measurements in the near-bed region are required to investigate the importance of the near-bed aggregation mechanism as a means of accelerating the transfer of pelagic carbon sources to the passive suspension and deposit feeders in the benthic community. Such a transport and near-bed retention mechanism may reduce the delivery time for the pelagic carbon to the deposit feeders in shallow, turbulent systems such as San Francisco Estuary. These near-bed bio-physical processes may be capable of limiting pelagic phytoplankton biomass and primary production in a manner similar to that seen with filter-feeding organisms.

References

Colomer, J., Peters, F., Marrasé, C. (2005), Experimental analysis of coagulation of particles under low shear flow, *Water Research*, 39, 2994–3000.

Dame, R., Zingmark, R., Stevenson, H., Nelson, D. (1980), *Filter feeder coupling between the water column and benthic subsystems*. In: Estuarine perspectives. Kennedy, V.S., Estuarine Research Federation, United States Environmental Protection Agency (Eds.), Academic Press. pp521–526.

Jahmlich, S., Lund-Hansen, L.C., Leipe, T. (2002), Enhanced settling velocities and vertical transport of particulate matter by aggregation in the benthic boundary layer, *Geografisk Tidsskrift – Danish Journal of Geography*, 102, 37 49.

Meadows, P., Tait, J.,. Hussain, S. (1990), Effects of estuarine infauna on sediment stability and particle sedimentation, *Hydrobiologia*, 190, 263–266.

Newell, R.I.E. (2004), Ecosystem influences of natural and cultivated populations of suspension-feeding bivalve molluscs: a review, *Journal of Shellfish Research*, 23, 51–61.

O'Riordan, C.A., Monismith, S.G., Koseff, J.R. 1995. The effect of bivalve excurrent jet dynamics on mass-transfer in a benthic boundary-layer, *Limnology Oceanography*. 40, 330–344.

Ortmann, C., Grieshaber, M.K. (2003), Energy metabolism and valve closure behaviour in the Asian clam Corbicula fluminea, *Journal of Experimental Biology*, 206, 4167–4178.

Prins, T.C.,. Escaravage, V. (2005), Can bivalve suspension-feeders affect pelagic food web structure? In: The Comparative Role of Suspension-Feeders in Ecosystems. Dame, R.F., Olenin, S. (Eds.), NATO Science Series. Springer. pp31–52.

Stolzenbach, K.D., Newman, K.A., Wang, C.S. (1992), Aggregation of fine particles at the sediment-water interface, *Journal of Geophysical Research*, 97, 17889–17898.

Wood, N.B. (1981), A simple method for the calculation of turbulent deposition to smooth and rough surfaces, *Journal of Aerosol Science*, 12, 275–290.

Modeling and observation of acceleration-skewed oscillatory flow over fixed beds

ALAN G. DAVIES[1], DOMINIC A. VAN DER A[2], TOM O'DONOGHUE[2], JAN S. RIBBERINK[3]

1. School of Ocean Sciences, College of Natural Science, Bangor University, Menai Bridge, Anglesey LL59 5AB UK
email: a.g.davies@bangor.ac.uk

2. School of Engineering, University of Aberdeen, Aberdeen AB24 3UE UK
email: d.a.vandera@abdn.ac.uk, t.odonoghue@abdn.ac.uk

3. Water Engineering and Management, University of Twente, P.O. Box 217, 7500 AE Enschede, Netherlands
email: j.s.ribberink@utwente.nl

Keywords: oscillatory boundary layer, turbulence, waves, wave-induced flow

ABSTRACT

Recent interest in the effects on net sediment transport of acceleration skewness beneath steep and breaking waves has highlighted the lack of detailed process measurements available, not least of the hydrodynamics. This has motivated a series of experiments, involving 'sawtooth' waves, to be conducted above fixed rough beds. This paper focuses on comparisons between the new data and a 1DV k-ε turbulence-closure model. The results presented examine (i) the evolution of velocity profiles through the sawtooth wave cycle, (ii) the asymmetry in the turbulence intensities and shear stresses during the cycle and (iii) the residual currents generated in the (implied) offshore direction by turbulence-asymmetry. The general implications for sediment transport are also considered.

Introduction

Practical models of net sand transport by wave action have typically been of quasi-steady type relying on the assumption that the time-varying bed shear stress, which acts as the driver for sediment movement, can be related directly to the time-varying free-stream velocity (e.g., Ribberink, 1998). Moreover, it has been shown previously how velocity skewness, such as found beneath Stokes second-order waves, can give rise to a net 'onshore' transport of sediment (i.e., in the direction of wave advance) (Davies and Li, 1997). However, a variety of recent experimental and modeling studies has highlighted the significant, additional influence of acceleration skewness on net sediment transport rates beneath waves. This effect is important, for example, just before wave breaking, as may be inferred from an extensive analysis of field data by Elfrink et al. (2006).

Laboratory experiments involving 'sawtooth-type' flows above sand beds have produced non-zero net transport rates, with the magnitude of the transport increasing with the degree of acceleration skewness (Watanabe and Sato, 2004). Such results have prompted attempts to incorporate 'acceleration effects' into practical sand transport models (e.g., Nielsen, 2006; Silva et al., 2006; Guard et al., 2007). Research models have also been used to investigate acceleration effects (Hsu and Hanes, 2004; Calantoni and Puleo, 2006; Gonzalez-Rodriguez and Madsen, 2007). However, our understanding of acceleration effects has been limited to date by the lack of detailed process measurements.

The research reported here focuses on oscillatory flows with sawtooth-type velocity time-series. In particular, measurements and modeling have been carried out in flows that exhibit zero velocity skewness, but non-zero acceleration skewness. The latter effect has thereby been isolated though, of course, in the field the two effects would be expected to occur simultaneously. Here full-scale laboratory tunnel experiments are investigated in which sawtooth-type flows, with varying degrees of skewness have been generated over fixed rough beds. The results from the experiments are compared with predictions from an oscillatory boundary layer model with emphasis on (i) the evolution of velocity profiles through the sawtooth cycle, (ii) the asymmetry in turbulence intensities during the cycle and (iii) the residual current generated in the (implied)

offshore direction by the turbulence-asymmetry. The near-bed residual current is driven entirely by boundary layer processes and, thus, will complement, for example, any undertow that may be present on site.

Model

The numerical oscillatory boundary layer model used to simulate the experimental conditions provides a time-varying description of the velocity and turbulence fields during the wave cycle. The model is a standard, local, 1DV, k-ε, turbulence closure model (Malarkey et al., 2003) in which the driving, horizontally-uniform pressure gradient has been set to correspond to the experimentally-generated sawtooth flows. The model describes well the boundary layer processes beneath velocity-skewed (Stokes type) flows, but its application to sawtooth-type flows has not been reported previously. Here the bed roughness length scale has been taken as $z_0 = D_{50}/12$ (D_{50} = median grain diameter) and the depth of water as 1.0 m (nominal value). The model has been run for 200 wave cycles to produce the converged results shown later.

Experiments

The experiments were conducted in the Aberdeen Oscillatory Flow Tunnel (AOFT), a large tunnel facility capable of generating oscillatory flows with periods and amplitudes equivalent to those of full-scale waves. The AOFT has an overall length of 16 m with a glass-sided, 10 m long, rectangular test section, 0.75 m high by 0.3 m wide. For the fixed bed experiments the bed within the test section consisted of sediment glued to a 25 mm thick marine plywood base securely fixed to a rigid frame bolted to the floor of the tunnel. The tunnel piston was programmed to generate flows with specified period T, maximum velocity u_{max} and acceleration skewness β, with zero velocity skewness (i.e., sawtooth-type oscillatory flow). A total of 12 experiments was conducted, involving two different bed roughnesses (sand with D_{50} = 0.44 mm, gravel with D_{50} = 5.65 mm), two T-u_{max} combinations (T = 5 s & u_{max} = 1 m s^{-1}; T = 7 s & u_{max} = 1.2 m s^{-1}) and three degrees of acceleration skewness (β = 0.5, 0.6, 0.75), where $\beta = \dot{u}_{max}(\dot{u}_{max} - \dot{u}_{min})$, $\dot{u}_{max}$ is maximum positive acceleration and $\dot{u}_{min}$ is the maximum negative acceleration (which has a negative value); β = 0.5 corresponds to sinusoidal flow.

Horizontal and vertical velocities were measured using an adaptive cross-correlation particle image velocimetry (PIV) system comprising a double-pulsed Nd:YAG laser illuminating a 2-d plane within the flow and a 1600 × 1200 pixel cross-correlation camera capable of recording image pairs (Δt = 1 ms) with a 15 Hz sampling rate. The area of flow measurement was 126 mm (x-direction) by 90 mm high (z-direction) and measurements were recorded over 50 oscillatory flow cycles. Image analysis used a final interrogation area of 32 × 32 pixels with 50% overlap to give velocity vectors every 1.26 mm in the x and z directions. Ensemble-averaging was carried out over 50 cycles at each location. Horizontal averaging was then carried out over 70 adjacent x-positions to yield the time-evolving velocity profiles shown below. Turbulence intensities in the horizontal and vertical directions, and also the Reynolds stress (xz-component), were extracted in an analogous manner, following subtraction of the ensemble-averaged velocities from the respective, local, instantaneous values.

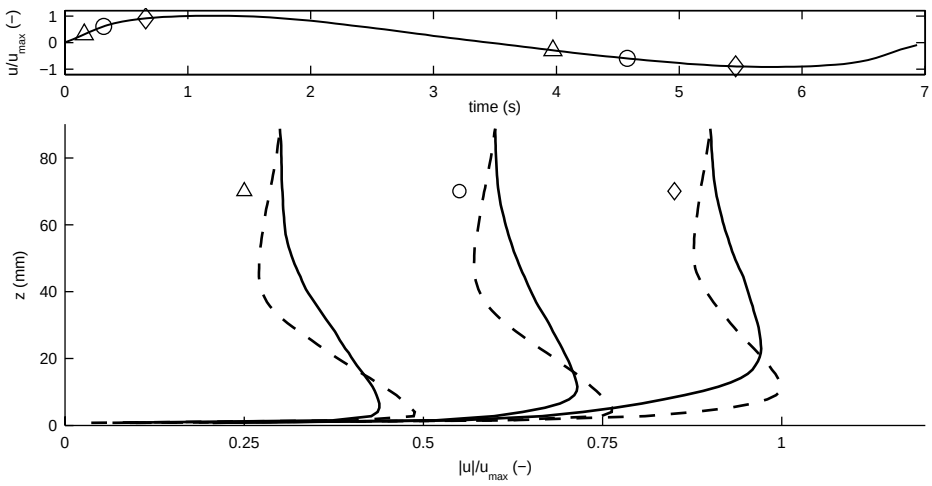

Figure 1. Normalized velocity (absolute) profiles at six phases corresponding to u/u_{max} = ±0.3 (triangle), ±0.6 (circle) and ±0.9 (diamond) for an experiment with T = 7 s, u_{max} = 1.2 m s^{-1}, β = 0.75 over the fixed bed with grain size 0.44 mm. The origin of the z-axis is at the grain crests. Positive velocity profiles (dashed) are associated with higher acceleration; negative velocity profiles (solid) are associated with lower acceleration.

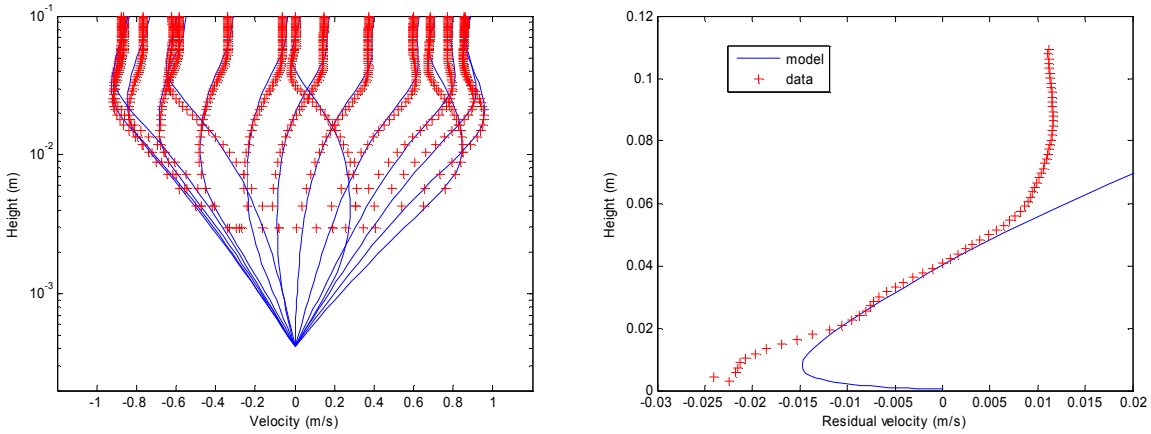

Figure 2. Left: observed (pluses) and modelled (full lines) velocity profiles at 15 instants during a sawtooth wave cycle ($T = 5$ s, $U_1 = 1.0$ m s^{-1}, $\beta = 0.75$, $D_{50} = 5$ mm). Right: corresponding residual velocity profiles.

Figure 1 shows the differences between measured velocity profiles that have the same magnitude of free-stream velocity, but different accelerations. During the strongly-accelerated part of the flow cycle following reversal ($0 < t < 1$ s) the boundary layer remains thin, as a result of which the bed shear stress increases rapidly. In contrast, following flow reversal in the weakly-accelerated part of the cycle ($3.5 < t < 6$ s) the boundary layer thickness has more time to grow and bed stresses are correspondingly smaller. Consistent with this, the experimental results show that greater near-bed turbulence intensities occur following the interval of strong deceleration and acceleration ($6 < t < 7 + 1$ s) than following the interval of weak deceleration and acceleration ($1 < t < 6$ s). As a consequence of this, a residual current is generated in the (implied) offshore direction. This phenomenon is well known in the case of velocity-skewed flows (of Stokes 2nd order type) (Davies and Li, 1997) but it has not been reported previously for sawtooth flows.

Comparisons between observations and *k*-ε model

The comparisons shown below are for the case of the fixed gravel bed, for which the origin of the vertical axis in the model has been optimized to be at a distance of $0.4\,D_{50}$ below the grain crest level.

The results in Figure 2 show that the (untuned) *k*-ε model captures the essential nature of the velocity profiles and predicts quite well the thickness of the oscillatory boundary layer. The most strongly accelerated flow occurs as the free-stream velocity changes from negative to positive values. Figure 2 shows also the near-bed drift that occurs in the (implied) offshore direction. For reasons of mass continuity in the AOFT the offshore drift must be balanced by a return flow; the sign of the residual velocity here changes at a height of 0.040 m. In order to represent this effect in the model, a steady pressure gradient has been imposed in the onshore direction, allowing the residual velocities to be matched at 0.040 m. If no such pressure gradient is applied the peak, predicted residual velocity becomes −0.028 m s^{-1} (i.e., closely similar to the observed peak value) instead of the rather lower value (−0.015 m s^{-1}) shown in Figure 2.

Figure 3 shows a comparison between the observed and predicted shear stresses. In order to secure a clear basis for this comparison, the measured velocity field has here been analyzed using the momentum defect method. The results show the pronounced asymmetry that develops between the larger/smaller magnitudes of shear stress associated with the accelerating/decelerating stages of the flow. At the lowest measurement level the data suggests that $|\tau_{max}/\tau_{min}|$ is 1.38 while the model yields a value of 1.23 at this level. The consequences for net sediment transport of such differences between the onshore and offshore stresses could be substantial. Above the near bed layer both the observations and the model show generally good agreement, with the shear stress decreasing with height and experiencing a phase shift. The rather spiky nature of the observations in Figure 3 is simply a consequence of the limited amount of smoothing that has been carried out during the analysis, and this probably explains, in part, the difference between the values quoted above for $|\tau_{max}/\tau_{min}|$.

Conclusions

The new AOFT experiments reported here have provided the most detailed set of measurements to date of the flow and turbulence beneath acceleration-skewed waves. A convincing representation of the boundary

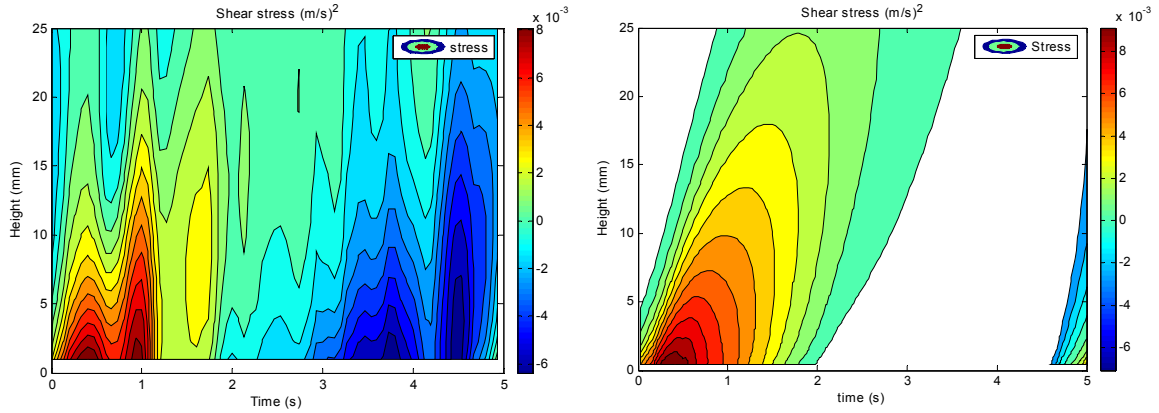

Figure 3. Shear stress (kinematic) contours (in a time-versus-height plane) for a sawtooth wave cycle ($T = 5$ s, $U_1 = 1.0$ m s^{-1}, $\beta = 0.75$, $D_{50} = 5$ mm). Left: Shear stresses determined from the observed velocity field using the momentum defect method. Right: shear stresses from the k-ε model.

layer processes, including shear stresses and wave-induced residual currents, has been provided by a k-ε turbulence-closure model. It may be inferred that the net sediment transport beneath sawtooth-type waves involves a competition between an 'onshore' wave-related flux and an 'offshore' current-related flux.

Acknowledgements

This work is part of the SANTOSS project ('SANd Transport in OScillatory flows in the Sheet-flow regime') funded by the UK's EPSRC (GR/T28089/01) and STW in The Netherlands (TCB.6586).

References

Calantoni, J., Puleo, J.A. (2006), Role of pressure gradients in sheet flow of coarse sediments under sawtooth waves, *Journal of Geophysical Research*, 111, C01010, doi:10.1029/2005JC002875.

Davies, A.G., Li Z. (1997), Modelling sediment transport beneath regular symmetrical and asymmetrical waves above a plane bed, *Continental Shelf Research*, 17(5), 555–582.

Elfrink, B., Hanes, D.M., Ruessink, B.G. (2006), Parameterization and simulation of near bed orbital velocities under irregular waves in shallow water, *Coastal Engineering*, 53, 915–927.

Gonzalez-Rodriguez, D., Madsen, O.S. (2007), Seabed shear stress and bedload transport due to asymmetric and skewed waves, *Coastal Engineering*, 54, 914–929.

Guard, P., Teakle, I., Nielsen, P., Baldock, T. (2007), *Modelling sheet flow transport using convolution integrals*. Coastal Sediments '07: Proceedings of the 6th International Symposium on Coastal Engineering and Science of Coastal Sediment Processes, May 2007, New Orleans, American Society of Civil Engineers, pp286–299.

Hsu, T.-J., Hanes, D.M. (2004), Effects of wave shape on sheet flow sediment transport, *Journal of Geophysical Research*, 109, C05025, doi:10.1029/2003JC002075.

Malarkey J., Davies, A.G., Li, Z. 2003. A simple model of unsteady sheet flow sediment transport. *Coastal Engineering*, 48(3), 171–188.

Nielsen, P. (2006), Sheet flow sediment transport under waves with acceleration skewness and boundary layer streaming, *Coastal Engineering*, 53, 749–758.

Ribberink, J.S. (1998), Bed-load transport for steady flows and unsteady oscillatory flows, *Coastal Engineering*, 34, 59–82.

Silva, P.A., Temperville, A., Seabra Santos, F. (2006), Sand transport under combined current and wave conditions: a semi-unsteady, practical model, *Coastal Engineering*, 53, 897–913.

Watanabe, A., Sato, S. (2004), *A sheet-flow transport rate formula for asymmetric forward-leaning waves and currents*, Proceedings of the 29th International Conference on Coastal Engineering, Lisbon, World Scientific, pp1703–1714.

Wave-induced Eulerian drift above vortex ripples

JEBBE J. VAN DER WERF[1, 2], JAN S. RIBBERINK[1], ALAN G. DAVIES[3]

1. Water Engineering and Management, University of Twente,
P.O. Box 217, 7500 AE Enschede, Netherlands
email: j.j.vanderwerf@utwente.nl, j.s.ribberink@utwente.nl

2. Deltares, Rotterdamseweg 185, P.O. Box 177, 2600 MH Delft, Netherlands

3. School of Ocean Sciences, College of Natural Science, Bangor University,
Menai Bridge, Anglesey LL59 5AB UK
email: a.g.davies@bangor.ac.uk

Keywords: Eulerian drift, oscillatory flow, vortex ripples, wave boundary layer, waves

ABSTRACT

Progressive surface waves induce a near-bed Eulerian drift due to the effect of vertical orbital velocities in the bottom boundary layer (see Longuet-Higgins, 1953) and asymmetry in the turbulence intensity in successive wave half cycles (see Trowbridge and Madsen, 1984). Although this wave-induced current is small relative to the horizontal orbital velocities, it is potentially important for the net sand transport since most of the sand is present in the few centimeters directly above the bed.

Davies and Villaret (1999) developed a practical model of the drift induced by weakly asymmetrical progressive waves in the bottom boundary layer above rippled and very rough beds. This model is based on velocity data from small wave flume experiments with relatively short wave periods ($T < 3$ s). Recently, van der Werf et al. (2007) carried out detailed velocity measurements above mobile ripples in full-scale oscillatory flows ($T \geq 5$ s). For fixed period, orbital velocity amplitude and grain size the degree of orbital flow asymmetry was varied. In this paper we use these data to study the effect of orbital flow asymmetry on the Eulerian drift above vortex ripples. We adjust the model of Davies and Villaret (1999) for the oscillatory flow tunnel case where the flow is purely horizontal and uniform in the horizontal direction, and compare the original and adjusted model with the oscillatory flow tunnel data.

Velocity measurements above vortex ripples

Van der Werf et al. (2007) measured the time-dependent two-dimensional vertical (2DV) velocity field above mobile ripples in full-scale regular oscillatory flows using a cross-correlation particle image velocimetry system in the Aberdeen Oscillatory Flow Tunnel (AOFT). The AOFT is a large laboratory facility in which near-bed horizontal flows, equivalent in period and amplitude to the near-bed horizontal flows induced by full-scale waves, can be generated over sediment beds. In contrast to the orbital flow induced by progressive surfaces waves, the velocity is uniform in the horizontal direction and no vertical orbital motions are present. Table 1 shows the experimental conditions. The velocity function has the same form as beneath second-order Stokes waves:

$$u(t) = U_{\infty 1}\cos(\omega t) + BU_{\infty 1}\cos(2\omega t) \qquad (1)$$

where $U_{\infty 1}$ is the first-order free-stream velocity amplitude, $B = U_{\infty 2}/U_{\infty 1}$ the degree of orbital flow asymmetry with $U_{\infty 2}$ the second-order velocity amplitude, and $\omega = 2\pi/T$ the angular frequency with T the flow period. $U_{\infty 1}$ and $U_{\infty 2}$ are based on the measured velocity outside the wave boundary layer. The table also lists the measured ripple height η, length λ and steepness η/λ. The ripples were two-dimensional. The wave Reynolds number is defined as $\mathrm{Re} = (a_1 U_{\infty 1})/\nu$, where $a_1 = U_{\infty 1}/\omega$ and ν is the kinematic viscosity (10^{-6} m^2 s^{-1}). The equivalent bed roughness is given by $k_s = 25\eta^2/\lambda$ following Nielsen (1992).

Table 1: Conditions of the experiments by van der Werf et al. (2007).

Experiment	T (s)	$U_{\infty 1}$ (m/s)	B	η (cm)	λ (cm)	η/λ	Re (10^5)	a_1/k_s
Mr5a54	5.0	0.30	0.07	6.5	31	0.21	0.7	0.7
Mr5a58	5.0	0.31	0.14	5.3	24	0.22	0.8	0.8
Mr5a63	5.0	0.31	0.18	4.4	24	0.18	0.8	1.2
Mr5d54	5.0	0.43	0.03	7.3	39	0.19	1.5	1.0
Mr5d58	5.0	0.43	0.09	6.7	35	0.19	1.5	1.0
Mr5d63	5.0	0.44	0.17	6.2	39	0.16	1.5	1.4
Mr5b54	5.0	0.55	0.05	8.2	39	0.21	2.4	1.0
Mr5b58	5.0	0.53	0.12	8.5	39	0.22	2.2	0.9
Mr5b63	5.0	0.53	0.17	8.3	39	0.21	2.2	1.0

Analytical Eulerian drift model of Davies and Villaret (1999)

Davies and Villaret (1999) (DV99) presented an analytical model for the prediction of the near-bed Eulerian drift induced by weakly asymmetrical second-order Stokes waves ($B < 0.2$) above very rough and rippled beds. Above such beds, momentum transfer is dominated by the spatially well organized process of vortex shedding, rather than by random turbulent processes. They defined a height-independent, time-varying convective eddy viscosity ν_t to characterize this vortex shedding process in a standard, one-dimensional vertical (1DV), gradient diffusion framework:

$$\nu_t = \nu_{t0}\left(1 + \varepsilon_1 e^{i\theta} + \varepsilon_2 e^{2i\theta}\right) \tag{2}$$

in which the respective terms on the right-hand side represent the mean, asymmetric and symmetric components of ν_t with ν_{t0} the time-mean eddy viscosity according to Nielsen (1992), θ is the wave phase, $\varepsilon_1 = |\varepsilon_1|\exp(i\varphi_1)$ and $\varepsilon_2 = |\varepsilon_2|\exp(i\varphi_2)$. The magnitudes of the time-varying eddy viscosity components, $|\varepsilon_1|$ and $|\varepsilon_2|$, depend on B and reflect the increasing relative importance of the asymmetric eddy viscosity contribution as the degree of orbital flow asymmetry increases. The phase angles φ_1 and φ_2 allow a phase difference between the free-stream velocity and the respective eddy viscosity components. DV99 developed phase relationships such that peak eddy viscosity occurs near flow reversal, mimicking vortex shedding. Their analysis results in three contributions to the Eulerian drift. One is related to the wave Reynolds stress (similar to the Longuet-Higgins solution) and two are related to wave asymmetry.

The model coefficients were based on data from small-scale wave flume experiments. This is illustrated in Figure 1 which shows the location of the data used by DV99, together with the new data, on the (Re, a_1/k_s)-plane that delineates flow regimes. Except for two cases, all of the data lie in the very rough turbulent regime. The range of relative roughness values is similar. However, the wave Reynolds number is an order of magnitude greater for the new data, related to the larger flow period and orbital velocities.

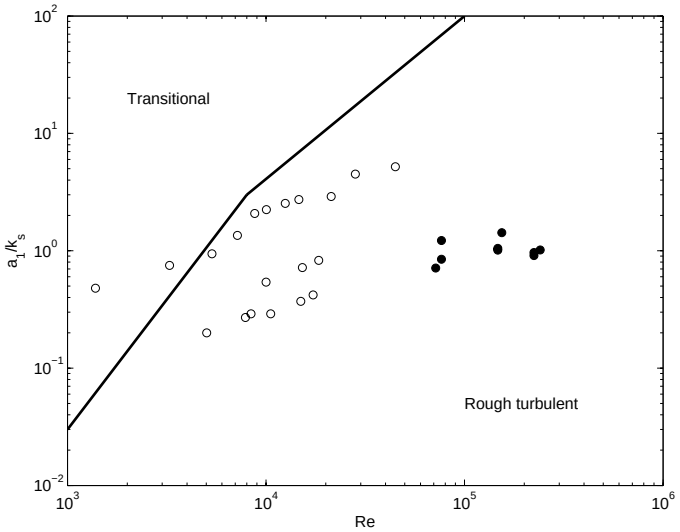

Figure 1. Delineation of flow regimes, indicating the boundary layer between transitional and rough turbulent oscillatory flow. Open circles: data used by DV99 for their model development, closed circles: new data.

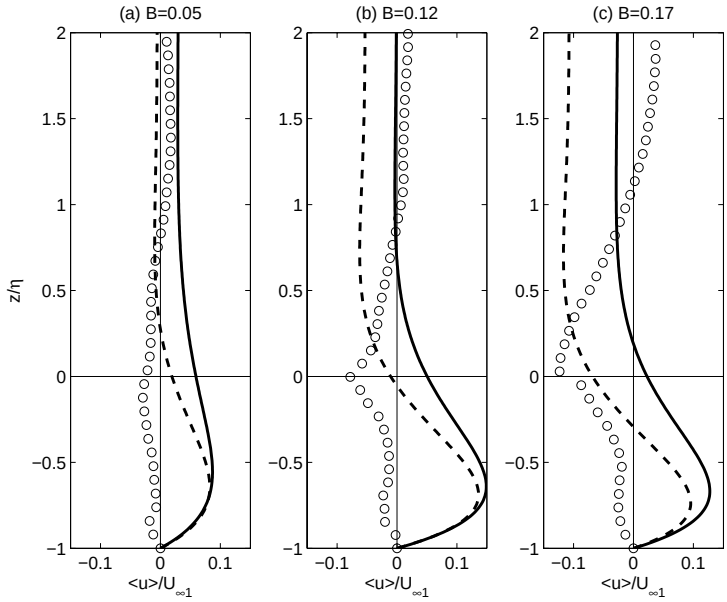

Figure 2. Eulerian drift profiles for different degrees of orbital flow asymmetry (experiments Mr5b54, Mr5b58 and Mr5b63). Open circles: measured, solid lines: original DV99 model, dashed lines: adjusted DV99 model.

In flow tunnels the oscillatory flow is purely horizontal and uniform in the horizontal *x*-direction. The DV99 solution for the Eulerian drift induced by this type of flow has two contributions:

$$\overline{U^{(1)}} = 0.5U_{\infty 1}|\varepsilon_1|\left[e^{-\alpha z}\cos(\alpha z+\varphi_1)-\cos\varphi_1\right] \tag{3a}$$

$$\overline{U^{(2)}} = 0.5BU_{\infty 1}|\varepsilon_2|\left[e^{-\sqrt{2}\alpha z}\cos\left(\sqrt{2}\alpha z+\varphi_2\right)-\cos\varphi_2\right] \tag{3b}$$

where $\alpha = [\omega/(2\nu_{t0})]^{0.5}$. The main difference with the original DV99 is the absence of the positive, 'onshore-directed' Eulerian drift contribution related to the wave Reynolds stress.

Comparison Eulerian drift model against experimental data

Figure 1 shows a comparison between measured and predicted Eulerian drift profiles for experiments Mr5b54, Mr5b58 and Mr5b63. Data are ripple-averaged. Ripple crest level is at $z/\eta = 0$; ripple trough level at $z/\eta = -1$. Davies and Villaret (1999) took the origin of z at the mid crest-to-trough level. Here we take the trough level as $z = 0$ in the model.

The measured Eulerian drift profiles comprise significant negative (against flow asymmetry) near-bed velocities and smaller positive velocities higher up in the flow. The first is the result of stronger and larger vortices on the onshore ripple flank than on the offshore ripple flank. The latter is a compensation of the negative near-bed flow, since there is no net water flow over the complete cross section of the test section of the tunnel. The model does not include this latter effect. The strong effect of asymmetry on the Eulerian drift profile is clear. Increasing asymmetry leads to an increasingly negative near-bed drift and an increasingly positive, compensating drift higher up in the flow.

The computed profiles exhibit a positive time- and ripple-averaged velocity near the bed, a level of zero velocity within the boundary layer, and a small positive or negative velocity higher up in the flow. The effect of flow asymmetry is to increase the near-bed positive velocity maximum and the flow higher up in the water column becomes increasingly negative. The measured profiles do not display the strong positive Eulerian drift between the ripple trough and crest level as given by the models. This discrepancy could be related to the fact that i) these near-bed velocities are very much affected by the underlying ripple and cannot be modelled in a 1DV way, ii) the model is based on data from wave flume experiments and/or iii) the model has been run outside its range of validity (see Figure 1). The relatively large Reynolds numbers might have an effect on the phase angles in the eddy viscosity model.

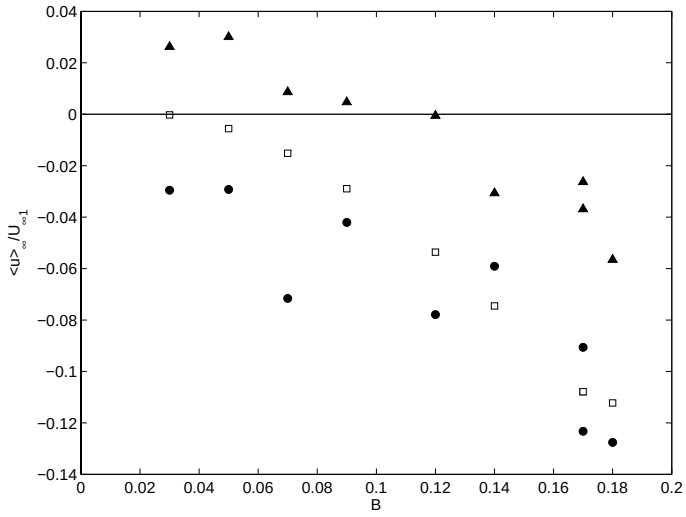

Figure 3. Eulerian drift at the edge of the boundary layer as function of the degree of orbital flow asymmetry. Closed circles: measured, open squares: adjusted DV99 model, closed triangles: original DV99 model.

Due to the absence of the positive contribution associated with the wave Reynolds stress, the Eulerian drift velocities calculated by the adjusted DV99 model are more negative and agree better with the measured velocity values. This is echoed in Figure 3 which compares the measured and computed Eulerian drift at the edge of the boundary layer. For the experimental data, the level of negative overshoot is taken as the edge of the boundary layer. The adjusted DV99 model is capable of making reasonably good predictions of the Eulerian drift at the edge of the boundary layer, especially for cases with $B > 0.09$. Possibly the results for the lower asymmetry cases could be improved by tuning the phase angles in the eddy viscosity model.

Conclusions

Flow tunnel measurements of the velocity field above full-scale, mobile vortex ripples in nine different regular, asymmetric oscillatory flows have been analyzed. The measured Eulerian drift profiles comprise strong negative (against flow asymmetry) near-bed velocities up to 10% of the orbital velocity amplitude and smaller positive velocities higher up in the flow. The effect of asymmetry is strong. Increasing asymmetry leads to an increasingly negative near-bed drift and an increasingly positive drift higher up in the flow.

The analytical model of Davies and Villaret (1999) (DV99) to predict the Eulerian drift induced by second-order Stokes waves above very rough and rippled beds has been adjusted such that it is valid for oscillatory flow tunnel cases. The main difference between the original and adjusted DV99 model is the absence of the positive, 'onshore'-directed Eulerian drift contribution related to the wave Reynolds stress. The adjusted model shows better agreement with the velocity data. However, it calculates a strong positive Eulerian drift between the ripple trough and crest level, which is not found in the measurements. This discrepancy is possibly related to the too crude schematization of the 2DV processes in a 1DV model or to running the model outside its validity range. Furthermore, the model does not reproduce the positive return flow higher up in the flow which must be present in oscillatory flow tunnels for continuity reasons. However, this simple model gives reasonably good predictions of the Eulerian drift at the edge of the boundary layer.

References

Davies, A.G., Villaret, C. (1999), Eulerian drift induced by progressive waves above rippled and very rough beds, *Journal of Geophysical Research*, 104(C1), 1465–1488.

Longuet-Higgins, M.S. (1953), Mass transport in water waves, *Philosophical Transactions of the Royal Society of London. Series A*, 245(903), 535–581.

Nielsen, P. (1992), *Coastal bottom boundary layers and sediment transport*, World Scientific, Singapore.

Trowbridge, J., Madsen, O.S. (1984), Turbulent wave boundary layers 2. Second-order theory and mass transport, *Journal of Geophysical Research*, 89(C5), 7999–8007.

van der Werf, J.J., Doucette, J.S., O'Donoghue, T., Ribberink, J.S. (2007), Detailed measurements of velocities and suspended sand concentrations over full-scale ripples in regular oscillatory flow, *Journal of Geophysical Research*, 112, F02012, doi:10.1029/2006JF000614.

Fine sediment flocculation in a tidal channel: field observations

IAIN T. MACDONALD[1], MALCOLM O. GREEN[2], STEPHEN E. COLEMAN[3], VLADIMIR I. NIKORA[4]

1. School of Environmental Sciences, University of East Anglia, Norwich NR4 7TJ UK
email: i.macdonald@uea.ac.uk

2. National Institute of Water and Atmospheric Research,
P.O. Box 11-115, Hamilton 3521, New Zealand
email: m.green@niwa.co.nz

3. Department of Civil and Environmental Engineering, University of Auckland,
Auckland 1142, New Zealand
email: s.coleman@auckland.ac.nz

4. School of Engineering, University of Aberdeen, Aberdeen AB24 3UE UK
email: v.nikora@abdn.ac.uk

Keywords: flocculation, turbulence, benthic boundary layer

ABSTRACT

Fine sediments can have detrimental effects on water quality, visibility, benthic ecosystems and bed-sediment quality. Being able to manage these effects hinges on, amongst other things, our ability to predict fine-sediment dispersal and settling.

The dynamic behavior (settling, suspension, dispersal) of fine sediments in turbulent flows is controlled by a number of processes. Flocculation plays a significant role, since this causes fine particulate matter to 'stick' together to form larger aggregates or flocs. Flocculation alters the size and settling velocity of the aggregates relative to the constituent particles, which then feeds back on the dynamic sediment behavior. Presently, our ability to make accurate predictions of fine-sediment behavior is limited by our imperfect understanding of the flocculation process.

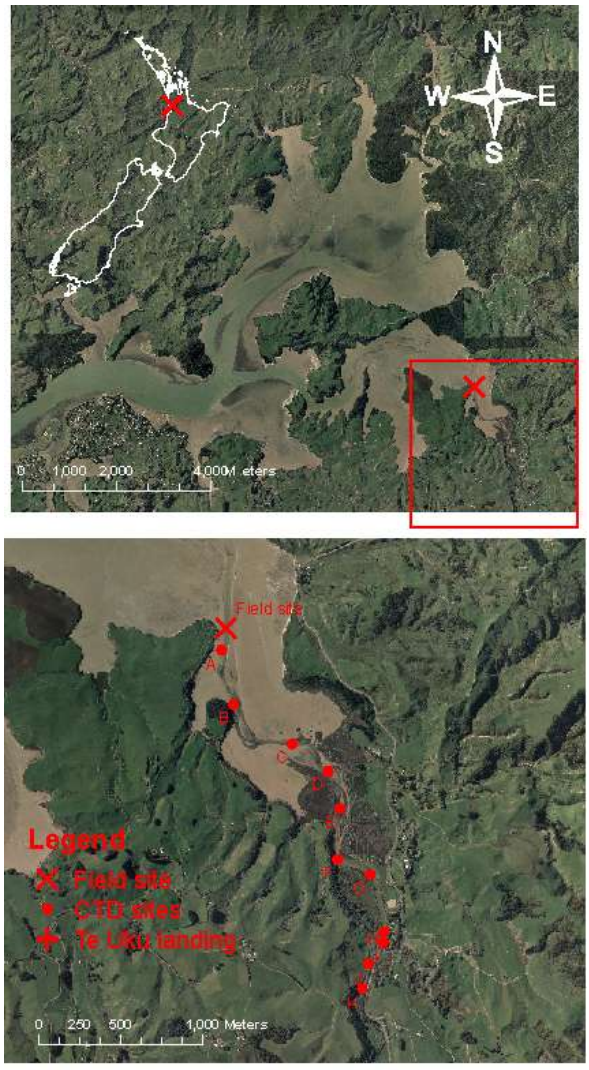

Figure 1. Raglan Harbour, NZ.

Methods

To investigate flocculation under field conditions, measurements were made in a tidal channel in the Waitetuna arm of Raglan (Whaingaroa) Harbour, North Island, New Zealand (Figure 1). Raglan Harbour is a mesotidal estuary with semi-diurnal tides, with mean neap and spring ranges of 1.4 m and 3.1 m respectively. In terms of salinity, the Waitetuna system is best described as a partially-mixed estuary. The Peak river flow is approximately 80 m^3s^{-1} and the maximum tidal discharge into the Waitetuna, under spring tide conditions is approximately 1600 m^3s^{-1}.

Sampling was conducted in a straight section of the channel (lower panel Figure 1). Water levels at this site range from a few tens of centimeters, to around 3.8 m. Peak tidal currents are typically less than 80 cm s^{-1}, but can exceed 100 cm s^{-1} during rainfall events. Salinity profiles (not shown here) have demonstrated that the maximum intrusion of the saltwater wedge occurs around site H, which is approximately 2.5 km upstream from the sampling location. Salinity profiles taken at the field site shows a stratified water column.

The aim of the field experiments is to investigate how changes in environmental parameters, namely turbulence, suspended sediment concentration (SSC) and salinity affect flocculation in the benthic boundary layer.

To achieve the aims of the field experiments, turbulence measurements were derived from velocity measurements using ADVs. The ADVs are integrated with optical backscatter sensors (OBS) to measure SSC. Salinity was obtained from measurements of conductivity and temperature. In situ particle size distributions (PSD) were measured using a LISST-ST (Type C). Water samples were collected, and subsequently analyzed back in the laboratory, to determine the size distribution of the constituent (primary) particles.

The top panel in Figure 2 shows a schematic diagram of the experimental setup. The frame to the left was setup to take measurements at three vertical positions, these being 20, 60 and 140 cm above the above the bed (cmab). Each position was equipped with ADV, OBS and CT probe. Water samples were collected at each position, via plastic tubing that was run from shore. The frame to the right was designed and built to raise and lower the LISST through the water column.

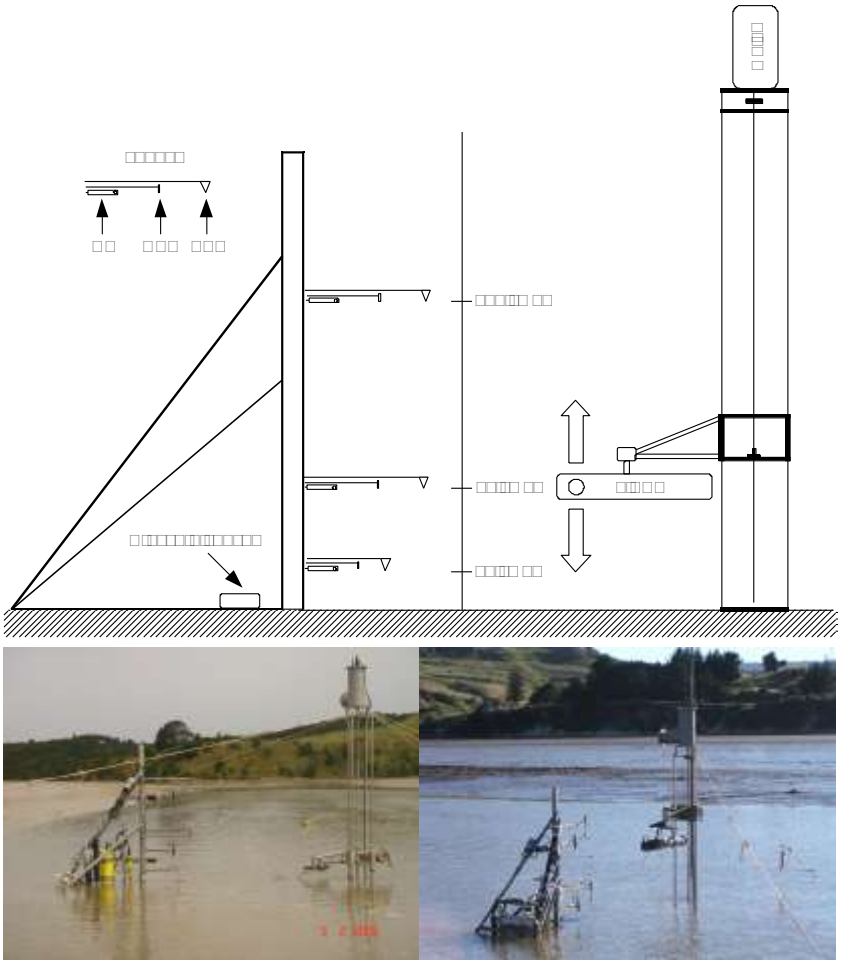

Figure 2. Experiment set up and study site.

Due to power and memory limitations all instruments were programmed to collect data in bursts. The interval between bursts was 20 minutes. It was assumed that the conditions were stationary over the burst duration such that measured series could be represented by burst-averaged values.

A critical aspect of this research is being able to identify the degree of flocculation from a measured PSD. Identifying times when the PSD is becoming more (less) flocculated will help identify the conditions that favor aggregation (breakup). To this end, it would be useful to reduce the PSD to characteristic numbers that reflect the degree of flocculation. One such number is called the floc factor (F), which is defined as

$$F = \frac{d_{50f}}{d_{50p}} \tag{1}$$

where is the median particle size of the in-situ PSD, and is the median particle size that corresponds to the primary PSD.

Despite the widespread use of the LISST, we have experienced difficulties in obtaining reliable information. In a laboratory evaluation of the LISST in a stratified fluid, Styles (2006) showed that changes in salinity can produce scattering patterns that are indistinguishable from particle scattering. This has serious operational implications for its use in the estuarine setting, where strong longitudinal and vertical salinity gradients exist. However, we are now confident that our post-processing procedures are producing reliable information, for at least part of the measured particle size distribution.

The key turbulence parameter in flocculation studies is the rate of turbulent energy dissipation (ε). As a result estimates of ε were made from the measured fluctuating velocity components based on the spectral inertial subrange. The optical backscatter intensity measured by the OBS was converted into estimates of SSC by applying a linear calibration. Salinity was determined from the conductivity and temperature measurements using the Practical Salinity Scale 1978 (PSS1978) equation.

Results

Experiments were carried out on three occasions. Table 1 summarizes the name of each experiment, the period over which the experiment took place, the tidal conditions and the season in which the experiment was carried out.

Table1. Experiment times and conditions.

Experiment name	Period	Tidal conditions	Season
JAN06	31/1/2006 to 4/2/2006	Spring	Summer
AUG06S	11/8/2006 to 14/8/2006	Spring	Winter
AUG06N	18/8/2006 to 21/8/2006	Neap	Winter

The recurring trend from all three experiments is that F (degree of flocculation) increases as both SSC and ε increase. The increase in F as the SSC increases makes sense. This is because the aggregation rate scales with the number of particles squared. However, the increase in F as ε increases does not make sense. At some stage, an inverse relationship between ε and F would be expected as floc breakup begins to dominate.

One possible explanation for why an inverse relationship between ε and F is not observed is that ε and SSC are in phase. Under this scenario, SSC and ε would increase (and decrease) at the same time. If the increased breakage associated with the increase in ε is insufficient to overcome the enhanced aggregation (driven by the increase in SSC), F would appear to increase as both ε and SSC increase, hiding the true effect of ε on F. If this is indeed what is happening then clearly SSC is the primary driver of flocculation at the measurement site.

Other results suggest that not all the changes in the PSD can be attributed to flocculation. Floc settling or erosion of flocs from the bed, for example, are likely to contribute to some of the observed changes in F.

References

Styles, R. (2006), Laboratory evaluation of the LISST in a stratified fluid, *Marine Geology*, 227, 151–162.

Influence of salinity and pH on turbulent induced mud flocculation

FRANCESCA MIETTA[1], ANDREW J. MANNING[2, 3], JOHAN C. WINTERWERP[1, 4]

1. Environmental Fluid Mechanics Section,
Faculty of Civil Engineering and Geosciences, Delft University of Technology,
P.O. Box 5048, 2600 GA Delft, Netherlands
email: f.mietta@tudelft.nl, j.c.winterwerp@tudelft.nl

2. School of Earth, Ocean and Environmental Sciences, University of Plymouth,
Drake Circus, Plymouth PL4 8AA UK
email: andymanning@yahoo.com

3. HR Wallingford Ltd., Howbery Park, Wallingford OX10 8BA UK

4. Deltares, Rotterdamseweg 185, P.O. Box 177, 2600 MH Delft, Netherlands

Keywords: mud, flocculation, salinity, pH, shear rate

ABSTRACT

An important property of cohesive sediments is that their size and settling velocity vary with the environmental conditions as a consequence of the flocculation process. The rate at which the flocs grow and the size they attain depends on hydrodynamic conditions, residence time, sediment type and properties of the water suspension such as pH and salinity. Estuaries are highly dynamic environments with constantly changing conditions where sediment is transported horizontally by currents and advection. This implies that it is difficult to understand the mechanisms leading to flocculation by means of in situ observations and that laboratory experiments are necessary. We use both full scale settling column with oscillating grid (Maggi et al., 2002) and jar tests. Jar tests are widely used for flocculation experiments: Serra and Colomer (2007) and Coufort et al. (2005) did extensive studies on the properties of the generated turbulence and its effects on flocculation. A propeller generates a non-homogeneous turbulence field with turbulent intensity higher close to the propeller. An oscillating grid generates a more homogeneous turbulent field. The advantage of a settling column is a residence time which can be changed by changing the height of the column. The residence time in the turbulent field with respect to the flocculation time is important for the determination of the equilibrium size of flocs.

The study presented in this paper consists of a series of flocculation experiments where pH, salinity and shear rate are varied to observe flocculation time as well as equilibrium floc size. The experiments are done both in a jar stirred by a propeller and in a settling column with an oscillating grid. When the jar test is used, the flocs' sizes are measured using laser diffraction while imaging techniques are used in the settling column experiments. The material used is mud from the Western Scheldt which has been characterized by measuring the organic matter content, the primary particles size distribution and the zeta-potential under different physicochemical conditions. The results of the flocculation experiments are discussed in relation with the values of the zeta-potential measured under the same conditions. Some of the results obtained with the jar tests are compared to the ones obtained with a settling column.

Materials

The material used is natural mud from the Western Scheldt sampled in October 2007 near Antwerp. The organic matter content measured by loss on ignition is 6.56% by mass. 2% by mass of the material is smaller than 2 μm and 93% is smaller than 63 μm. The pH has been changed by adding hydrochloric acid HCl and sea salt has been artificially created through a combination of KCl, NaCl, $MgCl_2$, $CaCl_2$. The zeta-potential has been measured by means of a Malvern zeta-sizer, the concentration of the sediment during the measurements is $c_{MUD} = 0.05$ g l^{-1}.

Jar tests are performed in cylinders of 125 mm diameter with four baffles each 14 mm large. The water depth is 85 mm. The suspension is stirred with a rectangular paddle with a width of 75 mm and an height of 25 mm

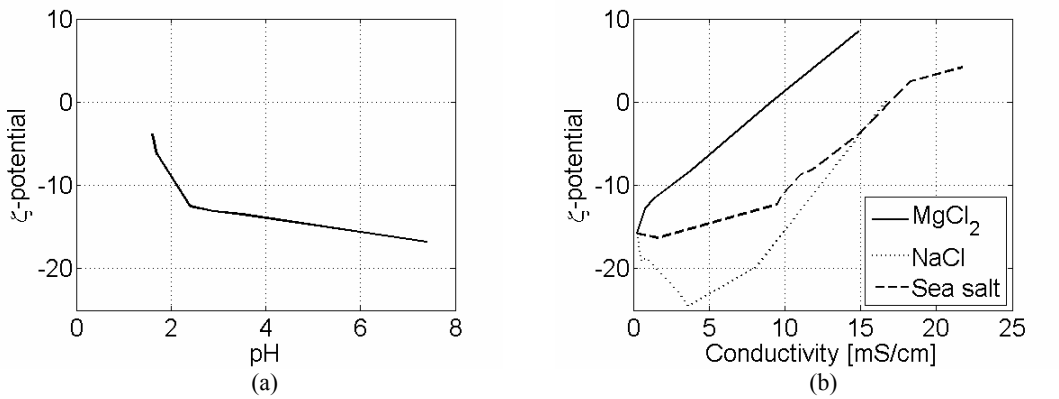

Figure 1. Zeta-potential of mud measured for different pH (a) and salinities (b).

which is rotating around its axis close to the bottom of the jar. The shear rate G is computed from the rotational frequency of the propeller by measuring the power consumption (KIWA, 1976). The volume based floc size distributions are measured every 40 seconds through laser diffraction with a Malvern Mastersizer 2000. To ensure uniform initial conditions, the suspension is stirred at $G = 400\ s^{-1}$ each experiment.

The settling column used for the experiments is described in Maggi et al. (2002). A highly-concentrated suspension, continuously mixed in the storage tank, is injected into the buffer tank mounted on top of the settling column, where two counter rotating vanes generate a uniform sediment distribution at the top of the settling tube. The concentration in the buffer tank is kept equal to the test concentration c_c via a controlled system which activates an injection pump when the measured mass concentration in the buffer tank is lower than c_c. The settling column is 4.7 m high and 280 mm in diameter. Herein, a homogeneous turbulence field, produced by an oscillating grid, induces flocculation. The grid is 4 m high and consists of meshes of 75 mm size with square cross-sectioned rods and deck distance of 75 mm. The relation between the oscillating frequency and the shear rate G has been obtained from LDA measurement by Maggi (2005). The whole settling column is placed in a climate-controlled room at $T = 20°C$ to minimize temperature gradients and convective flows.

Results

Zeta-potential

The zeta-potential has been measured using the Malvern zeta-sizer. The zeta-potential gives an indication of the charge of the particles and when its absolute value is close to zero the suspension is unstable and particles are likely to flocculate. On the contrary, when the zeta-potential is large in absolute value the repulsive forces between particles are large and it is difficult for aggregation to occur. Figure 1a shows the zeta-potential as a function of the pH of the suspension while Figure 1b shows the zeta-potential as a function of the salt concentration of the suspension. The zeta-potential decreases for decreasing pH and increasing salinity.

Jar tests

Figure 2a shows the evolution of the average of the mass based distribution for different shear rates for a suspension of mud in tap water (zeta-potential = −16 mV). Flocculation takes long time and the increase in average floc size is small. The shear rate which generates larger flocs is $G = 23\ s^{-1}$ and shear rates smaller or larger than this value lead to the formation of smaller flocs. Figure 2b shows the results of flocculation tests when a mixture of salt comparable to sea salt is added to obtain the same salinity as in the Western Scheldt (zeta-potential = −12.6 mV). In this case flocculation is faster and flocs grow larger than in the previous case. Shear rates of $G = 12\ s^{-1}$ and $G = 35\ s^{-1}$ lead to the formation of larger flocs. Figure 2c shows the evolution of the average size in a suspension with pH = 1.8 (zeta-potential = −4 mV). In this case flocculation occurs very fast and large flocs are formed. The average values corresponding to $G = 12\ s^{-1}$, $G = 23\ s^{-1}$ and $G = 35\ s^{-1}$ are very similar while increases in shear rate lead to the formation of smaller flocs.

In Figure 2b the effect of the shear rate on the rate of floc growth can be observed. When the shear rate is small, flocculation takes time and the evolution of the average size shows two different curvatures. The time corresponding to the inflection point decreases with increasing shear rate up to the limit where the curve

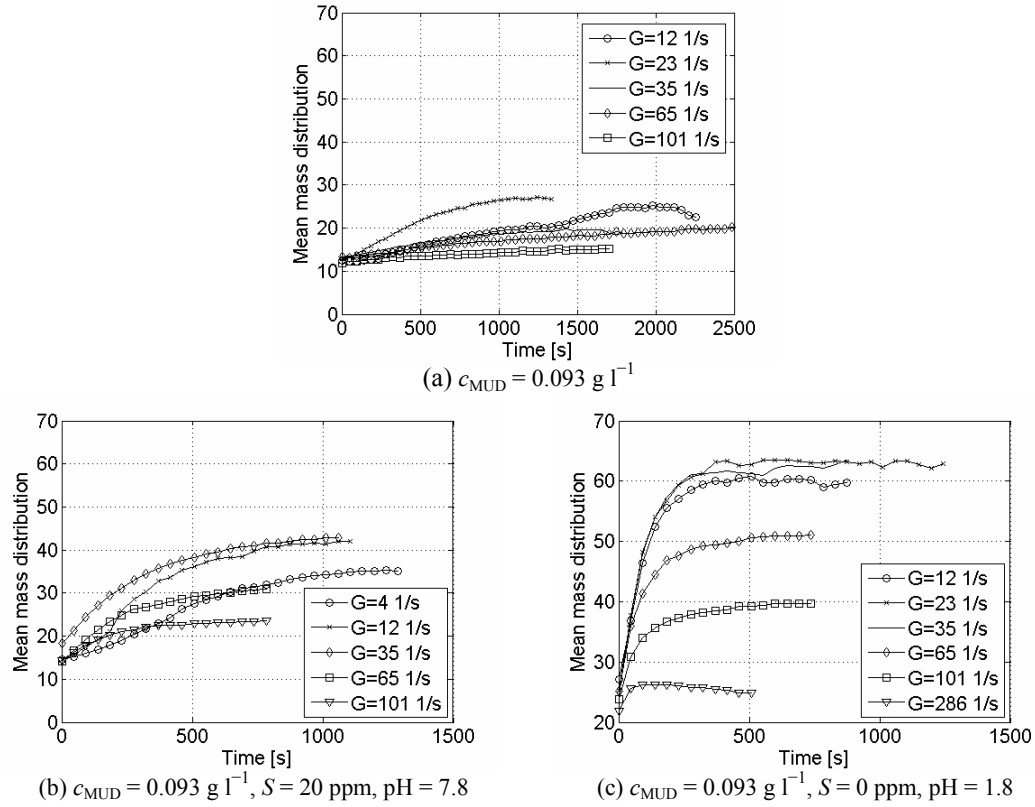

(a) c_{MUD} = 0.093 g l^{-1}

(b) c_{MUD} = 0.093 g l^{-1}, S = 20 ppm, pH = 7.8

(c) c_{MUD} = 0.093 g l^{-1}, S = 0 ppm, pH = 1.8

Figure 2. Evolution of the average size for different shear rates for mud in tap water (a), saline suspension (b) and acid suspension (c). Note the difference in time scales.

shows only one curvature (G = 35 s^{-1}). For high values of the shear rate floc growth starts very fast and decreases when approaching the equilibrium size. Differences in floc growth for different shear rates cannot be observed in the other two cases since flocculation is very slow in tap water and very fast at pH = 1.8.

Settling column

The Scheldt sediment present in the settling column was agitated by an oscillating grid, with a nominal stroke of 10 cm, installed inside the column to produce turbulence within the flow. Turbulent shear G-values in the column ranged from 1–10 s^{-1}. Flocs representative of the column ambient conditions were extracted from the settling column a height of 0.93 m above the base. Due to the hydrostatic pressure created by the fluid (salinity = 20) in the 4.7 m high column, a dual valve floc sample chamber (FSC) was constructed to facilitate floc acquisition in the lower section of column. The tubular FSC was 24 cm in length and had an internal bore diameter of 18 mm. The tube was connected to an extraction port located in the column outer wall and when the valves were opened in a preselected sequence, flocs were allowed to pass, without interference, from the column into the tube.

Once the valves were closed, the FSC was detached from the column. Floc sizes and settling speeds of each population were observed using the low intrusive, video-based LabSFLOC – Laboratory Spectral Flocculation Characteristics – instrument (Manning, 2006). A representative mud floc suspension was then careful extracted from the FSC using a proven modified pipette technique (e.g., Gratiot and Manning, 2004), and then quickly transferred to the 190 mm high by 100 mm square Perspex LabSFLOC column. The settling floc populations were observed (within a controlled sample volume) by a high resolution (10 μm lower limit) monochromatic video camera (Manning and Dyer, 2002). The camera was mounted in a viewing port located in the side wall of the Perspex LabSFLOC column a depth of 115 mm below the column surface.
Individual floc size (D) and settling velocity (Ws) measurements of the Scheldt Estuary mud were obtained from the LabSFLOC video recordings during post-processing. By implementing a series of computational algorithms originally derived by Fennessy et al. (1997) and later modified by Manning (2004), it was possible to accurately estimate numerous individual floc properties, including: floc dry mass, effective

density, porosity, fractal dimensions, and mass settling flux. These floc properties will be described in terms of their spectral distributions.

Conclusions

During 2005 Manning et al. (2007) conducted in situ floc measurements during neap tides in the Lower Estuary as part of the High Concentrated Benthic Suspension (HCBS) series of field campaigns (e.g., Manning and Sas, 2006). These surveys were commissioned by the Flemish government in order to improve the sediment transport modeling in the Antwerp region before and after the construction of Deurganckdok tidal dock. The turbidity maximum (TM) is present in the Antwerp region of the Scheldt Estuary, and as such significant changes of sediment concentration and shear stress can occur. This in situ study revealed that within the TM zone the suspended sediment concentration reached 277 mg l^{-1} and the floc mass distribution was bi-modal, with 80% of the population comprising macroflocs up to 507 μm in diameter. These macroflocs had individual settling velocities ranging from 1 to 11 mm s^{-1}. The macroflocs ($D > 160$ μm) presented 88% of the floc mass, had a $Ws_{macro} = 3.9$ mm s^{-1} and contributed to 97% to the total settling flux. These natural in situ Scheldt mud floc properties will be compared with both the controlled Jar Test and Settling Column laboratory results.

In the jar tests different parameters have been widely changed to investigate the flocculation behavior of the sediment. In particular from Figure 2c it can be observed that when the pH of the suspension is very small, and the zeta-potential close to zero, large flocs are formed and flocculation is very fast. In the other two cases, where the zeta-potential is large in absolute value, formed flocs are smaller and flocculation time is larger. This is coherent with what expected from the definition of the zeta-potential and suggests that the zeta-potential, together with the physico-chemical properties of the suspension, can be used as a useful parameter to characterize natural sediment.

References

Coufort, C., Dumas, C., Bouyer, D., Liné, A. (2007), Analysis of floc size distributions in a mixing tank. *Chemical Engineering and Processing,* 47, 187–194.

Fennessy, M.J., Dyer, K.R., Huntley, D.A., Bale, A.J. (1997), *Estimation of settling flux spectra in estuaries using INSSEV*. In: Cohesive Sediments – Proceedings of the INTERCOH Conference. (Wallingford, England), Chichester: John Wiley & Son, Burt, N., Parker, R., Watts, J. (Eds.), pp87–104.

Gratiot, N., Manning, A.J. (2004), An experimental investigation of floc characteristics in a diffusive turbulent flow. In: P. Ciavola and M. B. Collins (Eds), *Sediment Transport in European Estuaries*, *Journal of Coastal Research*, SI 41, 105–113.

KIWA (1976), *Bekerglasproef voor coagulatie: mengtijden en G-waarden*. Report number SW151.

Maggi, F. (2005), *Flocculation dynamics of cohesive sediments*. PhD Thesis, TU Delft, Delft, Netherlands.

Maggi, F., Winterwerp, J.C., Fontijn, H.L., van Kesteren, W.G.M., Cornelisse, J.M. (2002), *A settling column for turbulence-induced flocculation of cohesive sediments*. Proceedings of HMEM2002 Conference, Wahl, T.L., Pugh, C.A., Oberg, K.A., Vermeyen, T.B. (Eds.), Estes Park, Colorado, paper 93, doi:10.1061/40655(2002)34.

Manning, A.J. (2004), Observations of the Properties of Flocculated Cohesive Sediment in Three Western European Estuaries, *Journal of Coastal Research Special Issue*, SI 41, 70–81.

Manning, A.J. (2006), *LabSFLOC – A laboratory system to determine the spectral characteristics of flocculating cohesive sediments*. HR Wallingford Technical Report, TR 156.

Manning, A.J., Dyer, K.R. (2002), The use of optics for the in-situ determination of flocculated mud characteristics, *Journal of Optics A: Pure and Applied Optics*, Institute of Physics Publishing, 4, S71–S81.

Manning, A.J., Martens, C., de Mulder, T., Vanlede, J., Winterwerp, J.C., Ganderton, P., Graham, G.W. (2007), Mud floc observations in the turbidity maximum zone of the Scheldt Estuary during neap tides. *Journal of Coastal Research*, SI 50, 832–836.

Manning, A.J., Sas, M. (2006), *Report 3: Settling velocity of the sediment–INSSEV – Winter 2005*. IMDC Technical report of flocculation and hydrodynamic measurements at Deurganckdok location, Lower Scheldt Estuary (Port of Antwerp, Belgium). Project: Field measurements – high-concentration benthic suspensions (HCBS1), Doc. Ref.:I/RA/11265/05.016/MSA, 212pp.

Serra, T., Colomer, J., Logan, B.E. (2008), Efficiency of different shear devices on flocculation. *Water Research*, 42, 1113–1121.

Effect of flocculation processes on the transverse distribution of cohesive sediment in tidal estuaries

HENK M. SCHUTTELAARS[1], HUIB E. DE SWART[2], STEFAN A. TALKE[3], KARIN M.H. HUIJTS[2]

1. Delft Institute of Applied Mathematics, Delft University of Technology, Mekelweg 4, 2624 CD Delft, Netherlands
email: h.m.schuttelaars@tudelft.nl

2. Institute for Marine and Atmospheric Research Utrecht, University of Utrecht, P.O. Box 80000, 3508 TA Utrecht, Netherlands
email: h.e.deswart@phys.uu.nl, k.m.h.huijts@phys.uu.nl

3. Department of Civil and Environmental Engineering, University of Washington, P.O. Box 352700, Seattle WA 98195-2700, USA
email: stalke@u.washington.edu

Keywords: flocculation, high concentrations, sediment trapping; Ems estuary

ABSTRACT

In many estuaries the cross-sectional distribution of suspended sediments shows large variability in both time and space, as illustrated by data collected at the Ems estuary, located at the German-Dutch border. The Ems estuary has a length of approximately 100 km, a tidal current amplitude of ~0.8–1.5 m s^{-1} and a river discharge of 100 m^3 s^{-1}. The estuary is well-mixed with respect to salinity. The suspended sediment mainly consists of cohesive material.

In Figure 1a, we show the suspended sediment concentration in g l^{-1} at a fixed position as a function of time to illustrate its temporal variability: high concentrations are observed during maximum flood (time ~11 hours from midnight) and maximum ebb (approximately 17 hours from midnight). The maximum concentration during ebb exceeds the maximum concentration during flood and is whirled up higher in the water column. During high water slack, very low concentrations are observed in the water column. During low water slack, however, the concentrations are high again. The cross-sectional distribution of suspended sediments at a fixed time is illustrated in Figure 1b. This concentration profile is measured during flood and shows that a high concentration of sediment is present both on the left-hand and right-hand side of the estuary.

To gain fundamental knowledge about the physical mechanisms underlying the distribution of sediment in estuarine cross-sections, a process-based analytical model has been developed and analyzed (Huijts et al., 2006). In this model, processes such as flocculation, hindered settling and the damping of turbulence due to the presence of sediment are neglected which can be justified in case that sediment concentrations are low enough.

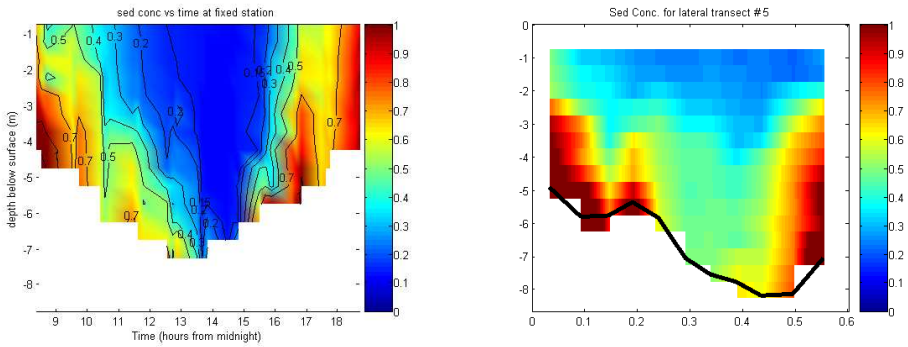

(a) Sediment concentration at a fixed location in transect 5

(b) Sediment concentration in transect 5, taken at t ~11:15 hours after midnight

Figure 1. Observations of sediment concentrations in transect 5, approximately 50 km from the seaward boundary. The data were collected on 21st September 2006.

However, observations in the Ems locally show suspended sediment concentrations up to a few grams per liter at the surface and tens of grams per liter near the bed. Based on these considerations, the main aim of this presentation is to develop an analytical model that includes the effect of a non-constant settling velocity (due to flocculation processes) and analyze the influence of non-constant settling velocity on the trapping of sediment.

Model

The model assumes along-channel uniform conditions with a bed profile arbitrary in the across-channel direction. The flow is governed by the shallow water equations and forcing is due to tides, river discharge, horizontal density gradients and wind. The resulting system of equations resembles that used in Huijts et al. (2006), but there are important differences. The first one is the boundary condition at the bottom: in this contribution we apply a partial slip formulation whereas Huijts et al. (2006) used a no slip boundary condition. Furthermore, the importance of the various forcing terms is slightly different. From observations in the Ems estuary, it is found that the lateral residual flow due to *residual* lateral density gradient is of the same order of magnitude as the lateral M_2 velocities due to the Coriolis deflection of the M_2 longitudinal velocity that is forced by the M_2 tidal discharge. Since we want to focus on the sediment transport and its trapping, it turns out that, using this observation, only the leading order longitudinal and lateral velocity components have to be calculated. After scaling the equations and using perturbation techniques, the required velocity components are obtained analytically.

The sediment transport is computed from a concentration equation, in which erosion of sediment by the bed shear stress is limited by the availability of sediment. After scaling the governing equation reads

$$\frac{\partial c}{\partial t} - \frac{\partial}{\partial z}\left(w_{\mathrm{s}} c + K_{\mathrm{v}} \frac{\partial c}{\partial z}\right) = 0, \tag{1}$$

with boundary conditions

$$w_{\mathrm{s}} c + K_{\mathrm{v}} \frac{\partial c}{\partial z} = 0 \quad \text{at} \quad z = 0 \qquad \text{and} \qquad K_{v} \frac{\partial c}{\partial z} = w_{\mathrm{s}} c_{\star} \quad \text{at} \quad z = -h\,(y). \tag{2}$$

Here c denotes the suspended sediment concentration, w_{s} is the settling velocity, K_z the constant vertical eddy diffusivity coefficient, $c_{\star}$ is a reference concentration and $z = -h(y)$ denotes the location of the bottom. The reference concentration is proportional to the bed shear stress and a laterally varying erosion coefficient that models the amount of sediment available for resuspension at the bed.

In general, the settling velocity can be written as the settling velocity of a single floc, modified for processes such as hindered settling, etc. (for details, see Winterwerp, 2002). Furthermore, high concentrations of suspended sediment result in damping of turbulence. Huijts et al. (2006) used a constant settling velocity. This is a good approximation for small sediment concentrations but has to be adopted when high sediment concentrations are considered. Motivated by van Leussen (1999), we model the settling velocity proportional to the concentration c,

$$w_{\mathrm{s}} = w_{\mathrm{s0}} + w_{\mathrm{s,ref}} \frac{c}{c_{\mathrm{ref}}}, \tag{3}$$

with $w_{\mathrm{s0}} = 0.5$ mm s^{-1}, $w_{\mathrm{s,ref}} = 1$ mm s^{-1} and $c_{\mathrm{ref}} = 1$ g l^{-1}. Hence, the formation and break up of the flocs, hindered settling and the coupling between turbulence and viscous damping are not considered in the contribution. The laterally varying erosion coefficient is resolved from imposing a morphodynamic equilibrium condition such that there is no net evolution of the bed.

Method

The system of equations that describes the water motion is solved analytically. Using these results, the bed shear stress (which is present in the reference concentration $c_{\star}$) is calculated. Since both residual and M_2 velocity components are present, the bed shear stress contains a residual, an M_2 component and all its overtides. This implies that the concentration c consists of all these components as well.

In this paper we want to focus on the convergence of the advective sediment fluxes in the lateral direction. Based on this consideration and the observation that the lateral velocity only consists of a residual and M_2 tidal component, we only need the residual and M_2 components of the concentration c. Considering the nonlinearity in Equation 1 (due to the dependence of the settling velocity w_s) and the magnitude of the various harmonic components of the bed shear stress, we can restrict our attention to the residual concentration, the M_2 and the M_4 constituent.

To actually solve for the harmonic components of the concentration, an iterative approach has to be taken as the concentrations depend nonlinearly on the unknown laterally varying erosion coefficient (which is present in the reference concentration $c_\star$). This laterally varying erosion coefficient can only be calculated if the concentrations are known, using the condition for morphodynamic equilibrium. Fortunately, if the settling velocity is taken independent of the concentration, the concentrations are linearly dependent on the laterally varying erosion coefficient. In this case the erosion coefficient can be easily obtained. Using this solution for concentration-independent settling velocity and a standard continuation method, the sediment concentrations and the corresponding laterally varying erosion coefficient are obtained.

Results

The bottom topography and residual lateral density gradient, used in the experiments, are obtained from measurements in the Ems estuary. The Coriolis parameter equals 8.8×10^{-5} s^{-1}, the friction parameter (Schramkowski and de Swart, 2002) equals 0.001 m s^{-1}, vertical eddy viscosity and diffusivity 0.001 m^2 s^{-1} and horizontal diffusivity is taken equal to 3 m^2 s^{-1}. The prescribed tidal discharge is chosen such that a good comparison between observations and model results is found (not shown).

In Figure 2 the total, time-dependent concentration is shown near the left bank of the estuary. Figure 2a shows the concentration for time-independent settling velocity, Figure 2b for a settling velocity depending on concentration. Both time series show that during ebb (t ~0.7 T) the concentrations are higher than during flood (t ~0.2 T). The main difference between the two experiments is the distribution of the sediment in the vertical: compared to the results obtained with w_s constant, the experiment with concentration-dependent settling velocity shows much larger concentrations at the bed and lower concentrations at the surface. When comparing to observations (Figure 1a), it is seen that the concentrations at the surface are in better agreement when a non-constant settling velocity is taken during slack. However, during ebb and flood, the sediment does not get high enough in the water column.

Figure 3 shows the tidally-averaged suspended sediment concentration in morphodynamic equilibrium for experiments with w_s constant (Figure 3a) and non-constant (Figure 3b), respectively. In both cases the sediment is trapped at the left bank, the main difference again is in the vertical distribution of the suspended sediments: when the settling velocity is taken non–constant, higher concentrations are observed near the bed and the sediment concentration at the free surface is lower, compared to the results obtained with constant settling velocity.

If the settling velocity is taken constant, increasing the amount of sediment in the system does not influence the location where the sediment is trapped. However, when the settling velocity is non-constant, the trapping location can change considerably (see Figure 4): for bottom concentrations ~10 g l^{-1}, most sediment is still

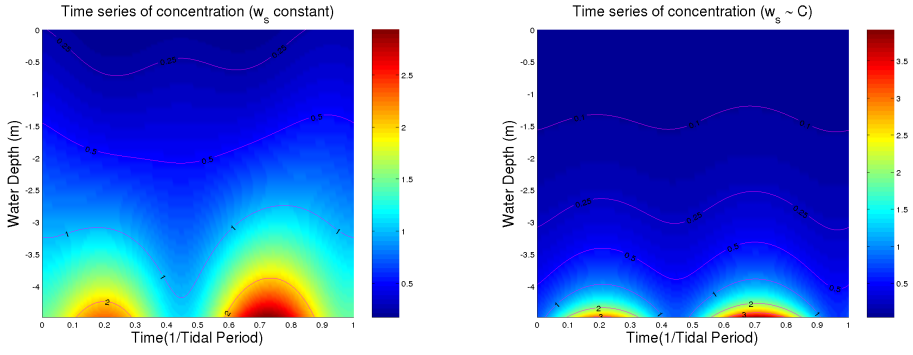

(a) Constant settling velocity (b) settling velocity depending on concentration

Figure 2. Time series of the vertical distribution of suspended sediment near the left bank.

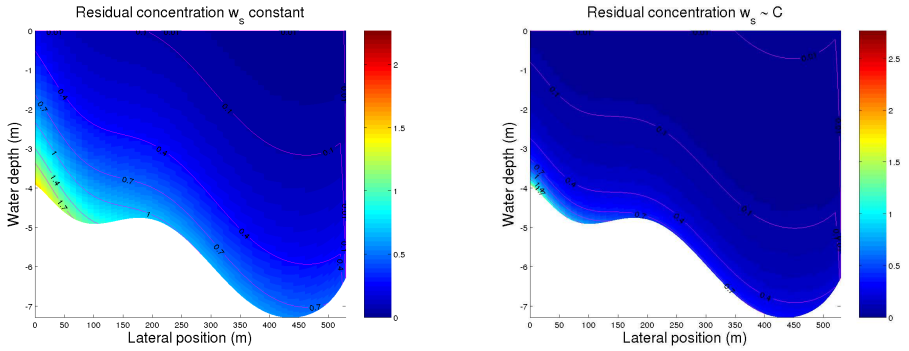

(a) Constant settling velocity (b) settling velocity depending on concentration

Figure 3. Tidally-averaged sediment concentrations.

found at the left bank, but a second maximum starts to appear ~400 m from the left bank. If the bottom sediment concentration is further increased to ~25 g l^{-1}, some sediment is still trapped near the left bank, but most sediment is found near x ~400 m. The presence of a second turbidity maximum seems to be supported by data as well (see Figure 1b). However, this comparison has to be further substantiated as Figure 1b only shows the concentration at a fixed time, whereas the trapping locations refer to tidally-averaged concentrations.

The trapping of sediment near 400 m can be understood as follows: due to the very high concentration of sediment at the bed, the sediment is transported downhill from the steep side of the channel, left from x ~400 m due to diffusive transport in the lateral direction. On the other hand, the residual circulation tries to transport the sediment uphill. This results in the observed convergence of sediment around x ~400 m.

Conclusions

Results show that flocculation processes have a strong effect on across-channel sediment distribution. The model is applied to a 500 m wide cross-section of the Ems estuary in Germany. In that transect, observations of flow, sediment concentration and salinity were collected over a full tidal cycle (cf. Figures 1a and 1b). A preliminary comparison of model results and observations over part of a tidal cycle shows an improved agreement between model results and observations when flocculation effects are incorporated.

However, some discrepancies are observed as well. The sediment, for example, does not get high enough in the water column when the settling velocity is non-constant. Therefore, the model formulation will be improved by considering effects such as damping of turbulence and hindered settling, effects that are not included in the present model.

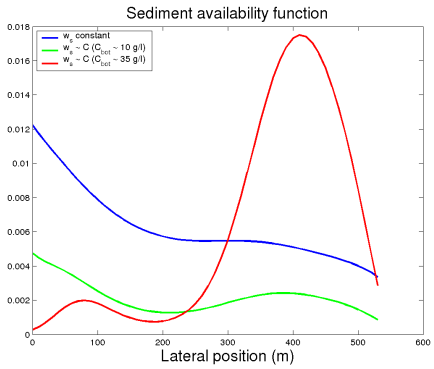

Figure 4. Dependence of laterally varying erosion coefficient on the bottom concentration and formulation of settling velocity.

References

Huijts, K.M.H., Schuttelaars, H.M., de Swart, H.E., Valle-Levinson, A. (2006), Lateral trapping of sediment in tidal estuaries: an idealized model, *Journal of Geophysical Research*, 111, C12016, doi:10.1029/2006JC003615.

van Leussen, W. (1999), The variability of settling velocities of suspended fine-grained sediment in the Ems estuary, *Journal of Sea Research*, 41, 109–118.

Schramkowski, G.P., de Swart, H.E. (2002), Morphodynamic equilibrium in straight tidal channels: Combined effects of Coriolis force and external overtides, *Journal of Geophysical Research*, 107, C12, 3227, doi:10.1029/2000JC000693.

Winterwerp, J.C. (2002), On the flocculation and settling of estuarine mud, *Continental Shelf Research*, 22, 1339–1360.

Observations of fine sediment resuspension by wind waves in the intertidal mudflats of a mesotidal lagoon (Arcachon, France)

ALDO SOTTOLICHIO[1], ANTHONY RAMBERT[1], ALEXIS AMOURIC[1], JEAN PAUL PARISOT[1], ROMARIC VERNEY[2], SERGE ROBERT[3]

1. Université Bordeaux 1, Laboratoire EPOC, avenue des Facultés, 33405 Talence Cedex, France
email: a.sottolichio@epoc.u-bordeaux1.fr, parisot@epoc.u-bordeaux1.fr

2. IFREMER Centre de Brest, Dyneco-Physed, BP 70, 29280 Plouzané, France
email: rverney@ifremer.fr

3. CRELA, Place du Séminaire, BP 5, 17137 L'Houmeau, France
email: srobert@ifremer.fr

Keywords: wind waves, tidal flats, sediment transport, coastal lagoon, bottom erosion

ABSTRACT

In intertidal areas protected from oceanic swell, wind waves play a key role on sediment dynamics, as they can be the only forcing able to generate significant erosion of the bed. The Arcachon lagoon is a mesotidal embayment of the French Atlantic coast where 74% of its total area is occupied by sheltered flats. The aim of this study was to characterize wind waves generation and their effect on intertidal sediment transport. Experiments consisted of continuous recording of water level, bed level, velocity currents and suspended sediment concentrations during one month, under winter conditions. Collected data showed that western winds associated to Atlantic low pressures can generate wind waves of 10–40 cm high with periods of 2–5 s. They also gave evidence of an increase of the wave height when tidal currents and wind are in the same direction. In terms of forcing, bottom shear stress generated by the most energetic wind waves is ten times higher than shear stress generated by tidal currents on intertidal flats. Suspended sediment concentration under wind wave action is in the order of 250 mg l^{-1}, whereas the bed can experience erosion of about 1–3 cm depending on sediment erodibility. After the windy episode, under fair weather conditions, the bed tends to recover its initial level, as tidal currents allow residual fluxes from the channel towards the inner part of the flat. These results highlight that short-term processes are of the same order than long-term residual accretion of the lagoon, estimated to be around 10 cm per century on average.

Introduction

Several studies have focused on physical processes in intertidal flats, which are governed by dynamics of waves and tidal currents (Shi and Chen, 1996; Le Hir et al., 2000; Janssen-Stelder, 2000). The Arcachon Lagoon is a mesotidal embayment located in the Atlantic coast of SW France. It is a major centre for oyster farming and spat production and a recreational area. Its total surface is about 156 m^2, of which 115 m^2 are occupied by wide intertidal areas protected from oceanic swell and drained by a network of thin channels. The intertidal flats are known to be in weak accretion under the effect of tidal currents. Evidence of accretion is only available from bathymetric charts, which show an average rate of 10 cm per century. In these areas, wind-induced waves can play an important role in sediment dynamics, leading to bed resuspension in an intermittent but more intense way than that due to tidal currents alone. The characterization of such episodes is important for a better understanding of the short-term functioning of the lagoon, in terms of morphodynamics but also water turbidity. The aim of this study is to characterize wind waves and to assess relative importance of currents and wind waves on fine sediment resuspension.

Methods

Field observations consisted of the deployment of eight Altus probes distributed in different areas of the lagoon, for duration of 8–10 weeks in the winter season, from December 2006 to February 2007. The Altus

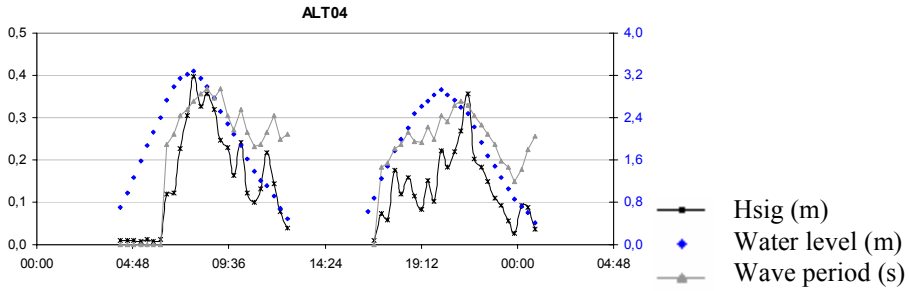

Figure 1. Example of wind wave evolution recorded by the Altus altimeters at Station 04 over two consecutives tidal cycles on 8 December 2006. Left axis: wave height in meters. Right axis: period in seconds, tidal level in meters.

probes (from NKE ©) are ultrasonic altimeters capable of measuring bed level with a precision of ±2mm. They are also equipped with a pressure sensor which gives information of water level: tidal height, waves height and period. The use of such instruments have proven to be effective tools to record accurately changes on bed level and forcings in intertidal areas (Bassoullet et al., 2000, Verney et al., 2007). The probes were installed in the lower portion of the mudflats, near the edge of the channels, in order to get advantage of long recovering periods and to optimize wave record. Records were performed at the frequency of 4 Hz. At two stations, the instrumental set was completed by an ADV velocimeter coupled to an OBS turbidimeter to record continuously velocity and suspended sediment concentration. Finally, sediment samples were taken at each station, at the beginning and at the end of the deployment. Grain size and shear strength analysis were made at the three first levels of the bed, with a spatial resolution of 1 cm.

Results

Records of wind speed provided by the Cap-Ferret Weather Station during the sampling period give evidence of six windy episodes associated with Atlantic western low pressures. For each of these periods, the mean wind speed (hourly averaged) is higher than 10 m s^{-1}. The winds generate waves between 10 and 45 cm high. The most intense episode was recorded on 8 December 2006, with wind speed of 20 m s^{-1} and significant height of wind waves (*Hsig*) of more than 30 cm. Figure 1 shows a typical record during two consecutive tidal cycles on 8 December. Wave parameters (period *T* and *Hsig*) increase together with the tidal level. This is probably due to a larger fetch when intertidal areas are flooded. Maximum wave height is reached at high tide (between 30 and 40 cm at Station 04 in the inner lagoon).

Bed level records show regular but weak remobilization due to tidal currents regulated by semi-diurnal tidal cycle. During the wind event, there is a clear erosion pattern, with the bed deepening of at least 10 mm in one tidal cycle. Figure 2 shows erosion pattern in three stations during the wind episode of 8 December 2006. In all stations, wind waves reach a similar significant height, around 50 cm during the two tidal cycles. However, the bed response is different following the type of sediment. Stations 04 and 03, more silty and consolidated, experience erosion of 1 cm only during the second tidal cycle. It is suggested that during the first tidal cycle, wave induced shear stress is not enough to generate resuspension, but it can contribute to the fluidization of the bed in the first cm, getting the surficial sediment easily erodible for the second tidal cycle. In Station 02, with high sand content and less consolidated, erosion starts before the energetic episode, under wind waves of 20 to 25 cm. After the two windy tidal cycles, the total erosion thickness is about 3 cm. Here, liquefaction is not necessary to generate erosion, and the sediment is supposed to be erodible in depth.

Erosion of the bed contributes significantly to the increase of suspended sediment concentration in the lagoon waters. Figure 3 illustrates a situation at Le Teich tidal flat (station 04) during a fortnightly tidal cycle. The effect of currents on resuspension is weak, with concentration lower than 50 mg l^{-1}. The development of wind waves on the surface of the lagoon after the spring tides generates significant bottom shear stress, ten times greater than bottom shear stress due to currents alone. Subsequent sediment erosion is also significant, and concentrations values can reach 250 mg l^{-1}. As suggested by Le Hir et al. (2000), maximum erosion occurs at high water slack, when wind waves are the most energetic, which contributes to the depletion of the tidal flat and the transfer of sediment towards the channel during ebb. It can be seen from the Altus probe record (lower panel) that erosion is effective during the windy episode, but in the absence of wind waves, the predominance of tidal currents promotes accretion of the tidal flat. At the end of the record, the bed level recovered its initial value.

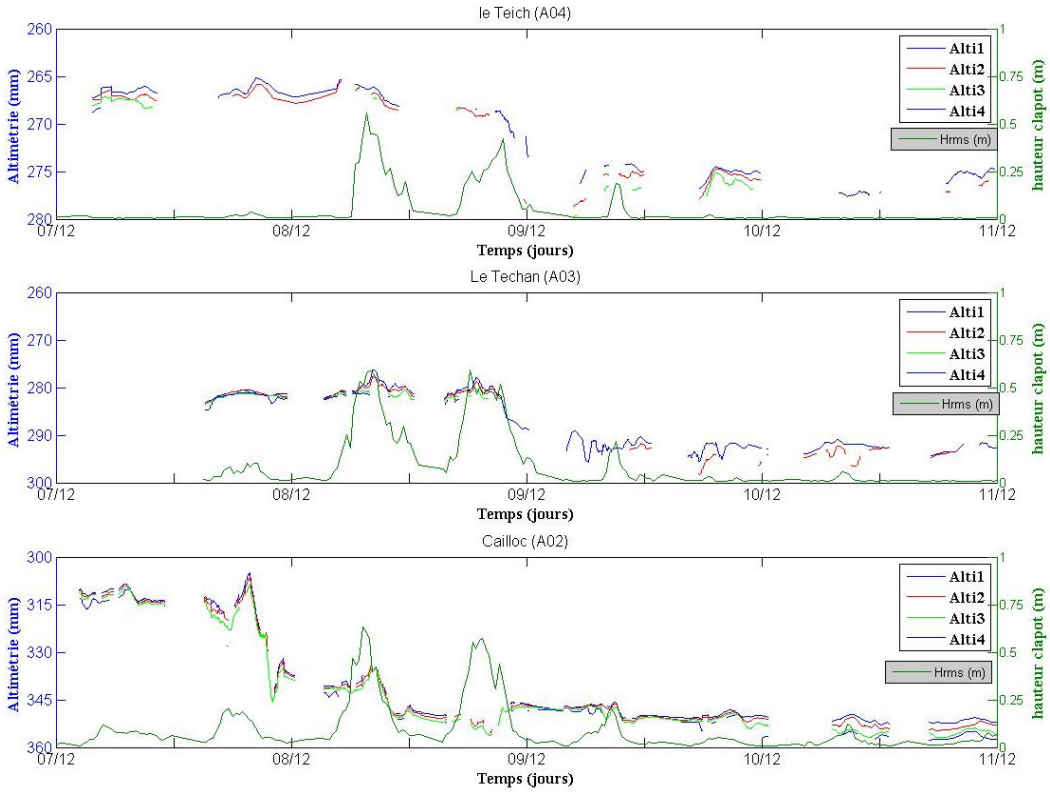

Figure 2. Record of bed level (left axis) and wind wave height *Hrms* (right axis) for three Altus stations in the Arcachon lagoon

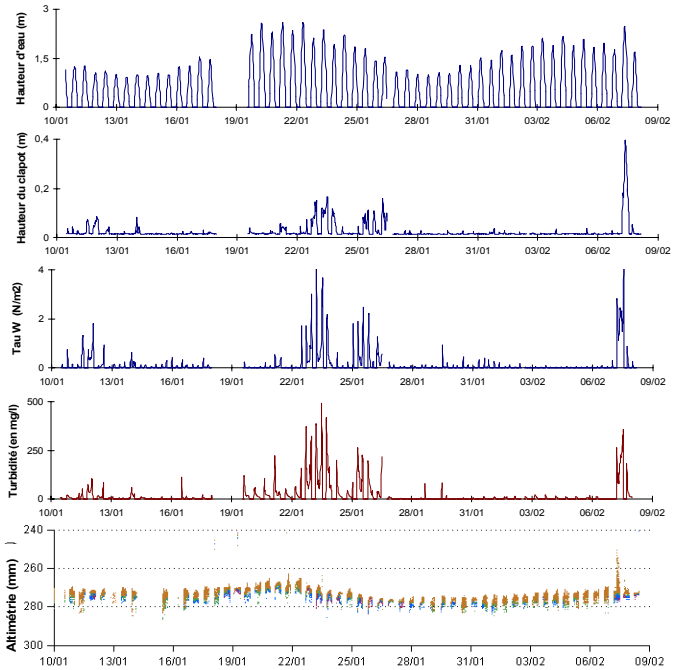

Figure 3. Series of record at Station 04 (Le Teich tidal flat, inner lagoon): (a) water level, (b) significant wave height *Hsig* of waves measured by the Altus, (c) bottom shear stress induced by waves, computed from Altus records, (d) suspended sediment concentration measured by a calibrated OBS turbidimeter (e) Bed level measured by the Altus turbidimeter.

Conclusions

This first series of fine record of wind waves and sediment dynamics in the Arcachon lagoon show that windy episodes generate enough wind waves to trigger bed remobilization and to increase water turbidity significantly. The wind waves are essentially generated by winds associated to Atlantic western low pressures. They propagate form west to east, and they are sensitive to tidal level, which favors larger fetch during high water. In terms of sedimentary balance, the erosive action of wind waves tends to equilibrate accretion trends forced by tidal currents. Erosion thickness is closely dependent on sediment properties and consolidation state. Sediment transport modeling must account for wind wave action, at least for a better estimation of bottom shear stress.

References

Bassoullet, Ph., Le Hir, P., Gouleau, D., Robert, S. (2000), Sediment transport over an intertidal mudflat: field investigations and estimation of fluxes within the 'Baie de Marennes-Oléron' (France), *Continental Shelf Research*, 20(12–13), 1635–1653.

Janssen-Stelder, B. (2000), The effect of different hydrodynamic conditions on the morphodynamics of a tidal mudflat in the Dutch Wadden Sea, *Continental Shelf Research*, 20(12–13), 1461–1478.

Le Hir, P, Roberts, W., Cazaillet, O., Christie, M., Bassoullet, P., Bacher, C. (2000), Characterization of intertidal flat hydrodynamics, *Continental Shelf Research*, 20(12–13), 1433–1459.

Shi, Z., Chen, J.Y. (1996), Morphodynamics and sediment dynamics on intertidal mudflats in China (1961–1994), *Continental Shelf Research*, 16 (15), 1909–1926.

Verney, R., Deloffre, J., Brun-Cottan, J.-C., Lafite, R. (2007), The effect of wave-induced turbulence on intertidal mudflats: Impact of boat traffic and wind, *Continental Shelf Research*, 27(5), 594–612.

Observations of the effects of turbulence on particle size distributions in an estuarine bottom boundary layer

WILL THURSTON[1], ALEJANDRO J. SOUZA[2], MARK PRITCHARD[3]

1. Institute for Atmospheric Science, School of Earth and Environment, University of Leeds, Leeds LS2 9JT UK
email: w.thurston@see.leeds.ac.uk

2. Proudman Oceanographic Laboratory, 6 Brownlow Street, Liverpool L3 5DA UK
email: ajso@pol.ac.uk

3. National Institute of Water and Atmospheric Research, P.O. Box 11-115, Hamilton 3521, New Zealand
email: m.pritchard@niwa.co.nz

Keywords: turbulence, SPM, flocculation

ABSTRACT

Here we present continuous, concurrent observations of dynamics and suspended particulate matter (SPM), performed in the bottom boundary layer (bbl) of a macrotidal estuary during a 24-day period. Turbulence parameters were found to vary on both a quarter-diurnal and a spring-neap tidal timescales. An approximate local balance between the shear production and dissipation of turbulent kinetic energy (TKE) was also found. The concentration of SPM in the bbl varied on similar timescales, but diurnal and synoptic scale variations were also found to be important. The size distribution of SPM observed is strongly linked to the Kolmogorov microscale and turbulent shear rate, suggesting that turbulence is playing a significant role in regulating the extent of SPM flocculation.

Introduction

The bottom boundary layer (bbl) of an estuary is an important and dynamically interesting area of study for physical oceanographers. It is here that the maximum levels of turbulence can be found, due to high stress and shear rates. A local balance should exist in the bbl between the production of TKE by shear and buoyancy and the viscous dissipation of TKE at the microscale. Erosion and deposition of SPM also occurs within the bbl, the rate of which is determined by the intensity of the turbulence experienced. In the case of cohesive SPM, turbulence also plays a role in determining the level of flocculation in addition to controlling the vertical flux. This flocculation itself has an effect on erosion/deposition, by modifying the size of SPM by up to one order of magnitude, e.g., Mikkelsen et al. (2007), changing its settling velocity.

There is an increasing use of prognostic numerical models, e.g., POLCOMS (Holt and James, 2001), coupled to ecosystem models, e.g., ERSEM (Baretta-Bekker et al., 1997), as a tool for water quality and pollutant transport forecasting in the shelf seas. In order to accurately predict the spatial distribution of a pollutant, the spatial distribution of SPM needs to be known, due to adsorption of pollutants onto the SPM surface. Knowledge of SPM dynamics is also sought after due to the important role SPM plays in biogeochemical cycling and primary productivity (Tett et al., 1993). Ultimately, the spatial distribution of SPM in the coastal zone is controlled by the vertical flux between the bed and the water column, as this determines the amount of material available for advection by the mean flow. The ability to model turbulence-SPM interactions in the bbl is therefore vital for accurate pollutant transport and water quality modeling. This is by no means an easy task, but one which can be aided by the collection of high quality observations of turbulence-SPM interactions. It is our aim to collect and analyze such a dataset which can be used to test, validate and improve the parameterizations which represent these processes in numerical models.

Methods

The observations presented here were performed in the Dee estuary, presented in Figure 1. The Dee is situated in between northeast Wales and northwest England and opens out into Liverpool Bay and the Irish Sea. Tidal forcing in the Dee is particularly strong, with a range in excess of 9 m and surface currents of 1.5 m s^{-1} experienced on spring tides. The tidal form is dominated by the M_2 and S_2 constituents, although shallow water overtides are also observed. Runoff from the 1816 km^2 catchment area supplies the estuary with freshwater at an annual average rate of 37 $m^3 s^{-1}$. Seasonal variation in this runoff rate is smoothed out to some extent by the Environment Agency's 'Dee extraction scheme', which stores water during the winter months in order to provide a sufficient supply during the summer for extraction and to prevent salt intruding upstream of Chester. Interaction between the tidal forcing and freshwater induced horizontal density gradient leads to an estuarine circulation and a cycle of periodic stratification. High concentrations of cohesive SPM are also found in the Dee, the dynamics of which make the estuary a morphologically complex site.

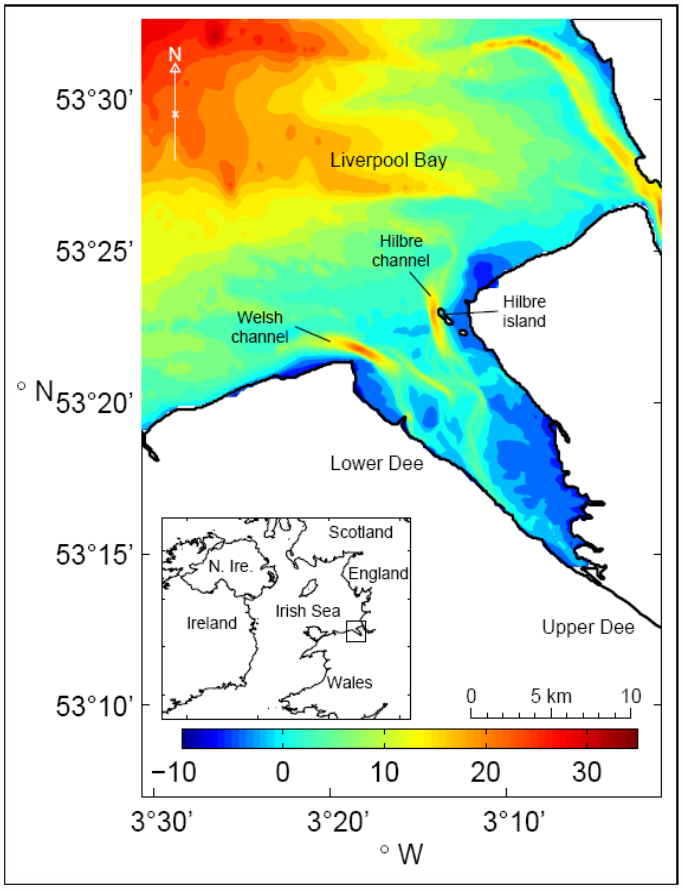

Figure 1. Bathymetry and location of the Dee Estuary.

The lower estuary narrows in a funnel like manner, from a width of 8 km at the mouth to a width of 100 m, over an axial distance of 20 km. From this point the lower estuary takes the form of a quasi-uniform channel which extends 15 km to the tidal limit at Chester weir. Two channels, the Welsh Channel and the Hilbre Channel, face each other across the mouth of the Dee. Both are approximately 20 m deep, 1 km wide and 4 km long.

A STABLE (sediment transport and boundary layer experiment) mooring was deployed in the Hilbre Channel, from the RV Prince Madog, for a 24-day period from 8 February 2006. The STABLE contained a LISST-100C, an acoustic backscatter system a sediment trap and three SonTek ADVs (mounted at 0.3, 0.6 and 0.9 m above the bed). A second mooring, containing a 1200 kHz RDI ADCP, was also deployed in the Hilbre Channel to observe dynamics throughout the water column in conjunction with CTD casts performed. Here we present some preliminary results from the ADV and LISST instruments, which were programmed to record a 20-minute observation burst once every hour for the duration of the observation period.

Results

In preparation for calculation of turbulence parameters, the ADV velocity bursts were first despiked using the Goring and Nikora (2002) velocity phase-space method. Then the velocity data was orientated along-channel by rotating to minimize the cross-channel variance over the 24-day observation period. Finally, the velocity data was rotated to minimize the vertical velocity over the observation period. Shear production of TKE, P (W m^{-3}), was calculated from

$$P = -\rho\left(u'w'\frac{\partial u}{\partial z} + v'w'\frac{\partial v}{\partial z}\right) \quad (1)$$

where the velocity covariances were calculated directly for each burst and the shear calculated assuming a log profile for velocity. The dissipation rate of TKE, ε (W m^{-3}), was calculated for each burst from the vertical velocity spectrum

$$E(k) = \alpha \varepsilon^{2/3} k^{-5/3} . \quad (2)$$

The variation of shear production and dissipation of TKE over the observation period, from the ADV mounted at 0.9 m above the bed, is presented in Figure 2. The dominant mode of variability of TKE production is at the quarter-diurnal frequency, due to maximum production rate coinciding with maximum flood and ebb currents. In addition, there is also a clear spring neap cycle in TKE production rates; during spring tides the maximum observed TKE production rates are over one order of magnitude greater than the observed maxima during neap tides. In general these results are in good agreement with the TKE production rates observed by the lowest bin of the ADCP. Comparing production and dissipation rates reveals that there is an approximate local balance in terms of the shape of the curve, but dissipation appears to be consistently higher than production. This inconsistency is emphasized during neap tides and slack waters.

The total SPM concentration (µl l^{-1}), summed over all size bands 2.5–500 µm, is presented in Figure 3a. Quarter-diurnal variability is observed, due to resuspension of SPM at high levels of TKE. A semi-diurnal signal is also evident; SPM concentration is generally higher on flood tide. There is similar variability in the median particle size, which is largest during the quiescent conditions of slack water and smallest during maximum flood/ebb. Larger flocs are observed at low water slack than at high water slack.

There is a less pronounced spring-neap cycle in the SPM properties than is observed in the TKE production and dissipation rates. This is due to synoptic events, such as wind and river runoff, playing an important role.

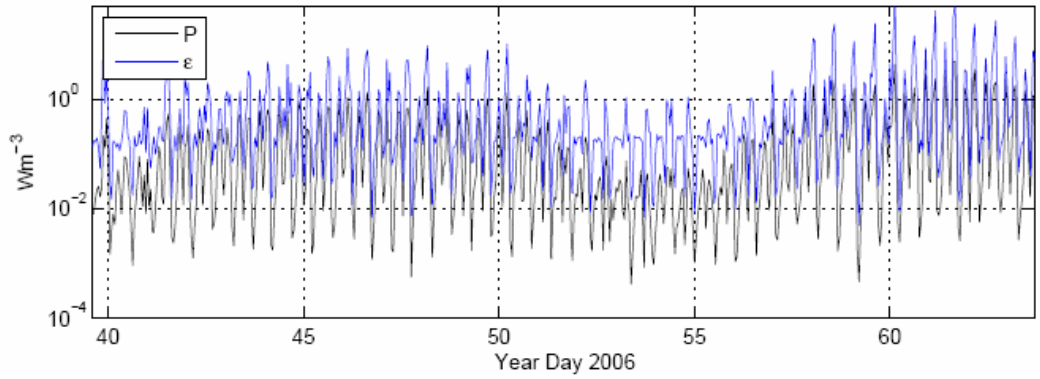

Figure 2. Timeseries of TKE production rate, P, and dissipation rate, ε (W m^{-3}) during the 24-day observation period.

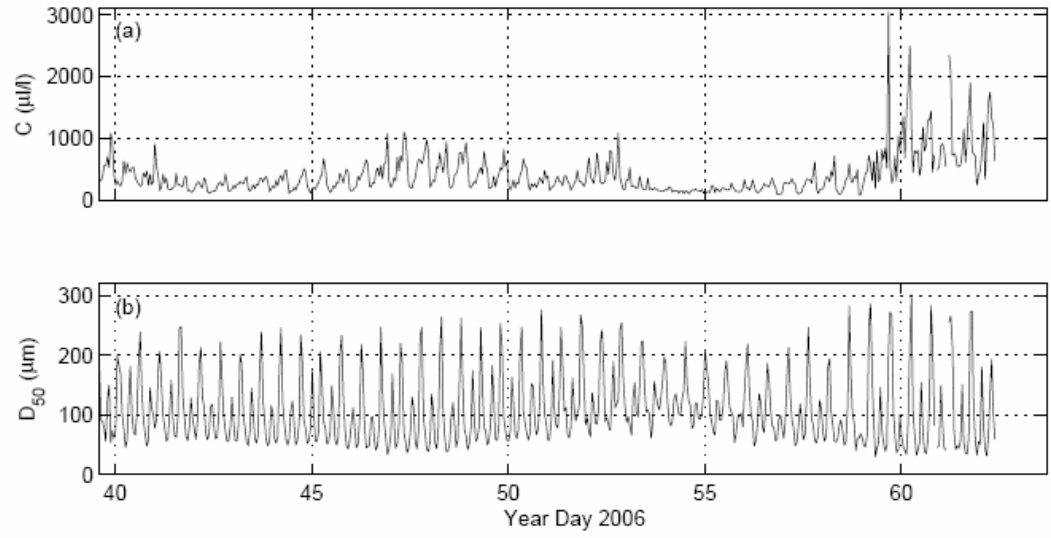

Figure 3. Timeseries of (a) the total SPM concentration, µl l^{-1} and (b) the median particle size D_{50}, µm during the 24-day observation period.

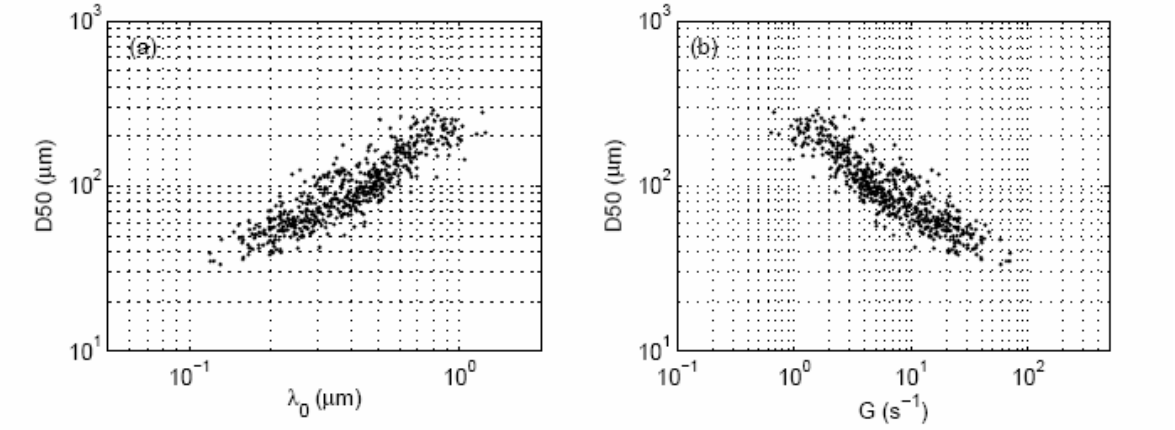

Figure 4. Comparison of the median particle size D_{50}, µm to (a) the Kolmogorov microscale, µm, and (b) the turbulent shear rate, s^{-1}.

Following Fugate and Friedrichs (2003) we consider the the Kolmogorov microscale, λ_K, and the turbulent shear rate, G, in an attempt to quantify the effects of turbulence on floc size

$$\lambda_K = \left(\frac{\upsilon^3}{\varepsilon}\right)^{1/4} \qquad G = \left(\frac{\varepsilon}{\upsilon}\right)^{1/2}. \tag{3, 4}$$

At present for these calculations we have assumed a local balance and substituted TKE production for dissipation because we have greater confidence in the accuracy of the TKE production results. Comparing G and λ_K to D_{50}, Figure 4, reveals a very strong relationship between turbulence and particle size. As λ_K increases, the size of floc that an eddy can enter and break up increases, increasing the median floc size. Similarly as the turbulent shear rate increases, more and more flocs are broken up, reducing D_{50}.

Conclusions

Concurrent observations from an estuarine bbl have revealed that both turbulence and SPM vary over timescales ranging from quarter-diurnal to spring-neap. A qualitative local balance between production and dissipation of TKE was also found. SPM concentration was generally found to be higher on flood tides than ebb tides and floc size was larger at low water slack than high water slack. The size distribution of SPM observed is strongly linked to the Kolmogorov microscale and turbulent shear rate, suggesting that turbulence is playing a significant role in regulating the extent of SPM flocculation.

References

Baretta-Bekker, J.G., Baretta, J.W., Ebenhöh, W. (1997), Microbial dynamics in the marine ecosystem model ERSEM II with decoupled carbon assimilation and nutrient uptake, *Journal of Sea Research*, 38, 195–211.

Fugate, D.C., Friedrichs, C.T. (2003), Controls on suspended aggregate size in partially mixed estuaries, *Estuarine, Coastal Shelf Science*, 58, 389–404.

Goring, D.G., Nikora, V.I. (2002), Despiking acoustic Doppler velocimeter data, *Journal of Hydraulic Engineering*, 128, 117–126.

Holt, J.T., James, I.D. (2001), An *s*-coordinate density evolving model of the northwest European continental shelf, *Journal of Geophysical Research*, 106, 14015–14034.

Mikkelsen, O.A., Hilla, P.S., Milligan, T.G. (2007), Seasonal and spatial variation of floc size, settling velocity, and density on the inner Adriatic Shelf (Italy), *Continental Shelf Research*, 27, 417–430, doi:10.1016/j.csr.2006.11.004.

Tett, P.B., Joint, I.R., Purdie, D.A., Baars, M., Oosterhuis, S., Daneri, G., Hannah, F., Mills, D.K., Plummer, D., Pomroy, A.J., Walne, A.W., Witte, H.J., Howarth, M.J., Lankester, R. (1993), Biological consequences of tidal stirring gradients in the North Sea, *Philosophical Transactions of the Royal Society of London*, *A*, 343, 493–508.

Hydrodynamics and sediment dynamics in a small muddy macrotidal estuary (Penzé Estuary, NW France): From monitoring to modeling

ROMARIC VERNEY[1], PHILIPPE BASSOULLET[1], PIERRE LE HIR[1],
HERVÉ JESTIN[1], MARC SOURISSEAU[2]

1. IFREMER Centre de Brest, Dyneco-Physed, BP 70, 29280 Plouzané, France
2. IFREMER Centre de Brest, Dyneco-Pelagos, BP 70, 29280 Plouzané, France
email: rverney@ifremer.fr, philippe.bassoullet@ifremer.fr,
pierre.le.hir@ifremer.fr, marc.sourisseau@ifremer.fr

Keywords: hydrodynamics, sedimentation and erosion processes, estuarine dynamics, 3-D numerical model

ABSTRACT

The Penzé estuary is located on the north coast of Brittany (France), where shellfish farming activity is seasonally confronted with harmful algal blooms. The Penzé is a small macrotidal, meandering, deeply embanked muddy estuary, seasonally influenced by freshwater inflows (Figure 1). This study investigates hydrodynamics and sediment dynamics in the Penzé estuary from field observations and 3-D numerical modeling. Once validated, this model will be coupled to an ecological model to simulate toxic algal blooms.

Monitoring strategy

The paper reports in situ measurements in the estuary: vertical stratification, estuarine turbidity maximum dynamics and erosion/deposition processes at several stations. Different field campaigns were realized in the Penzé estuary: i) longitudinal and fixed point measurement profiles (CTD + turbidity) in March (neap tide, high river discharge), April (spring tide, high river discharge) and June (low tide, low river discharge) 2001; ii) short term (two months) current and turbidity measurements in winter 2001–2002 and summer 2005; iii) long term bed level monitoring (ALTUS system) April 2001 to April 2002 on six intertidal mudbanks.

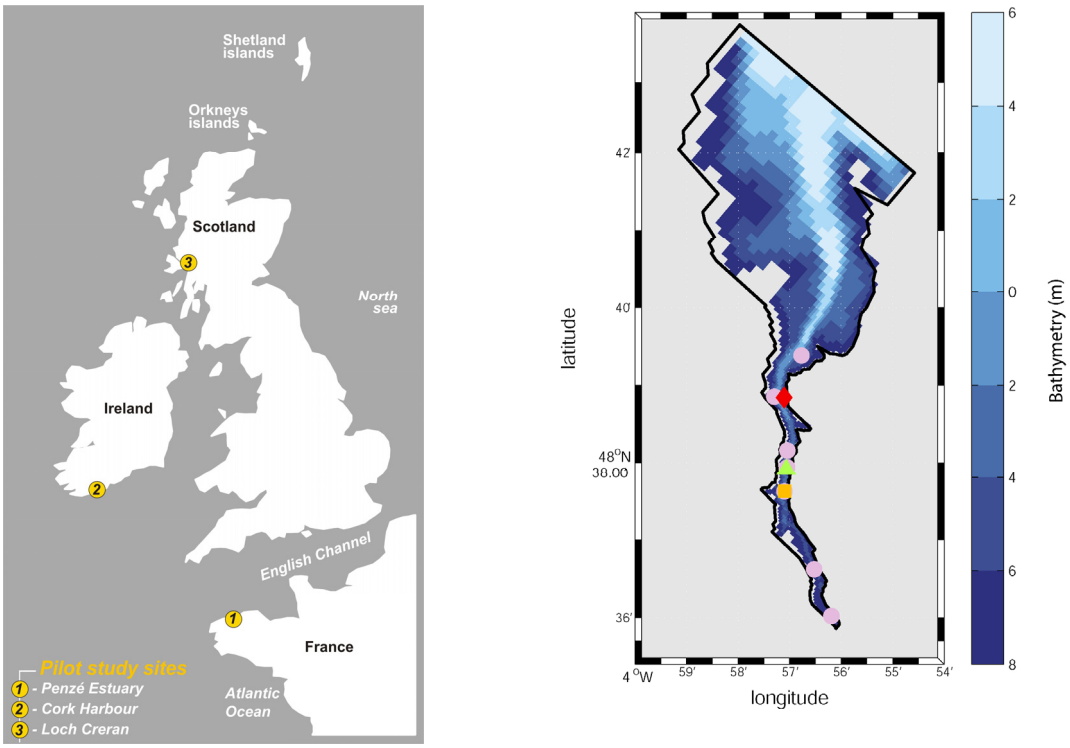

Figure 1. Left: Penzé estuary location. Right: numerical model bathymetry and survey sites – ● ALTUS stations, ■ SAMPLE station, ▲ multi-parameter probe, ♦ fixed station for profiling measurements.

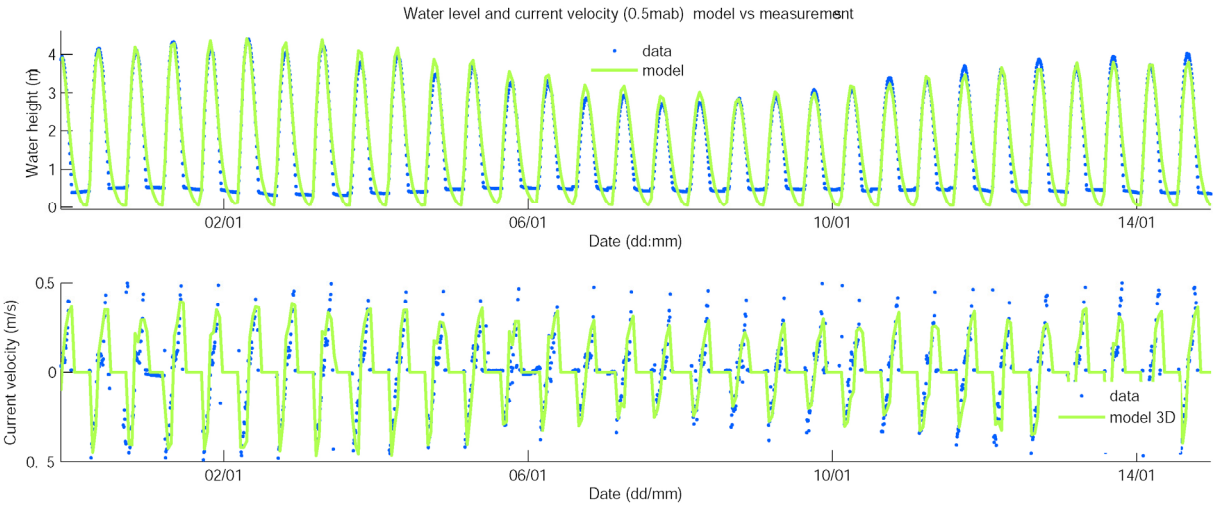

Figure 2. Current velocity in the upstream part of the Penzé estuary: model (green line) and measurements (blue dots).

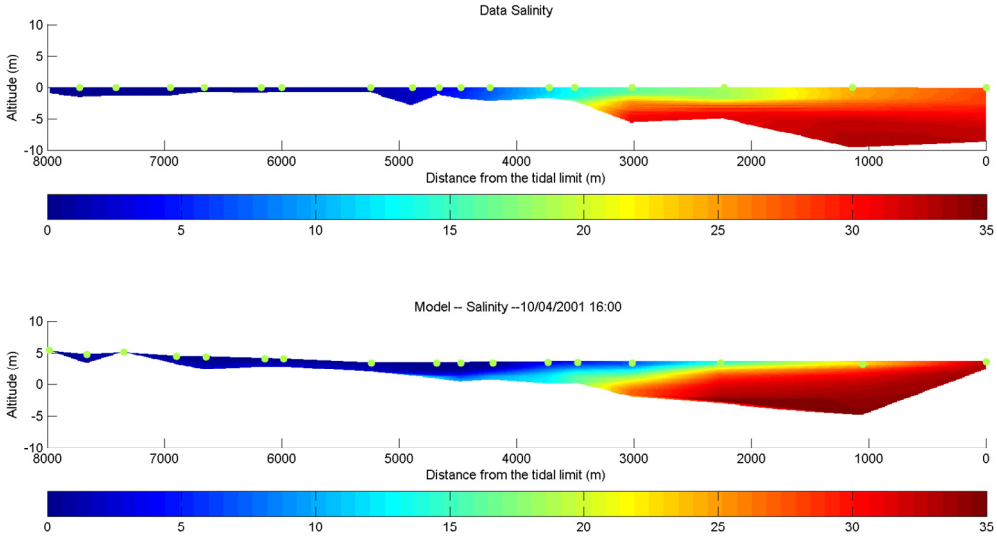

Figure 3. Salinity longitudinal profiles: measurements (upper), model (lower) on 4 October 2001: spring tide, high river discharge.

Model description

The S*i*AM-3D numerical model combines hydrodynamic and sediment transport models. The hydrodynamic module solves the Navier-Stokes equations (shallow water) assuming hydrostatic hypothesis and Boussinesq approximation. The model computes separately external (depth averaged) and internal (3-D computation) modes for CPU time optimization (for a complete description of the model see Cugier and Le Hir, 2002). S*i*AM-3D is based on a mixing length turbulence closure scheme, which account for turbulence damping due to stratification through a local gradient Richardson number (Lehfeld and Bloss, 1988). The sediment transport model is based on an advection/diffusion model and transports mud, temperature and salinity as well as other dissolved species (nutrient, contaminants) and pelagic variables like phytoplankton species used in the ecological model. The sediment compartment is discretized in thin layers that are dynamically created or deleted as a function of sediment concentration, bed erosion or deposition. Deposition and erosion processes are calculated from the Krone and Partheniades formulations respectively (Le Hir et al., 2001). Erosion is controlled by the bed shear stress while deposition is always allowed. Similarly to the sediment compartment, the water column is discretized in ten σ-coordinates layers of equal thickness to improve simulation of density gradients and then stratification.

The Penzé estuary is a strongly muddy estuary, with a wide mouth progressively narrowing upstream up to the inner part of the estuary. The upper estuary is featured by large and steep sloping lateral intertidal mudbanks beside the main channel. In this area during the highest spring tides, the main channel section at

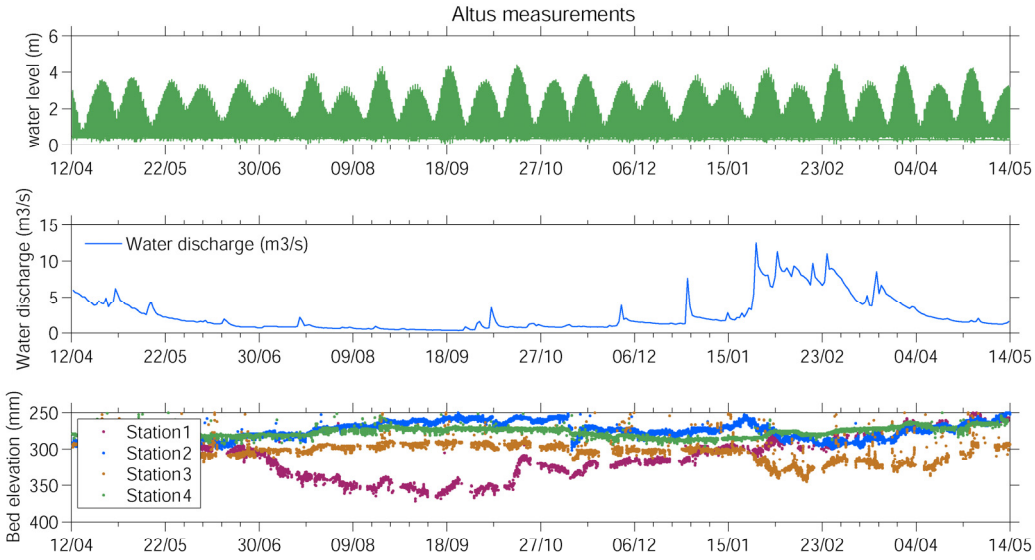

Figure 4. Tidal amplitude (upper panel), river discharge (middle panel) and bed level monitoring (lower panel) from spring 2001 to spring 2002. Station 1 is the most upstream and next stations follow downstream.

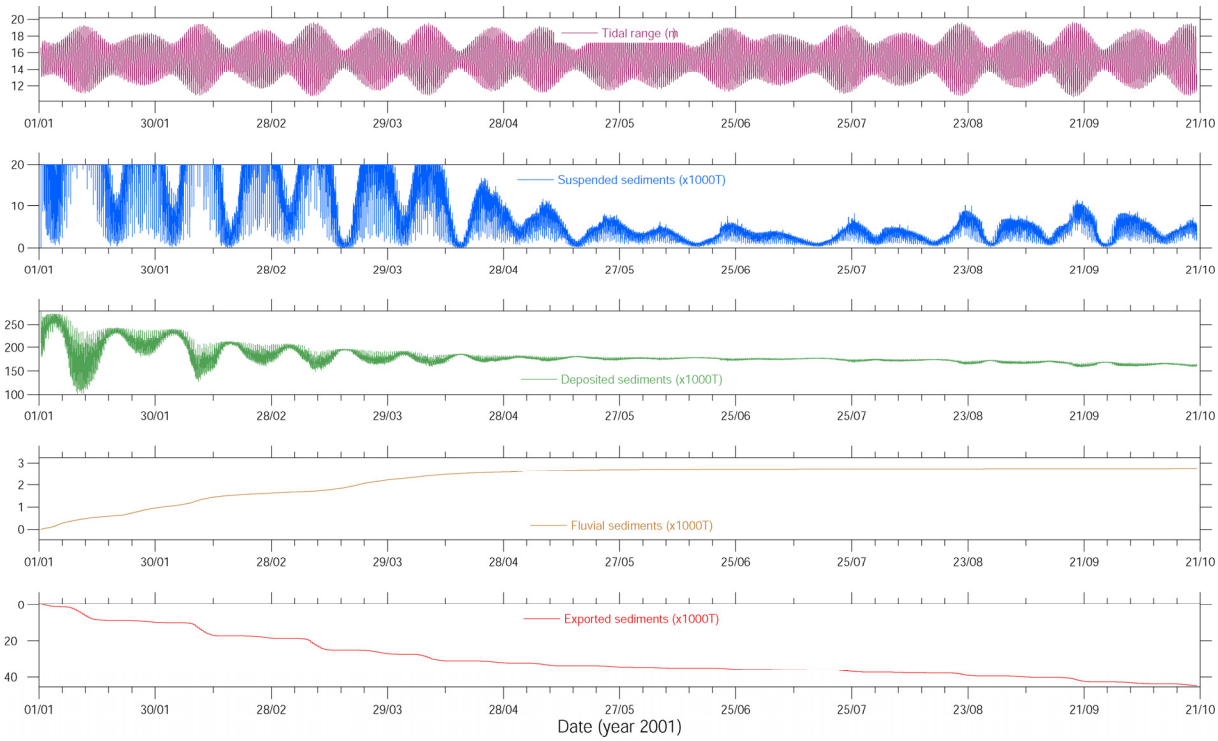

Figure 5. Sediment budget in the whole estuary simulated during ten months in 2001: tidal elevation, mass of sediment in suspension, deposited sediment, exported sediment and fluvial sediment brought by the Penzé River.

low tide can be as thinner as a few meters. Therefore irregular grid spacing was adopted to optimize model performances for simulating small scales processes and conform to the bathymetry, with refined grid spacing in the upper estuary (50 m) and larger spacing at the sea boundary (200 m) (Figure 1).

Results

Tidal amplitude and tidal currents are well reproduced by the model all along the fortnightly cycle, with strongest flood during spring tides, up to 0.5 m s^{-1} (Figure 2). Few discrepancies were observed at the end of ebb tides, where the model tends to simulate lower currents than those observed. Salinity and temperature profiles show strong stratification patterns during high river discharge with salinity gradients from 5 to 30 in

two meters below the surface all along the estuary and stronger during neap tide (Figure 3). This stratification pattern is correctly reproduced by the model, with similar depth variations, excepted during neap tides in conjunction with high river discharge.

SPM longitudinal measurements as well as short term fixed measurements show the presence of an estuarine turbidity maximum moving up to the tidal limit during spring tides. The largest near-bed concentrations were measured over 3 g l^{-1}. The most upstream part of the estuary (station 1) is mainly influenced by spring tides, when the ETM is moving up to the tidal limit (Figure 4). Also no effects are observed during high river discharge, while this event caused strong erosions downstream (stations 2 and 3). These erosion events are correlated to deposition further downstream (station 4).

S*i*AM3D is shown to correctly simulate suspended matter concentration and the turbidity maximum dynamics. Results show a relative fair agreement with bed level monitoring, with a strong control of tides, river discharge. However, some sedimentation or erosion episodes may be missed. The apparent difficulty in simulating local sedimentation dynamics is mainly due to the morphology of the estuary, i.e., steep muddy embankments, still not well reproduced by the model despite a rather high spatial resolution.

In terms of sediment budget within the estuary, up to 10,000 tonnes of sediment are resuspended during the highest spring tides, constituting a turbidity maximum area (Figure 5). These sediments are mainly deposited during neap tides (mass in suspension below 1000 tonnes). Most of the turbidity in the estuary is due to resuspension as few suspended sediment entered the estuary at the upstream tidal limit (below 3000 tonnes in ten months).

References

Cugier, P., Le Hir, P. (2002), Development of a 3-D hydrodynamic model for coastal ecosystem modelling. Application to the plume of the Seine River (France), *Estuarine, Coastal and Shelf Science*, 55, 673–695.

Lehfeld, R., Bloss, S. (1988), *Algebraic turbulence model for stratified tidal flows*. In: Physical Processes in Estuaries, Donkers, J., van Leussen, W. (Eds.),Springer-Verlag, New York, pp. 278–291.

Le Hir, P., Ficht, A., Silva Jacinto, R., Lesueur, P., Dupont, J.-P., Lafite, R., Brenon, I., Thouvenin, B. Cugier, P. (2001), Fine sediment transport and accumulations at the mouth of the Seine Estuary (France), *Estuaries*, 24(6B), 950–963.

Estuarine turbidity maximum dynamics in the outer Weser Estuary for different runoffs including a river flood

IRIS GRABEMANN

Institute for Coastal Research, GKSS Research Centre, Max-Planck-Straße 1,
21502 Geesthacht, Germany
email: iris.grabemann@gkss.de

Keywords: SPM dynamics, river flood, estuary

ABSTRACT

Introduction and database

In the Weser estuary (Germany) the estuarine turbidity maximum (ETM) is generally found in the lower salinity region of the mixing zone. The positions of mixing zone and ETM vary with freshwater runoff. Near-bottom time series measurements between 1983 and 1997 (source: Alfred-Wegener-Institut für Polar- und Meeresforschung (AWI), Bremerhaven) provided insight into the suspended particulate matter (SPM) dynamics on different time scales. These measurements included long-term recordings with long gaps in the order of months and years at the site BL (Figure 1) in the inner part of the estuary and sparse recordings of weekly to monthly duration at a few other sites. The measurements at BL comprise freshwater runoffs from about 100 to 2000 $m^3 s^{-1}$ and the sparse measurements were performed during low to moderate runoff conditions. They displayed that the ETM is flushed towards the outer estuary during river floods together with the mixing zone. For runoffs greater than 1000 $m^3 s^{-1}$ (the long-term mean runoff is about 325 $m^3 s^{-1}$) generally no ETM is observed in the inner estuary at BL. The mixing zone returns simultaneously with decreasing runoff and the salinity levels at a fixed site show nearly no hysteresis before and after river floods. If the floods and their decreasing parts occur during times of relatively low mean water levels, a hysteresis in SPM levels can be observed which may result from a lagging re-establishment of the ETM. In the case of relatively high mean water levels, the ETM seems to be maintained in the outer estuary (Grabemann and Krause, 2001). For the fate of the ETM in the outer Weser estuary during river floods, assumptions only could be derived from the above-mentioned measurements.

In the course of the last years, recurring SPM (turbidity) measurements of weekly to monthly duration were performed at different sites in the inner and outer estuary (Figure 1) by the Wasser- und Schifffahrtsamt (WSA) Bremerhaven (Waterway Authority). The recordings in the outer estuary contain a river flood. Salinity (conductivity) and current velocity also were measured. Daily values of the freshwater runoff recorded about 30 km upstream of Bremen and the heights of tidal high and low water recorded at km 66.7 were taken from annual manuals (Deutsches Gewässerkundliche Jahrbuch, Weser und Emsgebiet).

The aim of this study is to investigate the SPM dynamics in the outer estuary by using the WSA measurements and to gain insight into the fate of the ETM in the outer estuary under river flood conditions. The dynamics in the inner and outer estuary will be compared and differences will be discussed.

Results

The positions of mixing zone and ETM vary according to runoff variations. Thus, a fixed site can be in the central part or in the margins of the ETM or up- or downstream of this feature. In the ETM region the strong intratidal SPM variability can be explained as the result of a circular process consisting of deposition over slack water periods, subsequent re-suspension and depletion of temporarily-formed deposits and upstream and downstream transport by tidal currents. Characteristic intratidal SPM patterns can be specified for each ETM part. Empirical relationships between runoff, salinity and the characteristic intratidal SPM patterns known from earlier investigations (e.g., Grabemann and Krause, 2001) have been complemented using the WSA measurements and are used as indicators to determine the positions of mixing zone and ETM relative to a site. In the following, salinity and concentration values are averages over the given runoff intervals.

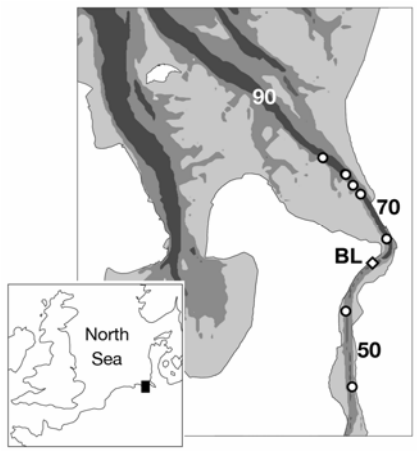

Figure 1. Map of the Weser estuary. The numbers give the official kilometer scale which starts at km 0 in Bremen. The weir 5 km upstream of km 0 is the landward boundary of the estuary. The dots present the locations of the WSA measurements and the rectangle shows the location of the site BL.

For runoffs of 200–300 $m^3 s^{-1}$ measurements at km 46.6, km 55.8 and km 66.7 were conducted simultaneously. For such runoffs the lower-salinity region of the mixing zone occupies the inner estuary and the tidally averaged near-bottom salinity is about 1.2, 5 and 13, respectively, at these sites. At km 46.6 SPM concentration peaks occur in the second half of the flood and the first half of the ebb tide showing that the site is in the landward part of the ETM. At km 55.8 the concentration peaks are somewhat broader; this site is in the proximity of the central part. At km 66.7 the concentration peaks occur during the first half of the flood and the second half of the ebb tide which is the characteristic pattern for the seaward part of the ETM. The ETM is located in the inner estuary – as expected – and it seems to be centered at about km 60.

Non-simultaneous measurements at the site BL and the sites at km 73.1 and 79.5 were linked by using the above-mentioned empirical relationships and the runoff. The intratidal SPM patterns show that BL is located in the central-seaward part of the ETM for runoffs of 200–300 $m^3 s^{-1}$ and the tidally averaged near-bottom salinity is about 7 which correspond to the above-mentioned findings. Towards the end of the ebb tide, higher turbidity also occurs at km 73.1 in the outer estuary and somewhat later and less high at km 79.5 and vanishes at the beginning of the flood tide; the seaward tail of the ETM seems to reach these sites. The peak concentrations are smaller by factors of about 2.4 and 3, respectively, than the peak concentration at km 55.8. Both sites are located in this case in the higher-salinity region of the mixing zone; the tidally averaged near-bottom salinity is about 17 and 21, respectively. The measurements at km 73.1 and 79.5 suggest that the longitudinal ETM extension during lower and moderate runoff conditions seems to be further seaward than expected so far.

During the peak and the decreasing part of a river flood simultaneous measurements were performed at km 66.7, km 74.6 and km 76.2. During these measurements the runoff exceeds 1100 $m^3 s^{-1}$ and the mean water levels are comparatively high. For runoffs of 1200–1600 $m^3 s^{-1}$ the lower salinity reaches are located in the outer estuary and the tidally averaged near-bottom salinity is about 3, 9 and 12, respectively. The mean intratidal SPM concentrations are in the same order of magnitude as those found at km 55.8 and km 66.7 during lower to moderate runoffs. The three sites show the intratidal SPM patterns which are consistent with those in the landward, the central-seaward and the seaward part of the ETM showing that an ETM exists in this part of the outer estuary during this river flood. Furthermore, the intratidal SPM behavior seems to be similar to that found in the inner estuary for smaller runoffs.

The results presented for this river flood are in agreement with the assumption by Grabemann and Krause (2001), notably, that the ETM is maintained in the outer estuary in the case of the coincidence of a river flood and higher mean water levels.

Nevertheless, this ETM in the outer estuary as well as the mixing zone seem to have a comparatively smaller longitudinal extension; they seem to be ‘compressed’. SPM behavior and the part of the mixing zone with mean salinities from about 1 to about 13, which are widespread over about 20 km in the inner estuary for smaller runoffs, are extended over approximately 15 km in the outer estuary for river flood conditions and higher mean water levels (then the tidally averaged salinity at BL would be about 1).

Acknowledgements

The author thanks the Wasser- und Schifffahrtsamt (WSA) Bremerhaven and the Alfred-Wegener-Institute für Polar- und Meeresforschung (AWI) for providing data.

References

Deutsches Gewässerkundliches Jahrbuch, Weser und Emsgebiet (various years), Niedersächsisches Landesamt für Ökologie (Ed.), Hildesheim, Germany.

Grabemann, I., Krause, G. (2001), On different time scales of suspended matter dynamics in the Weser estuary, *Estuaries*, 24(5), 688–698.

Suspended sediment mineralogical signature – an approach to understand shelf water hydrodynamics

ANABELA T.C. OLIVEIRA, ANA ISABEL O. SANTOS, ALEXANDRA H. MORGADO, ANTÓNIO JORGE DA SILVA

Marinha-Instituto Hidrográfico, Rua das Trinas 49, 1249-093 Lisboa, Portugal
email: anabela.oliveira@hidrografico.pt, ana.santos@hidrografico.pt, alexandra.morgado@hidrografico.pt, jorge.silva@hidrografico.pt

Keywords: mineralogy, rivers, suspended sediment, buoyancy coastal current

ABSTRACT

The northern Portuguese-Galician shelf current system is under study in the framework of the NICC (Northwest Iberian coastal current) project. This project seeks to understand if river runoff can induce a buoyancy driven coastal current capable of promoting an effective northward transport of water, sediments and biological material from both shelf and estuarine sources. In this study we use the mineralogy of suspended fine sediments as tracers of river runoff. Data were obtained in February/March 2006, for a better comprehension of winter shelf dynamics.

Introduction

The current system in the northern part of the west Iberian shelf is not yet well understood and existing models fail to describe it adequately, especially in extreme conditions (Silva et al., 2008). In this area, active and persistent coastal upwelling conditions prevail from June to September (e.g., Wooster et al., 1976). In wintertime (October to January) the wind regime favors downwelling (e.g., Vitorino et al., 2002), but the shelf waters surface layer are expected to be also influenced by: upwelling – favorable winds (Vitorino et al., 2002; Ribeiro et al., 2005); surface intensified poleward flows along the slope, associated with the Iberian Poleward Current (IPC) (e.g., Peliz et al., 2003; Garcia-Soto et al., 2002) and buoyant plume – the Western Iberia Buoyant Plume (WIBP) (e.g., Peliz et al., 2002). Buoyancy induced coastal currents occur in areas of major river outflow. The northern Portuguese shelf is influenced by five major rivers (Minho, Lima, Cávado, Ave and Douro) discharging within 20 km of each other, and therefore inner shelf waters tend to have reduced salinity and high turbidity. The Douro River is the largest of these rivers with an annual mean discharge of 8.2×10^9 m^3 and its catchment covers 98×10^3 km^2. In contrast in the Spanish sector there are four rias (Vigo, Pontevedra, Arosa and Muros) which are drowned river systems deeply incised into the coastline. In terms of suspended particles composition the terrigenous components generally prevail inshore and increase toward the bottom nepheloid layer (BNL). In the upper part of the water column particles are more organic (Oliveira et al., 2002). Most of the lithogenic particles suspended in both the BNL and surface nepheloid layer (SNL) derive directly from the weathering of the high mountains (1000 m) of the Minho region mainly dominated by granitic and schist-greywacke formations. During periods of heavy rain, rivers carry high loads of suspended material, with a composition dominated by clay minerals, quartz and feldspar (Oliveira et al., 2002; Santos et al., this issue). In this study we use the mineralogy of suspended fine sediments as tracers of river runoff and try to comprehend the sediments dispersal on the shelf, in winter conditions.

Methods

A CTD/nephelometer and water sampling survey was conducted, on the northern part of the western Iberian shelf (24 February–7 March 2006). A total of 259 water samples were collected and used to evaluate the particulate matter concentration, calibrate the nephelometer response and characterize suspended sediment grain-size and mineralogy. Water samples were collected with a Rosette system in high optical turbidity layers (BNL and intermediate nepheloid layers -INL), as well as at surface (0–1 m) and 5 m water depth. The samples were filtered on board through (0.45 µm, 47 mm diameter) cellulose acetate filters. The current was monitored over the inner shelf, north of the Douro river mouth, by means of a 600 kHz ADCP moored over the 32 m isobath.

Mineralogical analysis was performed directly on the filters. XRD measurements were performed on a PANalytical diffractometer, using CuKα radiation. Scans were run between 2º and 35° 2θ. Peak areas of the basal reflections of the main minerals were determined using the X'Pert HighScore program (Version 1.0f) and weighted by empirically estimated factors. For semi-quantitative determination, criteria recommended by Schultz (1964), Thorez (1976) and adapted by Rocha (1993) have been followed. The dispersed grain-size distribution was determined using a laser forward-scattering particle size (Malvern MicroP2000).

Results and discussion

River runoff was rather low during the beginning of the winter 2006 (mean <350 m^3s^{-1} for the Douro River and <250 m^3s^{-1} for the Minho River). The survey of February–March 2006 was conducted just after a period of northerly winds, when the Douro River runoff increased to an average of nearly 780 $m^3 s^{-1}$. However the WIBP was not detected during this period. The initial southward current with maximum surface speed around 40 cm s^{-1}, changed to northward direction on 3 March, as a consequence of a change in wind forcing, reaching nearly 1 m s^{-1} on 4 March. While that occurred within one inertial period, a sudden change in wind to northerly on 4 March caused the current to change to southward, with a nearly simultaneous response for the whole water column, reaching values around 50 cm s^{-1} on 5 March. (Silva, A. et al., 2008). During the cruise, extremely variable winds direction induces inverse circulation over the continental shelf. Northerly winds induce southward currents, south of Minho River, but were insufficiently strong and persistent to promote upwelling and offshore extension of river plumes. By contrary, the density field shows the penetration of oceanic water over the shelf. The meandering of the IPC over the outer and middle shelf went to the 40–60 m isobaths, in the area between the Douro and Cávado rivers (NICC, 2007). The water column was vertically homogeneous with the exception of the coastal area, where freshwater inputs from rivers caused local stratification (<20 m) and higher turbidity (NICC, 2007). The particulate matter concentration (PMC) data showed that the study area was generally characterized by low values (mean 1.5 mg l^{-1}) (Figure 1A). At the surface (0–1 m), the PMC varied between 0.2 and 10.4 mg l^{-1} (mean 1.5 mg l^{-1}), with the highest value near the Cávado River mouth. At 5 m depth the general distribution pattern prevails with PMC between 0.4 and 5.6 mg l^{-1} (mean 1.5 mg l^{-1}). Near the bottom, the PMC values were slightly higher (mean 1.9 mg l^{-1}), with the highest values at the inner shelf, south of Douro river. Relatively high PMC were observed both at shallow depths near the river mouths, and near the seabed.

In order to characterize the output of rivers, only the data from the surface (0-1m) layer was used, where the influence of fresh water from the rivers is clear in the density field (Figure 1B, γ<26.75 kg m^{-3}). Areas where the PMC is higher than 2 mg l^{-1} normally showed lower salinity and temperature (river plumes). As previously demonstrated by numerical models (Otero et al., 2008), propagation of river plumes depended on wind events and phase of the tide, with a response at short time scales (1–3 h). These events are important to explain the behavior of textural and mineralogical composition of shelf suspended sediment.

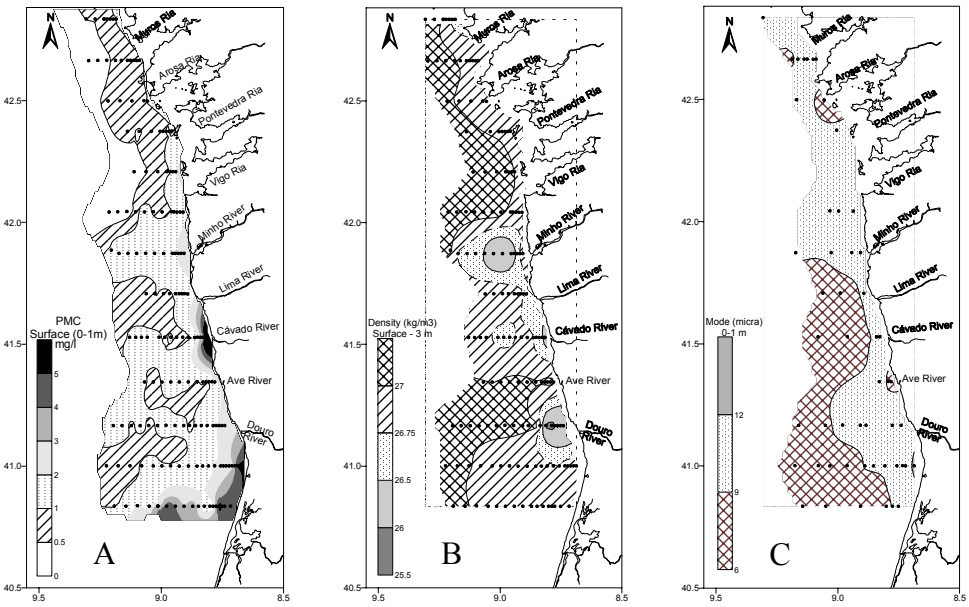

Figure 1. PMC (A), density and modal grain-size (C) distribution at surface (1–3 m) (B), for the February–March 2006 cruise.

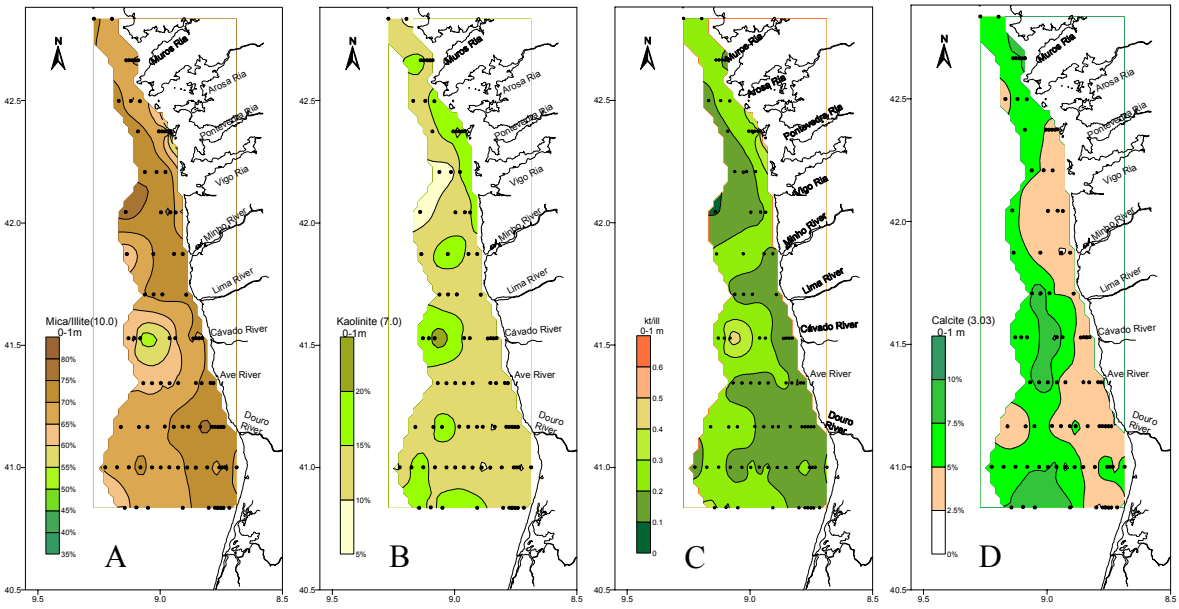

Figure 2. PM mineralogy distribution maps, at surface waters (0–1 m). (A) mica/illite, (B) kaolinite, (C) kaolinite (Kt)/illite (Ill) ratio, and (D) calcite.

The particulate matter (PM) samples collected in surface consist mainly of very fine silt and clay sized particles. The grain-size distribution curves are in general uni-modal, with a mode range between 6.6 μm to 13 μm. The distribution map (Figure 1C), allows the discrimination of two individualized water masses: more oceanic (<7.8 μm) related with the meandering IPC and coastal waters (>9 μm).

X-ray diffraction analysis, in surface water samples showed that the rivers plumes terrigenous components were mainly formed by clay minerals – illite, kaolinite and chlorite (Figure 2). The dominant mineral is illite with an average content of 69% (min: 36%, max: 79%), followed by kaolinite (average: 13%, min: 6%, max: 25%) chlorite (average: 8%, min: 3%, max: 18%) and calcite (average: 5%, min: 2%, max: 11%). Quartz and feldspars are also present in smaller proportions (average of 2% and 1% respectively). This mineralogy reflects the moderate climatic conditions prevailing in the source areas and the abundance of igneous (granitic rocks) and metamorphic rocks of Paleozoic age (schists, gneisses, micaschists and greywackes) in the region. Shelf waters PM composition is mainly due to the input of rivers, mainly the Douro River, that transports to the adjacent continental shelf suspended sediment, with high content of mica/illite (mean values higher than 70%), kaolinite (mean 12%) and chlorite (less than 5%) (see Santos et al., this issue). The Minho River also transport high content of mica/illite (mean 65%) with a slight increment of kaolinite (15%) and chlorite (6%). Selected minerals distribution maps are shown in Figure 2. The mineralogy distribution maps show us an integrated picture of the prevailing oceanographic processes. In the shelf, mica/illite is the predominant mineral, with the higher values (>70%) bordering the Portuguese coast (Figure 2A) and offshore the ria systems. It seems to be connected directly with Portuguese river runoff. The distribution map of kaolinite (Figure 2B) seems to indicate some contribution of kaolinite from Pontevedra Ria. It is also evident a maximum value in the shelf offshore Cávado River.

Kt/Ill ratio (Figure 2C) show a continuity of lower values near coast (<0.2), correlated with Portuguese rivers, that is interrupted near Minho River. Lower values are also found north of Minho River but now at middle shelf. Could this distribution pattern be an indication of northward Portuguese river transport (strong northward current event of 3 March) or/and an influence of ria discharge? Water and PM from the Pontevedra Ria are affecting the inner shelf and seems to be transported further south.

PM with higher content of calcite, can be a good indicator of marine waters, richer in biogenic components, were calcite are the main constituent of the skeletal remains. The calcite distribution map (Figure 2D) seems to reflect the influence of IPC in shelf waters. The two coastal lobules with lower calcite values (<5%) can be related with the two moderated north wind forcing events, insufficient to transport the water and sediment from rivers, further offshore.

Conclusions

The material being discharged from the Portuguese rivers is very similar in its general composition to the shelf suspended sediments. It is possible to correlate the mineral distribution with the major oceanographic winter processes, following the general current regime. There is clear evidence that the fine sediments exported by Portuguese rivers (mainly Douro and Minho) influence all the area and can be followed up to the middle shelf to the north (Galician shelf) and further south (south of the Douro River). The influence of Pontevedra Ria is also evident in coastal waters mineralogy.

Acknowledgements

This study has been supported by the NICC (POCTI/CTA/49563/2002) and ECOIS (POCTI/CTA/48461/2002) FCT projects. The authors would like to thank the crews and scientific team on board of N.O. Andrómeda, during which CTD data and suspended sediments were collected.

References

Garcia-Soto, C., Pingree, R.D., Valdés, L. (2002), Navidad development in the southern Bay of Biscay: climate change and swoddy structure from remote sensing and in situ measurements, *Journal of Geophysical Research,* 107 (C8), 3118, doi:10.1029/2001JC001012.

NICC project (2007), 2º year *FCT annual report* (POCTI/CTA/49563/2002). Unpublished.

Oliveira, A., Vitorino, J., Rodrigues, A., Jouanneau, J.M., Dias, J.A., Weber, O. (2002), Nepheloid layer dynamics in the northern Portuguese shelf, *Progress in Oceanography,* 52, 195–213.

Otero, P., Ruiz-Villarreal, M., Peliz, A. (2008), Variability of river plumes off Northwest Iberia in response to wind events, *Journal of Marine Systems*. (In press.)

Peliz, A., Rosa, T., Santos, A.M.P., Pissarra, J. (2002), Fronts, jets, and counter flows in the Western Iberian upwelling system, *Journal of Marine Systems,* 35(1–2), 61–77.

Peliz, A., Dubert, J., Haidvogel, D.B., Le Cann, B. (2003), Generation and unstable evolution of a density-driven Eastern Poleward Current: the Iberian Poleward Current, *Journal of Geophysical Research*, 108 (C8), 3268, doi:10.1029/2002JC001443.

Ribeiro, A.C., Peliz, Á., Santos, A.M.P. (2005), A study of the response of the chlorophyll-a biomass to a winter upwelling event off Western Iberia using SeaWiFS and in situ data, *Journal of Marine Systems*, 53, 87–107.

Rocha, F. (1993), *Argilas Aplicadas a Estudos Litoestratigráficos e Paleoambientais na Bacia Sedimentar de Aveiro*. PhD Thesis, Aveiro University, 399pp. Unpublished.

Santos, A.I., Balsinha, J. Oliveira, A. (2008), Suspended particulate matter tidal and seasonal variation in two mesotidal estuaries – Douro and Minho (NW Portugal). This issue.

Silva, A.J., Martins, I.**,** Bastos, L. (2008), An intermittent coastal current generated by buoyancy and wind forcing, *Geophysical Research Abstracts*, Vol. 10 (CD-ROM), EGU2008.

Thorez, J. (1976), *Practical identification of clay minerals*. Ed. G. Lelotte, Belgique, 99pp.

Wooster, W.S., Bakun, A., McLain, D.R. (1976), The seasonal upwelling cycle along the eastern boundary of the North Atlantic, *Journal of Marine Research*, 34 (2), 131–141.

Preferential transport paths of sediment fractions in a small estuary during river flood conditions

MARK PRITCHARD, MALCOLM O. GREEN

National Institute of Water and Atmospheric Research, P.O. Box 11-115,
Hamilton 3521, New Zealand
email: m.pritchard@niwa.co.nz, m.green@niwa.co.nz

Keywords: flood inundation, sediment transport, flocculation

ABSTRACT

Longer term changes in New Zealand estuarine substrate from sandy to muddy are thought to be mainly driven by the episodic delivery of high sediment loads from rivers in flood. The rapid delivery of nutrient-rich fine sediment to estuary basins has also been implicated in smothering shellfish and sea grass beds. Furthermore, fine sediment deposition drives the rapid spread of mangroves which consume otherwise economically and aesthetically valuable estuarine habitats. In this study we build on a previous investigation conducted in a small estuary that receives high sediment loads during river flood events. A series of field measurements and a finite mesh three-dimensional model have been used to investigate the paths and fate of three different sediment size fractions of cohesive sediments. The model was setup to receive a large sediment load comprising of three sediment size fractions delivered by flood waters from a single source. Model hydrodynamics were driven by salinity and tides and a high level turbulence module was included for closure. The sediment transport model was run with and without simple parameterizations of particle flocculation based on a SSC modified settling velocity. All particles were subject to a critical deposition and erosion threshold criterion. A subsequent series of simulations and a basin partition analysis showed after the initial influx of freshwater, sediments depending on initial threshold criterion and bed shear stresses followed specific transport paths. We discuss the implications of this with respect to the need of high quality observations to support future modeling studies.

Introduction

Many of the New Zealand North Island estuaries share very similar morphological features. Estuary basins are characteristically carved with a complex of deep and narrow sub-tidal channels. These channels are bordered by large expanses of inter-tidal mudflat fringed at the neap high water mark by mangroves. A mesotidal range and a large tidal excursion in the channels force the upper reaches of the estuaries to 'reset' every ebb tide with fresh headwaters from riverine input. This effectively flushes all saline waters from the upper estuary until the next flood tide forces a saline incursion beneath a buoyant outflowing surface layer. This discontinuity between the two water masses is often observed as a tidal intrusion front.

Most sediments are delivered to these estuaries during large flood events following heavy rainfall. Rapid drainage from steep catchments can cause river discharge to increase by orders of magnitude in little over half a day. The associated suspended sediment load also increases suddenly with high concentrations of particles of all size fractions being discharged as a 'slug' from river headwaters into the estuary. It is still not clear from observational studies what the ultimate fate of these sediments is in the days following a river flood event.

For this study, we present a number of initial observations and a series of model predictions for the Raglan Harbour, a small New Zealand North Island estuary. The results from a three-dimensional finite volume hydrodynamic and sediment transport model with simplified flocculation parameters are used to investigate the potential transport paths of cohesive particles within a small arm of the estuary basin.

Study site

Raglan Harbour discharges to the west coast of the North Island of New Zealand. It covers an area of ~33 km^2, with ~24 km^2 being intertidal. The estuary was formed post-glacially through the drowning of the

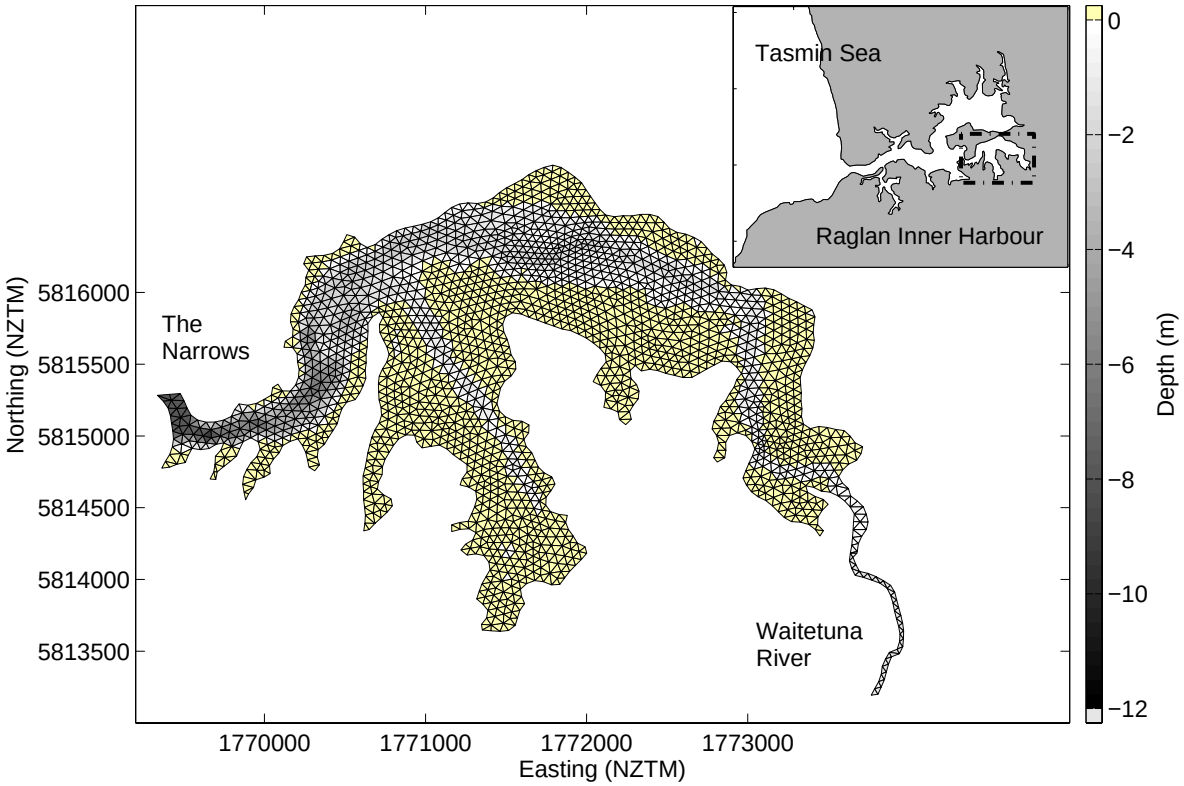

Figure 1. Finite element mesh of the Waitituna arm of the Raglan Harbour. Co-ordinates are New Zealand Transverse Mercator.

lower extremities of a branching river system (Sherwood and Nelson, 1979). The Waitetuna arm of the harbor, the main focus of this study, covers an area of ~5 km^2 to the east of a natural constriction known as the Narrows (Figure 1).

The Waitetuna arm has an extensive network of flood/ebb tidal channels, bordered by peripheral intertidal mudflats. The spring tidal range is ~4 m, and the neap range is 1.4 m, forcing peak streamwise tidal velocities of up to 2 ms^{-1} during flood and ebb tides through the Narrows. The Waitetuna arm's major source of freshwater is the Waitetuna River which receives the drainage from a 123 km^2 catchment area (see Figure 1). The river responds rapidly to rainfall and discharge can exceed 80 m^3s^{-1} during the floods which tend to occur during winter and spring. Base flow conditions are just ~4 m^3s^{-1}.

Model domain and setup

Hydrodynamics and sediment transport in the Waitetuna arm was modeled using modules from the DHI MIKE3 package. The FM (flexible mesh) hydrodynamic model is a finite-element, three-dimensional sigma-coordinate (multi-layer) semi-implicit model that finds numerical solutions for the Navier-Stokes equations for momentum. Mass is conserved through applying the principle of continuity. Estuarine physics are simulated through specifying, for example, tidal elevations, freshwater sources, eddy scales, turbulent closure schemes, surface and bottom boundary conditions, salinity/temperature structure and the earth's rotational effects. The finite element grid and baroclinic capability, plus the inclusion of a wetting and drying scheme, makes the FM model ideal for simulating tidally-driven flows and density fields in complex estuaries.

The DHI MT (mud transport) model simulates sediment transport through the application of the advection-diffusion (transport) equation. The effects of localized surface wave fields on sediment erosion, deposition, resuspension and transport may be computed. Particles may be introduced into the model domain as a sediment flux associated with a specific freshwater discharge. A simple parameterization of cohesive particles can be included in the model scheme.

Figure 1 shows the model's flexible mesh developed for the Waitetuna arm of the Raglan Harbour. Average cell size was approximately 1400 m^2 with five sigma levels. The model was forced at the Narrows by tide

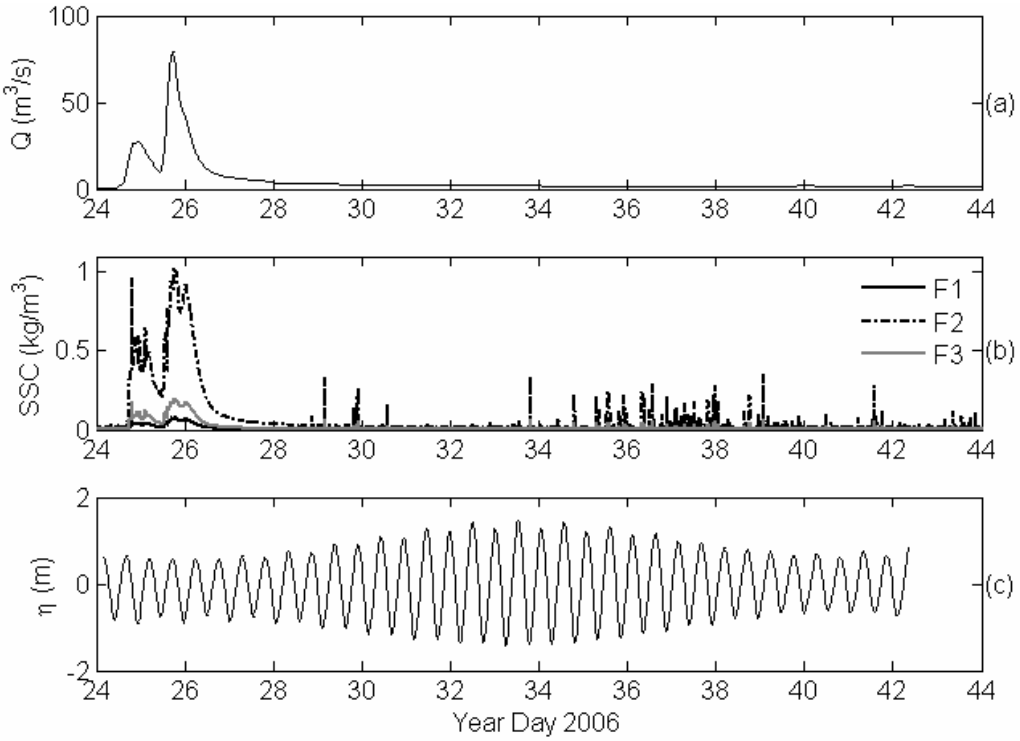

Figure 2. Model boundary conditions used in simulations for the January 2006 flood event. (a) Waitetuna River discharge, (b) suspended sediment concentration (F1 < 4 µm < F2 < 63 µm, F3 > 63µm) derived from OBS sensors and bottle sampling, (c) tidal elevations at the Narrows used to force hydrodynamics.

and constant salinity. Upstream boundary at Waitetuna was forced by freshwater and three sediment size fractions representing different size fractions of mud (F1 < 4 µm < F2 < 63µm, F3 > 63 µm).

The sediment transport module run with several different scenarios which included the effects of flocculation and alteration of deposition and erosion thresholds in the model scheme. Sediment inputs into the model at the Waitetuna boundary were based SSC flux and distribution of SSC across size fraction in the river headwaters. These were measured by optical backscatter sensors (OBS) and bottle samples during a flood experiment in January 2006.

Hydrodynamics in the model were forced with tides at the Narrows using elevations and currents computed from an ADCP moored in the channel (Pritchard and Green, 2008).

Preliminary results

Figure 3a shows that river discharge rises sharply in response to heavy rainfall over the catchment. The two peaks in the discharge correspond to two storm events. Sediment concentrations (Figure 2b) rise in response to the increasing discharge from the river. Sediment size fractions during the storms were measured as approximately: F1 – 6%; F2 – 79% and F3 – 15% (McKergow, personal communication).

Model simulations were used to determine sediment dispersal around the estuary during and after the flood. For this purpose two regions were defined: Sub tidal channels were classified as the area with depth < lowest astronomical tide (LAT) and inter-tidal mud flat with height > LAT. This effectively separated channelized areas from mud flats. The sediment mass in both regions were integrated with respect to depth and area and as cumulated over time for a 20-day period following the flood event.

Figure 3 shows results for a series of simulations using a variety of deposition and erosion thresholds for the sediment fractions in the sediment transport model (Whitehouse et al., 2000). The figure serves to illustrate the sensitivity of the system and importantly, how subtle changes in threshold can alter sediment transport paths. The inclusion of flocculation (modification of settling velocity through SSC) tended to cause F1 size sediments to initially settle and deposit in both channel and mudflat regions. However, on subsequent progression into spring tides, F1 is resuspended on the flat and moved back into the channel. F2 and F3 size

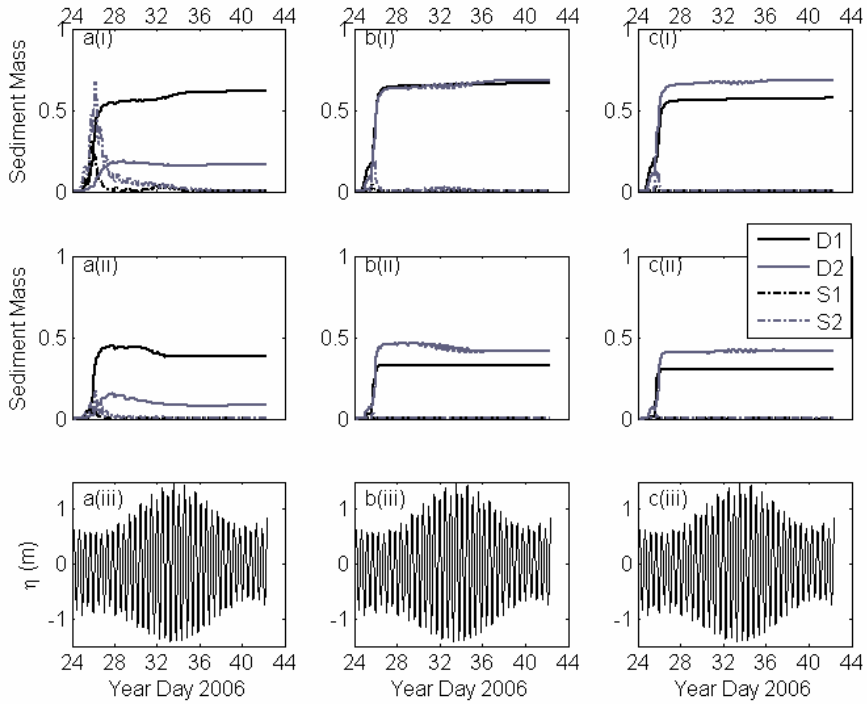

Figure 3. Sub-tidal channel (i) and inter-tidal mudflat (ii) suspended sediment and deposited mass and tidal elevation (iii) for: (a) F1; (b) F2; (c) F3 for two different model threshold parameterizations for the sediments. Sediment mass has been normalized by total input for the study period. D = Deposited Mass; S = Suspended Mass.

particles settle in channels and on mudflat and in the aftermath of the flood show no signs of remobilization through the remainder of the simulation.

Running the model with no flocculation and altering threshold values further shows the importance of threshold parameterizations for the sediments. For example, lowering critical bed shear stress for erosion causes the coarser F2 and F3 sediments initially deposited in the channels, to remobilize during spring tides.

Conclusions

The DHI MIKE3 model suite has been used to investigate the dispersal of three sediment grain sizes in an estuary during and after a river flood. Results suggest transport pathways are highly sensitive to threshold parameterizations within the sediment transport model. A sensitivity analysis emphasizes the importance of obtaining good field observations and calibration parameters for estuarine sediment transport models.

Acknowledgements

The DHI MIKE3 package was supplied and supported by DHI for this project. Thanks to Lucy McKergow for the sediment size analysis. The research was supported by The Foundation for Research, Science and Technology (Effects-Based Protection and Management of Aquatic Ecosystems; C01X0307) and Environment Waikato.

References

Pritchard, M., Green, M.O. (2008), *Flushing of fine sediments from an upper arm of Raglan/Whaingaroa Harbour*, Proceeding of DHI 5th Asia Pacific Software Conference, Auckland 2008.

Sherwood A.M., Nelson C.S. (1979). Surficial sediments of Raglan Harbour, *New Zealand Journal of Marine and Freshwater Research*, 13(4), 475–496.

Whitehouse, R., Soulsby, R., Roberts, W., Mitchener, H. (2000), *Dynamics of estuarine muds*. Thomas Telford Publishing, UK. ISBN 0-7277 -2864-4.

Sediment removal and entrainment in the Columbia River plume

ALEXANDER R. HORNER-DEVINE[1], EMILY Y. SPAHN[1], JONATHAN D. NASH[2], DAVID A. JAY[3], LEVI KILCHER[2]

1. Department of Civil and Environmental Engineering, University of Washington, P.O. Box 352700, Seattle WA 98195-2700, USA
email: arhd@u.washington.edu, spahn@u.washington.edu

2. College of Oceanic and Atmospheric Sciences, Oregon State University, 104 COAS Administration Building, Corvallis OR 97331-5503, USA
email: nash@coas.oregonstate.edu, lkilcher@coas.oregonstate.edu

3. Department of Civil and Environmental Engineering, Portland State University, P.O. Box 751, Portland OR 97123-0751, USA
email: djay@cecs.pdx.edu

Keywords: river plume, turbulence, sediment transport, re-suspension

ABSTRACT

Sediment transport in the Columbia River plume was investigated during the multi-year RISE (River Influences on Shelf Ecosystems) project. Fine sediments carried in the Columbia River plume deliver nutrients, micronutrients and micro-organisms to the coastal waters of the US Pacific Northwest, and help to support a productive coastal ecosystem. Sediment discharge is generally greater during winter and spring months due to storm and snowmelt induced flow peaks. In the summer, river discharge is one quarter to one half of the peak discharge and the river carries significantly less sediment. Intensive surveys of the near-field hydrodynamics, turbulence and suspended sediment fields during summer 2005 and spring 2006 are used to contrast the sediment transport during high-flow and low-flow regimes. In the summer, low river flow results in low density stratification and top-to-bottom turbulence during peak ebb. River input of sediment is low and we observe significant re-suspension of sediment in the near-field region. In the spring, the water column is strongly stratified, there is little re-suspension and all of the sediment input to the plume is from the river. Thus, sediment is supplied to the plume directly from the river in the spring, and from the shelf bottom near the mouth in the summer. This distinction may have important implications for geochemical contributions to the plume, since nutrients delivered to the shelf in the winter and spring may be re-processed in the benthos before they are re-suspended in the summer.

Introduction

Sediment and other river-borne particles deliver vast amounts of terrigenous organic matter, nutrients and contaminants to the coastal ocean, where they play key roles in the coastal ecosystem. The balance of incorporation of particles into the coastal ecosystem vs. burial in the deep ocean depends on a complex set of fluid dynamical processes at the mouth of the river, along the shelf and in the plume (Geyer et al., 2004). The fate of particles depends to a large extent on the rate at which they are removed from the water column and if, or when, they are re-suspended from the bottom. In this work we investigate re-suspension processes using extensive data sets collected during two River Influences on Shelf Ecosystems (RISE) cruises near the mouth of the Columbia River in August 2005 and May 2006. The two cruises correspond to late summer and spring freshet conditions, respectively, which are observed to have very different sediment transport regimes.

Site and sampling conditions

The Columbia River flows into the Pacific Ocean at Astoria, Oregon on the border between Oregon and Washington states (Figure 1a). It is the fourth largest river in the United States with an annual mean discharge of approximately 7300 $m^3 s^{-1}$ (Hickey, 1998; Barnes, 1972). The tidal range in the vicinity of the mouth is large (approximately 4.0 m) and the main estuary channel is relatively narrow (1–2 km), resulting in

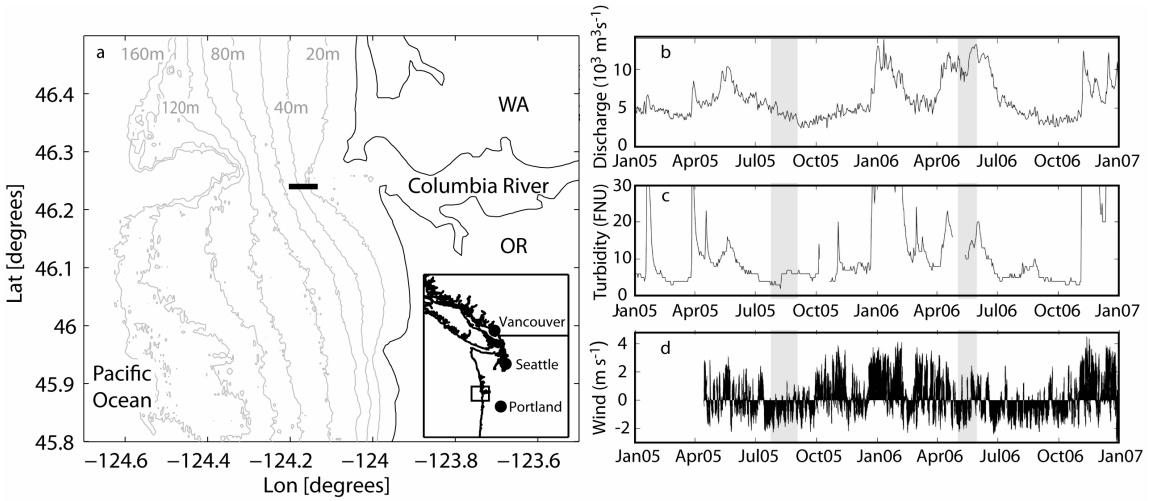

Figure 1. Sampling location and conditions for Columbia River plume observations. (a) Location of E-W transect (thick black line) relative to the mouth of the estuary. River discharge (b) and turbidity (c) measured 86 km upstream from the mouth at the Beaver Army Terminal and alongshore wind speed measured at the Columbia River bar buoy (d). Shading indicates cruise periods in August 2005 and May 2006.

a salinity intrusion that propagates are far as 30 km upstream from the mouth. The river mouth is approximately 5 km wide and oriented towards the south west. As a result of complex bathymetry in the estuary channel near the mouth, the estuarine outflow discharges approximately due west during maximum ebb. The tidal plume that is discharged on the ebb is very energetic (Horner-Devine et al., 2008), bounded by strong fronts that penetrate well below the plume (Orton and Jay, 2005) and often generates intense internal waves (Nash and Moum, 2005).

In this analysis, we focus on data that was collected along an across-shelf sampling line located between 124.13–124.21°W at the latitude of the Columbia River mouth, 46.24°N (Figure 1a). The line begins approximately 4.5 km from the river mouth and extends 4.5 km west along the main axis of the outflow from the estuary and it took between 45 and 120 minutes to cover the transect. The data set includes 33 transects during spring tide on 29 May 2006, and 123 on 20 August 2005. During neap tides, 83 transects were completed on 10 August and 12 in May. Operations along the line during neap tide in May were abandoned due to inclement weather. Thus, continuous sampling spanned at least one day for all four periods, except the neap period in May 2006. River discharge is 2–3 times higher in May 2006 than it was in August 2005, due primarily to the snowmelt-induced spring freshet in May (Figure 1b), and the turbidity in the river was approximately twice as high. Winds were upwelling favorable in August and mixed in May.

Methods

In order to investigate the processes leading to re-suspension we obtained coincident measurements of turbulent microscale shear and optical backscatter using Chameleon, the OSU Ocean Mixing Group's loosely-tethered microstructure profiler (Moum et al., 2005), in addition to standard hydrographic measurements. Profiles were obtained every 1–3 minutes, providing 50–500 m horizontal resolution depending on ship speed (2–10 knots over ground) and water depth. The profiler is equipped with a bottom-crasher, which allows sampling to within 10 cm of the seabed. Optical backscatter (OBS) measurements were calibrated for suspended sediment concentration (SSC) using bottle samples ($r^2 > 0.88$ for both cruises). The turbulent kinetic energy ε is computed from the measured shear variance and the turbulent diffusivity K_ρ is computed from ε assuming a TKE production-dissipation balance. The bottom stress τ_b is computed from profiles of ε in the bottom boundary region to determine u^* assuming a modified law-of-the-wall (Perlin et al., 2005). Particle fall velocity was estimated to be approximately 0.3 mm s^{-1} based on a modified settling tube method and LISST-FLOC particle size estimates. This is consistent with the smaller of two settling classes observed in the estuary (Fain et al., 2001) as well as the observed relationship between τ_b and SSC. It is possible, however that particles also settle as aggregates at a velocity greater than 1 mm s^{-1}.

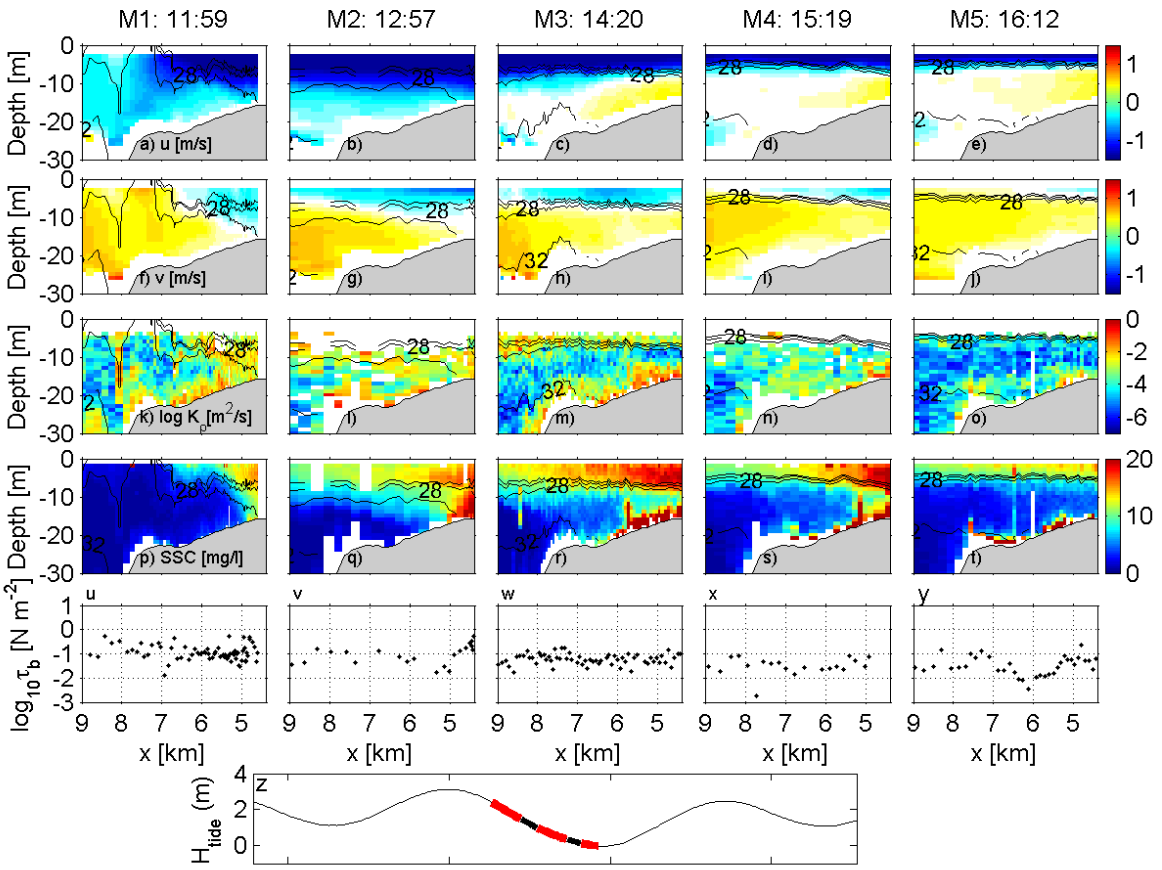

Figure 2. Hydrographic and sediment data from transect passes during greater ebb spring study on 29 May 2006. From top to bottom, the plots show E-W velocity (+ve east) with salinity contours, N-S velocity (+ve north), the eddy diffusivity, suspended sediment concentration and bottom stress. Each column corresponds to a different transect, which took approximately one hour. Tidal height is plotted in the lowermost panel and the times for each transect are indicated by the red and black sections.

Results

The sediment dynamics that are observed in the high flow period are shown in Figure 2. The plume is strongly stratified and, after the initial ebb pulse, thins rapidly and loses contact with the bottom in this region of the shelf. From this point on, the flow is directed landward along the bottom. More sediment is carried in the plume in May compared with August, and that sediment appears to come directly from the estuary. Mixing and gravitational flux act to detrain sediment from the plume as it evolves seaward. Re-suspension is limited to the bottom 5 m and there is no direct flux of benthic sediment into the plume.

The sediment dynamics that are observed in the low flow period are very different (Figure 3). During the spring tide in August 2005 large re-suspension events are observed, which mobilize bottom sediments and mix them upward into the water column. Observations of advective flux in the near-surface region and salinity-binned turbulent flux confirm that the re-suspended sediments are entrained into the fresher surface plume water, where they are transported rapidly away from the river mouth. The transect data also illuminate a number of details about the structure of the near-field plume that impact the fate of shelf sediments. At the beginning of the greater ebb the velocity and turbulent structure of the plume extend to the seafloor in the nearshore region. Mid-way through the ebb, the plume has re-stratified and detached from the bottom, except for a location approximately 6 km from the river mouth where it remains in contact with the bottom. During this period, re-suspended sediment is ejected from the near-bottom region and carried high into the water column. Some of this sediment is entrained into the surface flow and carried away in the plume, while some may also be re-deposited. The near-bottom flow is convergent, with continued seaward flow from the river as well as increased landward flow from offshore, which may trap near-bottom suspended sediments.

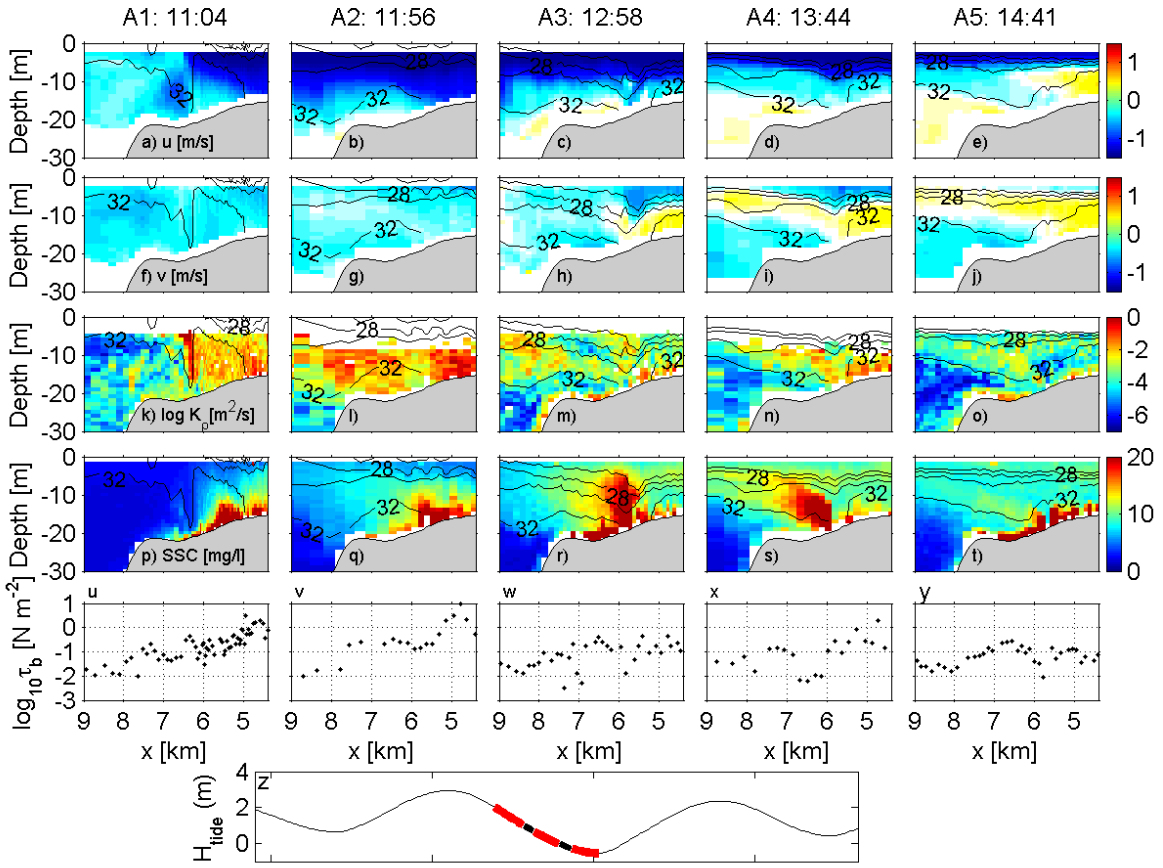

Figure 3. Hydrographic and sediment data from transect passes during greater ebb spring study on 20 August 2005. The panels are as in Figure 2.

Conclusions

These observations suggest that the source of sediment to the plume changes from an entirely riverine source in the winter and spring, to include a significant shelf source in the summer and fall. This seasonal cycle may have important consequences for the fate and transport of sediment bound nutrients in the plume ecosystem.

References

Barnes, C.A., Duxbury, A.C., Morse, B.-A. (1972), *Circulation and selected properties of the Columbia River effluent at sea*. In: The Columbia River Estuary and Adjacent Ocean Waters, Pruter, A.T., Alverson, D.L. (Eds.), University of Washington Press, Seattle, WA, USA. pp41–80.

Fain, A.M.V., Jay, D.A., Wilson, D.J., Baptista, A.M. (2001), Seasonal and Tidal Monthly Patterns of Particulate Matter Dynamics in the Columbia River Estuary, *Estuaries*, 24(5), 770–786.

Geyer W.R., Hill, P.S., Kineke, G.C. (2004), The transport, transformation and dispersal of sediment by buoyant coastal flows, *Contiental Shelf Research*, 24(7–8), 927–949.

Hickey, B.M., Peitrafesa, L.J., Jay, D.A., Boicourt, W.C. (1998), The Columbia River plume study: subtidal variability in the velocity and salinity field, *Journal of Geophysical Research*, 103(C5), 10339–10368.

Horner-Devine, A.R., Jay, D.A., Orton, P.M., Spahn, E.Y. (2008), A conceptual model of the strongly tidal Columbia River plume, *Journal of Marine Systems*. (In press.)

Moum, J., Gregg, M., Lien, R., Carr, M. (1995), Comparison of turbulence kinetic energy dissipation rate estimates from two ocean microstructure profilers, *Journal of Atmospheric and Oceanic Technology*, 12, 346–366.

Nash, J.D., Moum, J.N. (2005), River plumes as a source of large-amplitude internal waves in the coastal ocean, *Nature*, 437(7057), 400–403.

Orton, P.M., Jay, D.A. (2005), Observations at the tidal plume front of a high-volume river outflow, *Geophysical Research Letters*, 32(11), L11605.

Perlin, A., Moum, J.N., Klymak, J.M., Levine, M.D., Boyd, T., Kosro, P.M. (2005), A modified law-of-the-wall to describe velocity profiles in the bottom boundary layer, *Journal of Geophysical Research*, 110, C10S10, doi:10.1029/2004JC002310, 2005.

Sand transport induced by acceleration-skewed waves and currents – The TRANSKEW project

PAULO DA SILVA[1], TIAGO ABREU[2], PAULA FREIRE[3], GUSTAAF KIKKERT[4], HERVÉ MICHALLET[5], TOM O'DONOGHUE[4], SANDRA PLECHA[1], JAN S. RIBBERINK[6], GERBEN RUESSINK[7], FRANCISCO SANCHO[3], KATE STEENHAUER[4], ANDRÉ TEMPERVILLE[5], DOMINIC A. VAN DER A[4], JEBBE J. VAN DER WERF[6]

1. Departamento de Física, Universidade de Aveiro, Campus de Santiago, 3810-193 Aveiro, Portugal
email: psilva@ua.pt, sandraplecha@ua.pt

2. Instituto Politécnico de Viseu, DEC-ESTV, Campus de Repeses, 3504-510 Viseu, Portugal
email: abreu_tiago@portugalmail.pt

3. National Civil Engineering Laboratory, Av. do Brasil 101, 1700 Lisboa, Portugal
email: pfreire@lnec.pt, fsancho@lnec.pt

4. School of Engineering, University of Aberdeen, Aberdeen AB24 3UE UK
email: g.a.kikkert@abdn.ac.uk, t.odonoghue@abdn.ac.uk, k.steenhauer@abdn.ac.uk, d.a.vandera@abdn.ac.uk

5. University of Grenoble – LEGI, BP53, 38041 Grenoble Cedex 9, France
email: herve.michallet@hmg.inpg.fr, andre.temperville@wanadoo.fr

6. Water Engineering and Management, University of Twente, P.O. Box 217, 7500 AE Enschede, Netherlands
email: j.s.ribberink@utwente.nl, j.j.vanderwerf@utwente.nl

7. Department of Physical Geography, University of Utrecht, P.O. Box 80115, 3508 TC Utrecht, Netherlands
email: g.ruessink@geo.uu.nl

Keywords: sediment transport, skewed waves, fluid accelerations

ABSTRACT

New experiments of sand transport under sheet flow conditions were recently carried out in the Large Oscillating Water Tunnel (LOWT) of WL|Delft Hydraulics. These experiments were aimed to study the effects of flow accelerations on sand transport under asymmetric oscillatory flows that are characteristic of the surf zone. The project comprised measurements of integral parameters such as net transport rates and time-averaged suspended sand concentrations, as well as detailed time-dependent measurements of the near bed flow and concentrations for selected test conditions. This work describes the overall experimental project and present first results of the measurements.

Introduction

As waves travel and shoal towards the beach, they become peaked with sharp wave crests and long wave troughs. The corresponding orbital velocity near the bottom shows a similar (time) variation and this effect can be translated in terms of velocity skewness. Additionally the waves attain a sawtooth shape, with a steep front face and more gently sloping rear face. Under the steep front face, between the past wave trough and the following wave crest, the near bed velocity varies rapidly from a maximum negative (offshore) value to a maximum positive (onshore) value, giving rise to rapid fluid accelerations. The accelerations induced during

the rear face of the wave are much smaller. This effect is related with the so-called acceleration skewness. The effect of fluid accelerations seems to play a key role in sediment transport and sand bar migration (e.g., Hoefel and Elgar, 2003) and has been incorporated in different sediment transport models (e.g., Silva et al., 2006; Nielsen, 2006; Gonzalez and Madsen, 2007).

Only few researchers have investigated the effect of acceleration skewed flows on sand transport: King (1991) performed a series of experiments in the oscillatory flow tunnel of Scripps Institute of Oceanography under half-cycle sawtooth waves; Dibajnia and Watanabe (1998) and Watanabe and Sato (2004) have conducted experiments in the oscillatory flow tunnel of the University of Tokyo in sheet flow (flat-bed) conditions with irregular and regular oscillatory flows, respectively. These experiments were performed with flow periods shorter than 5 s. Longer periods could not be considered because of the limitations of the facility.

Due to this lack of experimental data, the TRANSKEW (sand TRANsport induced by SKEWed waves and currents) project was founded The aims of this project are: 1) to obtain a new reliable dataset of detailed flow and sand transport processes under sheet flow conditions generated by full-scale, regular, acceleration- and velocity-skewed oscillatory flows with and without opposing net currents; 2) to analyze the effects of the wave nonlinearities (such as the velocity and acceleration skewness) and the presence of a net current on the sediment transport processes and 3) to contribute to validation and further development of sand transport models.

The experiments

The experiments were performed in the Large Oscillating Water Tunnel (LOWT) at WL|Delft Hydraulics, the Netherlands, from 17 September to 3 December 2007. The experimental facility is of a U-tube construction with a rectangular horizontal test section (14 m long, 0.3 wide and 1.1 m height with a 0.3 m thick sand bed) and two cylindrical risers at either end. A piston system housed in one of the cylinders is capable of simulating near bottom velocities in the test section that correspond to full-scale wave conditions in the near shore-zone. The LOWT is fitted with a recirculation system that enables the generation of a mean current that is superimposed on the oscillatory flow.

The hydraulic conditions in the LOWT test section consisted of a repetition of regular oscillatory flows for the following three wave/current conditions: Series A consisted of regular oscillatory flows with different degrees of acceleration skewness, $\beta = a_{max}/(a_{max} - a_{min})$, where a is the acceleration; Series B considered acceleration-skewed oscillatory flows with a collinear net current (U_0), opposing the wave direction; and Series C considered both velocity and acceleration skewed oscillatory flows. The velocity skewness is characterized by $R = u_{max}/(u_{max} - u_{min})$, where u is the flow velocity. The test conditions are summarized in Table 1. The root-mean-square-value of the oscillatory velocity, U_{rms}, was maintained constant for all the conditions ($\approx$0.83 m s^{-1}).

As an example, Figure 1 presents the time series for the velocity and acceleration devised for condition A1 and C1. The test conditions were planned in order to satisfy the working limits of the LOWT, and to obtain sheet flow conditions for every test conditions. The values of β considered are close to those found in nature in the shoaling and surf zones. In all the tests the bed consisted of well-sorted quartz sand (ρ = 2650 kg m^{-3}) with a median grain diameter, d_{50} = 0.20 mm.

Table 1. Experimental conditions

Condition	U_0 (m s^{-1})	Wave period (s)	β	R
A1	0	7	0.65	0.5
A2	0	10	0.65	0.5
A3	0	7	0.75	0.5
A4	0	10	0.75	0.5
B1	−0.2	7	0.65	0.5
B2	−0.4	7	0.65	0.5
B3	−0.2	7	0.75	0.5
B4	−0.4	7	0.75	0.5
C1	0	7	0.65	0.6
C2	0	10	0.65	0.6
C3	0	7	0.5	0.6

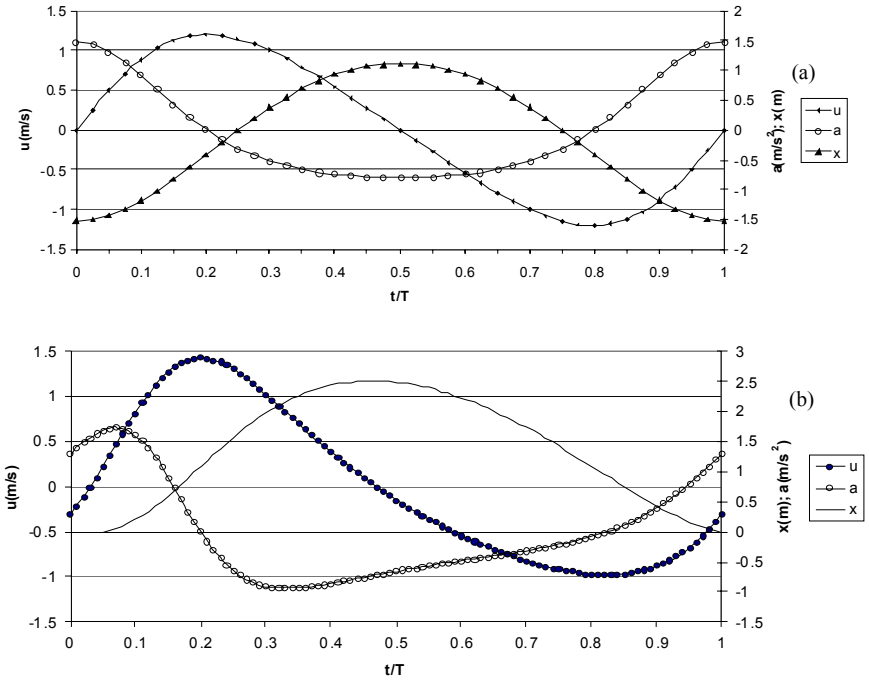

Figure 1. Velocity, displacement and acceleration time series for (a) A1 and (b) C1 conditions.

The measuring program was divided in two phases: the first part (M1) consisted of net sand transport rates measurements; the second part (M2) consisted of detailed measurements of time-dependent sand concentrations and flow velocities.

In the M1 experiments, a total of 48 runs corresponding to the hydraulic conditions listed in Table 1 were conducted. The bed profile before and after each run was measured with a Bed level Profiling System (BPS). For each run the free stream velocity was measured with an ElectroMagnetic Flow meter (EMF). The sand samples collected from the sediment traps located at both ends of the tunnel (and for Series B, also in the trap of recirculation system) were weighted underwater and analyzed in a Visual Accumulation Tube (VAT) to determine the particle size distribution.. Net transport rates were then computed from masses of sand and the volume change of sand along the tunnel test section, using a mass conservation method.

In the M2 tests, different measuring instruments were deployed in the test section of the LOWT: ABS – Acoustic Backscatter System, UVP – Ultrasonic Velocity Profiler, ADVP – Acoustic Doppler Velocity meter Profiler, Vectrino, CCM – Conductivity Concentration Meter and OPCON – Optical Concentration meter, allowing the measurement of time-dependent flow and sand concentrations in the suspension and sheet-flow layers. Time-averaged suspended sediments concentration measurements were also performed with a TSS – Transverse Suction System. The M2 measurements were made for five selected conditions (A1, A3, B2, B4, C1) and around 80 experiments were carried out. These measurements allow for estimating important quantities in sediment transport dynamics, such as, bed shear-stresses, roughness heights, sediment fluxes and sheet-flow layer characteristics (e.g., thickness of the layer, erosion depth).

Results

This paper focuses on the first part of the experiments, i.e., the net transport rate measurements. Figure 2 presents the measured values of the net transport rates for all the runs. Figure 2 (a, b) illustrate the effect of varying the acceleration skewness on net transport rates for the Series A and Series C conditions, respectively. In both cases, the increase of β increases the net transport in the (positive) wave direction. Notice also that the net transport rates are lower for increasing wave periods. Figure 2c shows an increase of the sand transport in the wave direction with velocity skewness (R). For $R = 0.6$, the net transport rate measured for $T = 10$ s is higher than for $T = 7$ s. This is possibly due to the fact that the measured U_{rms} is 9% higher in C2 condition than in C1. In Figure 2d, the measured net transport rates are shown for different values of mean current velocity, for $T = 7$ s, and two different values of β (0.65 and 0.75). Results obtained show that the effect of the acceleration skewness, produces a net transport in the positive wave direction, therefore reducing the amount of sediment transported in the negative direction of the mean current.

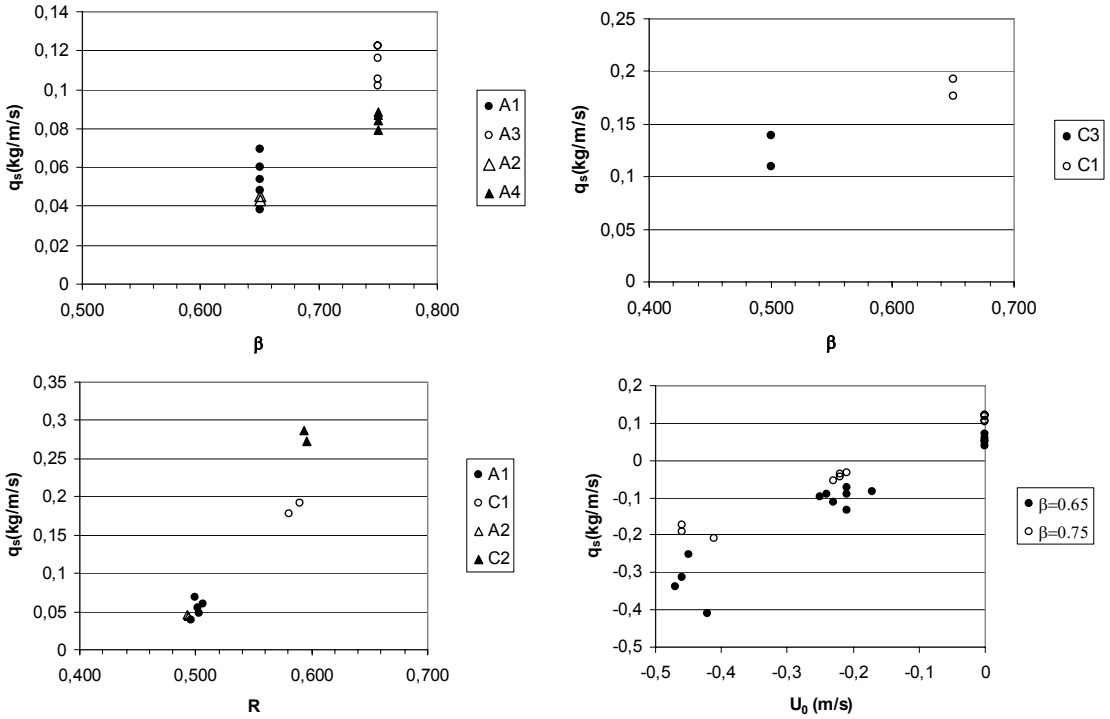

Figure 2. Comparison between measured net transport rates for conditions (a) A1–A4; (b) C1, C3; (c) A1, A2, C1, C2; (d) A1, A3, B1–B4.

Discussion and conclusions

A new consistent dataset of detailed and controlled laboratory measurements of near-bed flow velocities, sand concentrations and net transport rates under acceleration-skewed waves in sheet flow conditions is obtained. These measurements will contribute to fill the existing lack of data under such hydrodynamic conditions, particularly for the longer wave periods (T >5 s).

Preliminary results show evidence of the influence of acceleration-skewed oscillatory flows on net sediment transport rates: acceleration skewed oscillatory flows produce a net sand transport in the direction of the largest acceleration and the net transport rates increase with increasing acceleration skewness. The added effect of velocity skewness increases the net transport rates. On the other hand, the addition of an opposing net current is able to reverse the direction of the net sediment transport measured for the wave-alone cases.

Acknowledgements

This work was supported by the European Community's Sixth Framework Programme through the grant to the budget of the Integrated Infrastructure Initiative HYDRALAB III, Contract no. 022441 (RII3).

References

Dibajnia, M., Watanabe, A. (1998), Transport rates under irregular sheet flow conditions, *Coastal Engineering,* 35, 167–183.

Gonzalez-Rodriguez, D., Madsen, O. (2007), Seabed shear stress and bedload transport due to asymmetric and skewed waves, *Coastal Engineering,* 54, 914–929.

Hoefel, F., Elgar, S. (2003), Wave-induced sediment transport and sandbar migration, *Science*, 299, 1885–1887.

King, D.B. (1990), *Studies in oscillatory flow bed load sediment transport*. Ph.D. Thesis, University of California, San Diego.

Nielsen, P. (2006), Sheet flow sediment transport under waves with acceleration skewness and boundary layer streaming, *Coastal Engineering*, 53(9), 749–758.

Silva, P., Temperville, A., Seabra Santos, J.F. (2006), Sand transport under combined current and wave conditions: A semi-unsteady, practical model, *Coastal Engineering*, 53, 897–913.

Watanabe, A., Sato, S. (2004), *A sheet flow transport formula for asymmetric forward-leaning waves and currents*, Proceedings of the 29th ICCE, Lisbon, Portugal, pp1703–1714.

Effect of bottom stress formulation and tidal forcing on modeled flow and sediment trapping in cross-sections of tide-dominated estuaries

GEORGE P. SCHRAMKOWSKI[1], KARIN M.H. HUIJTS[2],
HENK M. SCHUTTELAARS[3], HUIB E. DE SWART[2]

1. Flanders Hydraulics, Berchemlei 115, 2140 Antwerp, Belgium
email: george.schramkowski@mow.vlaanderen.be

2. Institute for Marine and Atmospheric Research Utrecht, University of Utrecht,
P.O. Box 80000, 3508 TA Utrecht, Netherlands
email: k.m.h.huijts@phys.uu.nl, h.e.deswart@phys.uu.nl

3. Delft Institute of Applied Mathematics, Delft University of Technology, Mekelweg 4,
2624 CD Delft, Netherlands
email: h.m.schuttelaars@tudelft.nl

Keywords: tidal flow, density-driven flow, sediment trapping, tidal rectification

ABSTRACT

Field data collected in cross-sections of tide-dominated estuaries reveal that flow and suspended sediment concentration show pronounced spatial and temporal behavior, which depend on factors like tidal discharge, density gradients and the geometry of the cross-section. Models are capable of reproducing and explaining many aspects of the observations, but also marked discrepancies occur between model results and data. The objective of the present study is to systematically investigate the sensitivity of model output to formulations of physical processes. This is done by comparing two types of models. The first is a numerical model (NM) that solves the full shallow water equations with prognostic salt dynamics. The second is an idealized model (IM) that solves a reduced set of equations for tidal water motion and uses a diagnostic salinity field. The IM can be used as a tool to interpret the complex output of the NM. The NM, on the other hand, can be used to probe the limits of applicability of the IM and may give hints on further improvements of the IM.

Models

The IM results in a 2DV description of the residual and tidal flow in a cross-section of a weakly non–linear, tidally dominated channel without vertical density stratification. The model uses a diagnostic density field and a rigid lid approximation. The cross-sectional bottom profile is Gaussian, with depth $H = H_{max}$ at the centerline of the channel and $H = 2$ m near the banks, the cross–sectionally averaged water depth is denoted by H. The barotropic forcing is prescribed by specifying a cross–sectionally averaged M_2 tidal velocity amplitude U. The baroclinic flow results from prescribed residual and M_2 components of the horizontal density gradient. The water surface is stress-free and the velocity vanishes at the bed (no slip). The coefficient of vertical viscosity (A_v) and mixing (K_v) are taken constant and are related to the tidal flow U and average bottom depth by the relation

$$A_v = K_v = 0.002 U \bar{H} \ . \qquad (1)$$

The NM solves the three–dimensional shallow water equations with a prognostic density field and a free lid. To be able to compare the numerical model results with those obtained with the IM, the setup of the NM is chosen such that it mimics the basic assumptions of the IM as close as possible. Therefore, the model geometry describes a tidal channel of length 1200 km and uniform width $B = 5$ km. At the seaward entrance of the channel, an M_2 water level forcing (circular frequency σ) is imposed. The landward entrance is an open boundary on which zero discharge is prescribed. At a distance of 400 km from the seaward entrance, the cross-section is identical to the Gaussian bed profile in the IM. Only results in this cross–section are compared to the idealized model results. For further details, see Schramkowski et al. (2007).

For the NM a density difference between the seaward and landward entrance is imposed such that the residual along–channel density gradient of the NM equals the gradient imposed in the IM which is $\sim 10^{-4}$kg m^{-4}. To get similar forcings in both models, the following procedure is performed: first, a value for

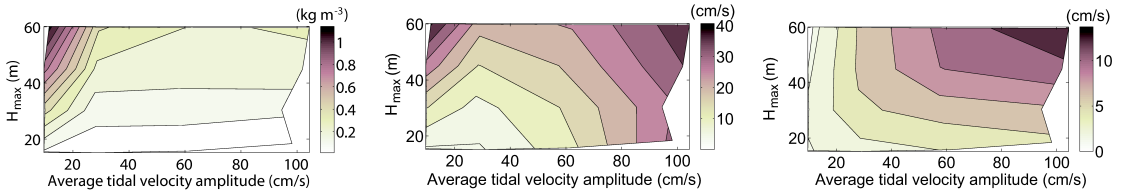

Figure 1. Several sensitivity diagrams: (a) maximum bed minus surface residual density difference, (b) maximum along-channel residual flow and (c) maximum across-channel tidal flow.

U is chosen. To get this value in the NM runs, the tidal boundary conditions are varied such that the required U is obtained at the cross–section. Finally, the residual and semi–diurnal parts of the depth–averaged density gradients, that are self-consistently calculated with the NM, are adopted as baroclinic forcing to the IM.

Finally, the hydrodynamics results from both NM and IM are used to solve the residual SSC from a sediment transport module (STM) a posteriori. This STM uses a morphodynamic equilibrium condition, which implies that the net lateral sediment flux (advective plus diffusive) vanishes. For a detailed discussion, see Huijts et al. (2006).

Methods

To assess the applicability of the IM, the IM results are compared with those obtained by the NM. To do this in an objective manner, we compare the residual and M_2 parts of velocity components (u, v, w) and sediment concentration c. Here u, v and w refer to along-channel, lateral and vertical velocity. Tidal components will be denoted by subscripts (e.g., u_{M0}). A good agreement is defined by a correlation coefficient larger than 0.75 and the ratio of the largest values between 0.3 and 3.

Results

For the IM and the NM, several experiments have been performed for a range of tidal flow velocities ($0.1 < U < 1$ m s^{-1}) and maximum bottom depth values (H_{max} = 10, 15, 30 and 60 m). The results are summarized in sensitivity diagrams, i.e., plots that show the variation of a quantity with U and H_{max}. Figure 1 shows three diagrams that give information about the applicability of the IM by probing the validity of its basic assumptions. First, Figure 1a gives maximum vertical difference in residual density. If this becomes too large the assumption of weak vertical stratification is violated. This occurs for situations with low tidal velocity U and large water depth. Figure 1b gives the along-channel residual velocity. If this becomes comparable to the along-channel directed tidal flow, the flow is no longer tidally dominated. Finally, the IM assumes that the flow is weakly non-linear, i.e., that advective terms in the momentum equations are small. This is not justified if the cross-channel tidal excursion length becomes comparable to the channel width B, i.e., if the lateral tidal velocity v_{M2} becomes too large. This occurs for high tidal velocity U and large depths (see Figure 1c). Nonetheless the actual applicability of the IM turns out to depend on the physical quantity and harmonic constituent under consideration. Explicitly, we found that:

- u_{M2} is well represented in all considered parameter ranges
- v_{M2} is not well computed for low tidal flow and large depths.
- u_{M0} is not correctly modeled for large tidal flow and large water depth
- v_{M0} is not calculated accurately for low tidal flow and fairly large water depth

Hence, *if the main interest is in the trapping of sediment*, the IM is applicable for all parameter values except for small tidal velocities and large water depth. This is because the lateral sediment transport is governed by the residual v_{M0} and tidal u_{M2} (see Huijts et al., 2006). This is confirmed by the sensitivity diagram in Figure 2a. The resulting SSC also shows good agreement between IM and NM in the same parameter regime, with the SSC mainly found at the left bank. Figure 2b shows this distribution for the case where U = 0.6 m s^{-1} and H_{max} = 30 m, which is within the region where IM and NM agree.

Finally, for the same parameter settings, Figure 3 shows the NM and IM results for the residual part of the along-channel velocity component. It is clear that the results are in good qualitative and quantitative agreement.

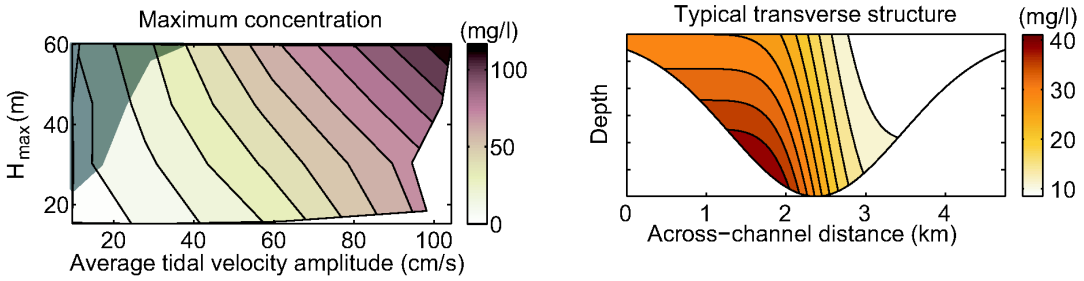

(a) Sensitivity diagram (b) Residual SSC

Figure 2. Left: sensitivity diagram for the residual SSC. The dark region indicates where the IM is not valid. Right: cross-sectional distribution of the residual SSC for $U = 0.6$ m s^{-1} and $H_{max} = 30$ m.

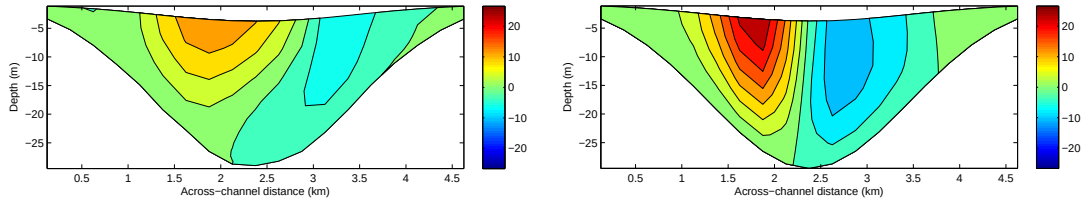

(a) Numerical model result (b) Idealised model result

Figure 3: Residual along-channel velocity for $U = 0.6$ m s^{-1} and $H_{max} = 30$ m. Left: numerical model, right: idealized model. The velocity scale is in cm s^{-1}.

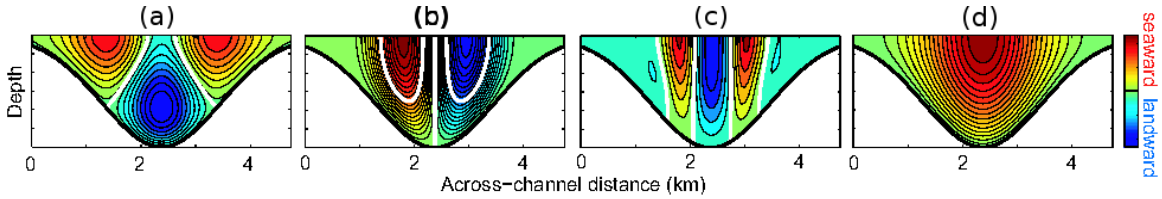

Figure 4. Four major mechanisms that contribute to the along-channel residual flow. Red (blue) is seaward (landward) directed flow.

Discussion

By combining the results of the IM and the NM, we have been able to use the NM to examine the validity of the IM (see Figure 1). Conversely, we can use the IM to interpret NM results for parameter settings where both models give similar results. As an example, we will elaborate on the result for the residual along-channel flow that is shown in Figure 3. Using the IM, is it possible to identify four major mechanisms that can contribute to the residual along-channel flow (see Figure 4). The first is the classical gravitational circulation (Figure 4a), which has relatively light (heavy) water moving seaward (landward) in the upper (lower) parts of the water column. This flow pattern is expected to be prominent at low tidal flow velocities. Figure 4b shows a horizontally stratified flow with inflow (outflow) located on the right (left) part of the cross-section. This contributing is due to tidal rectification by the Coriolis force. It arises from advection of the along-channel directed M_2 flow u_{M2} by the Coriolis induced cross-channel M_2 circulation (v_{M2}, w_{M2}) (Huijts et al., 2007). This cross-channel circulation consists of a single gyre (not shown). Figure 4c also stems from rectification, but here the main along-channel tide is advected with semi-diurnal cross-channel circulation that stems from the M2 component of the lateral density gradient. This lateral circulation consist of double gyre pattern (not shown) which reflects the fact the M_2 density variation has a larger amplitude in deeper parts. Finally, Figure 4d shows the residual flow that is related to the Stokes return flow. This flow is not included in the IM since it uses a rigid lid approximation. However, the NM does include free surface effects, so that it is possible to compute the discharge associated with the Stokes return flow. This discharge is then imposed in the IM.

It is clear from the results in Figure 4 that the Coriolis induced tidal rectification effect is the dominant mechanism in the situation shown in Fig. 3. Hence we see that the IM can be used as a means to identify key physical mechanisms in a NM result.

Conclusions and outlook

From the results presented above we conclude the following:

- the NM can be used to test validity of the IM, but the eventual reliability of the IM depends on the physical quantity and the tidal component of interest. In this respect, the IM may be more widely applicable than indicated by the sensitivity diagrams (Figure 1).
- the IM is able to describe lateral sediment trapping adequately, provided that the tidal flow is not too low or the water depth not too large (Figure 2).
- the IM can be used as a tool to interpret the outcome of the NM when both give similar results.

Recently, we have been extending the study by incorporating a partial slip formulation for the bed shear stress. This is motivated by the fact that it is inconsistent to use a no slip condition in conjunction with a constant vertical viscosity. As an alternative, one may put the near-bed boundary physically at the top of the constant stress layer rather than at the true bed. At this interface, it then realistic to adopt a partial slip condition.

It appears that the use of partial slip instead of no slip may have considerable consequences. As an example, let us consider the residual along-channel velocity u_{M0} once more. For partial slip, the relative importance of Coriolis driven tidal rectification (Figure 4b) will decrease. Indeed, the Coriolis driven lateral circulation is essentially driven by the vertical shear in the along-channel tidal flow. If one allows for velocity slip at the bed, the along-channel velocity will show less vertical variation, which indicates that the Coriolis driven lateral tidal flow will be smaller compared to the case where no slip is used. Hence we expect the Coriolis related tidal rectification to be a less important contributor to u_{M0}. The baroclinic contribution to u_{M0} (Figure 4c), however, will not decrease since the vertical variation of baroclinic forcing is less sensitive to velocity slip. Hence, we expect a relatively larger contribution from this mechanism if velocity slip is introduced.

By the same line of reasoning, we expect the IM to be more applicable if a partial slip formulation is used. Since velocity slip will lead to a decrease of the Coriolis induced lateral tidal circulation, it will give a lower value of $\nu_{M2}/(\sigma B)$. As a consequence, we expect the assumption of weak non-linearity that underlies the IM (see Figure 1c) to be valid over a larger range of the parameters U and H_{max}.

References

Huijts, K.M.H., Schuttelaars, H.M., de Swart, H.E., Valle-Levinson, A. (2006), Lateral trapping of sediment in tidal estuaries: an idealized model, *Journal of Geophysical Research*, 111, C12016, doi:10.1029/2006JC003615.

Huijts, K.M.H., Schuttelaars, H.M., de Swart, H.E., Friedrichs, C.T. (2007), Analytical study of the transverse distribution of along-channel and transverse residual flows in tidal estuaries, *Continental Shelf Research*, doi:10.1016/j.csr.2007.09.007. (In press.)

Schramkowski, G.P., Huijts, K.M.H., Schuttelaars, H.M., de Swart, H.E. (2007), *A model comparison of flow and lateral sediment trapping in estuaries*. In: River, Coastal and Estuarine Morphodynamics: RCEM 2007, Dohmen-Janssen, C.M., Hulscher, S.J.M.H. (Eds), 413–420.